



# Politecnico di Torino

Biomedical Engineering
A.y. 2024/2025
Graduation Session October 2025

Investigating the biophysical impact of Electromagnetic Fields on protein structures: a comparative analysis between Tubulin and G-actin

Supervisors:

Candidate:

Jacek Tuszynski Karthik Shankar Alessia Davoglio

#### Abstract

Abstract The cytoskeleton, composed primarily of microtubules and actin filaments, plays a crucial role in maintaining cellular architecture, regulating intracellular transports and supporting dynamic processes. Beyond their structural roles, cytoskeletal proteins also contribute to electrostatic regulation and can act as pathways for intracellular bioelectric signalling. Understanding how external physical stimuli modulate these proteins is therefore of biological and therapeutic interest. This thesis investigated the effects of electromagnetic field (EMF) stimulation on tubulin and G-actin using complementary biophysical approaches. Dynamic Light Scattering (DLS) was used to monitor hydrodynamic diameter and zeta potential, turbidity assays assessed polymerization dynamics, Raman spectroscopy analysed molecular vibrations and conductivity measurements proved electrostatic and charge transport properties. Two light-based devices with distinct physical characteristics were tested: Bioptron, emitting polarized broad-spectrum light, and Vielight, delivering near-infrared stimulation. DLS revealed device- and proteinspecific changes in hydrodynamic diameter under colloidally stable conditions. For tubulin dimers, the diameter was largely preserved under Vielight, while Bioptron induced modest decreases and a slight broadening of the distribution with a reduction in zeta potential, suggesting weak clustering. In G-actin, Bioptron increased the hydrodynamic diameter and broadened the size distribution, consistent with light-induced remodelling or oligomerization, while Vielight produced only minor and uniform shifts. These changes were accompanied by zeta potential variations: Bioptron reduced the negative charge of G-actin, favouring aggregation, while Vielight caused subtler modifications. Raman spectroscopy of both proteins did not show some characteristic peaks, such as the amide I band around 1650 cm<sup>-1</sup>, and stimulated and control samples were nearly identical, indicating that Bioptron irradiation did not measurably affect their vibrational profiles. Conductivity assays, performed under buffer conditions optimized for charge transport, provided complementary information. Tubulin showed low intrinsic conductivity and only modest changes upon irradiation. Under diluted buffer conditions, a further decrease in conductivity was observed, consistent with the reduced ionic strength and charge transport. G-actin exhibited high baseline conductivity, attributable to its acidic surface, but showed marked losses after Bioptron stimulation and moderate changes with Vielight. Turbidity assays, performed exclusively on tubulin, demonstrated a temporary acceleration of polymerization immediately after irradiation, followed by reduced reassembly after storage, particularly under Bioptron. Overall, these findings reveal that tubulin and G-actin display distinct sensitivities to EMF stimulation and can be selectively modulated according to wavelength, polarization, and

concentration. This modulation may be relevant in diseases involving cytoskeletal dysfunction, including Alzheimer's disease, depression, and actin-related disorders. In conclusion, this study shows that external light stimulation can influence the structural stability and electrostatic properties of cytoskeletal proteins. While these results open perspectives for photobiomodulation as a therapeutic strategy, further in vitro and in vivo studies are needed to validate these findings and determine their clinical applicability.

# Acknowledgements

I would like to sincerely thank Professor Jacek Tuszynski for offering me the opportunity to undertake one of the most enriching experiences of my life. The period spent at the University of Alberta has been deeply formative, it contributed significantly to my personal development and, above all, to my professional growth, enhancing both my research abilities and scientific perspective.

I would also like to thank Professor Karthik Shankar and Dr. Katia Simmen, who made this thesis possible by welcoming me into their laboratories and providing the opportunity to carry out this research project.

A special thank you goes to my tutor, Barbara Truglia, whose constant support and guidance made it possible for me to complete this journey. You truly taught me what it means to do research.

I am also truly grateful to the University of Alberta for welcoming me and providing an inspiring and supportive environment throughout my research stay.

I am deeply grateful to my parents, whose unconditional support, encouragement and trust have guided me through every challenge and made this journey possible. A special thanks also goes to my friends, who have always stood by my side with understanding and positivity, without their support, I would not have made it this far.

# Table of Contents

1	Intr	oduct	ion	1
2	Stat	te of t	he art	3
	2.1	Electr	omagnetic Fields	3
		2.1.1	The basics on Electric and Magnetic fields	3
		2.1.2	Generation of EMFs	5
		2.1.3	The electromagnetic spectrum	7
		2.1.4	Interaction of Electromagnetic Fields with Matter	8
		2.1.5	Application of EMFs in medicine and health and safety con-	
			siderations	9
	2.2 Photobiomodulation		biomodulation	10
		2.2.1	Definition of Photobiomodulation	10
		2.2.2	Biological mechanisms of PBM	11
		2.2.3	Application of PBM	11
		2.2.4	Vielight device	12
	2.3	Hyper	polarized Light	15
		2.3.1	Definition of Hyperpolarized Light	15
		2.3.2	Biological mechanisms of Hyperpolarized Light	15
		2.3.3	Application of Hyperpolarized Light	16
		2.3.4	Bioptron device	16
		keletal proteins	18	
		2.4.1	Importance of cytoskeletal proteins in the cell	18
		2.4.2	Tubulin	18
		2.4.3	Actin	23
		2.4.4	Similarities and dissimilarities between tubulin and actin	26
			tical techniques used	27
		2.5.1	DLS	27
		2.5.2	Turbidity as a measure of aggregation formation	28
		2.5.3	Characterization of actin and tubulin folding by raman spec-	
			troscopy	29
		2.5.4	Conductivity as a parameter for protein behaviour	29

3	Mat	terial and Methods	32
	3.1	Reconstitution	32
	3.2	DLS	33
		3.2.1 Hydrodinamic Diameter	33
		3.2.2 Zeta potential	34
	3.3	Turbidity	35
	3.4	Raman Spectroscopy	36
	3.5	Conductivity	37
	3.6	Data analysis	39
4	Res	ults	41
	4.1	DLS	41
		4.1.1 Hydrodinamic Diameter	41
		4.1.2 Zeta potential	48
	4.2	Turbidity	50
	4.3	Raman Spectroscopy	52
	4.4	Conductivity	54
		4.4.1 Conductivity in reconstitution buffer	54
		4.4.2 Conductivity in diluted buffer for tubulin	61
5	Disc	cussion	63
	5.1	DLS analysis	63
	5.2	Turbidity assays	64
	5.3	Raman Spectroscopy	65
	5.4	Conductivity analysis	66
6	Con	clusions and Future developments	69
$\mathbf{A}_{\mathbf{J}}$	ppen	dix	72
Bi	bliog	graphy	82

# Chapter 1

# Introduction

The cytoskeleton is a highly dynamic network composed primarily of microtubules and actin filaments, which together play essential cellular functions such as shape maintenance, intracellular transport, division and signaling. In recent years, increasing evidence has suggested that cytoskeletal proteins are not only structural elements but also active participants in the regulation of cellular bioelectricity and electrostatic interactions. This perspective opens the possibility that external physical stimuli, including electromagnetic fields (EMFs) could modulate cytoskeletal function in ways that are both scientifically interesting and clinically relevant.

The motivation for this thesis comes from two considerations. First, neurode-generative and psychiatric disorders such as Alzheimer's disease and depression are strongly associated with cytoskeletal dysfunction, including microtubule destabilization and actin dysregulation. Second, photobiomodulation and related EMF-based therapies have gained attention as non-invasive approaches for modulating cellular processes but their molecular mechanisms of action remain poorly understood. The study of how tubulin and G-actin respond to external irradiation in simplified experimental systems therefore provides a unique opportunity to clarify fundamental principles and explore potential translational applications.

The aim of this work was to investigate the biophysical effects of light stimulation on purified tubulin and actin, focusing on their structural, electrostatic and conductive properties. Two distinct light-based devices were employed: Bioptron, which delivers polarized broad-spectrum visible light, and Vielight, which applies single-frequency near-infrared stimulation. The combination of these devices allowed for a comparative analysis of how different irradiation characteristics affect cytoskeletal proteins.

A multi-technique experimental strategy was implemented. Dynamic Light Scattering (DLS) was used to measure the hydrodynamic diameter and zeta potential, turbidity assays monitored polymerization dynamics, Raman spectroscopy analyzed molecular vibrations and conductivity measurements determined charge transport

properties in solution. Together, these complementary approaches provided a comprehensive view of how tubulin and G-actin respond to EMF exposure under controlled buffer conditions.

The structure of this thesis reflects both the logical progression of the experimental work and the interpretative framework developed around the findings. Following this introductory chapter, Chapter 2 presents the state of the art, reviewing current knowledge on photobiomodulation and EMF effects on proteins, the structural biology of tubulin and actin, the role of the cytoskeleton in health and diseases. Chapter 3 details the materials and methods employed in the experimental analyses. Chapter 4 reports the results, organized according to the different assays (DLS, turbidity, Raman spectroscopy and conductivity) and provide initial interpretations. Chapter 5 is devoted to a comprehensive discussion of the findings, integrating them with the literature and highlighting mechanistic insights. Finally, Chapter 6 presents the conclusions and possible future developments, with an emphasis on potential therapeutic applications of EMF-based devices.

In summary, this thesis seeks to address an emerging question in biophysics and biomedical engineering: can external light stimulation influence the behavior of cytoskeletal proteins in ways that may ultimately be used for therapeutic benefit? By combining rigorous experimental measurements with a translational perspective, the work facilitates the connection between fundamental protein biophysics and innovative biomedical applications.

# Chapter 2

# State of the art

# 2.1 Electromagnetic Fields

Electromagnetic fields (EMFs) are a combination of electric and magnetic fields that oscillate and interact with each other. Both fields are invisible areas of energy (called radiation) that are produced by electricity. The pressure used to push electrons through the wire is called voltage, and it is what produces an electric field: if the voltage increases, so does the electric field (V/m). However, a magnetic field is the result of the flow of electrons through wires and increases in strength as the current increases ( $\mu$ T). When both types of field are combined, they cause electromagnetic radiation: the movement of charges creates a magnetic field and causes changes in the electric field.

# 2.1.1 The basics on Electric and Magnetic fields

#### Electric Field (E-field)

An electric field is a region around charged particles or objects within which force would be exerted on other charged particles or objects. It is measured in volts per meter (V/m) and the field lines emanate outward from positive charges and inward toward negative charges. [1]

#### Magnetic Field (B-field)

A magnetic field is a region around a magnetic material or moving electric charge within which the force of magnetism acts. It is measured in Tesla (T) or Gauss (G) (1T= 10,000 G) and the field lines form closed loops that flow from the north pole to the south pole of a magnet. [2]

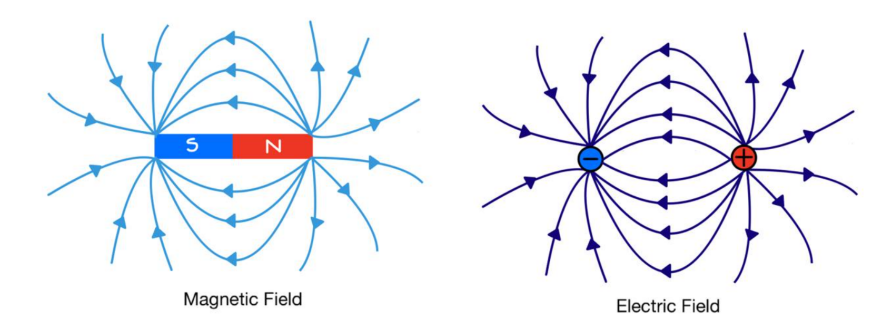


Figure 2.1: Comparison between magnetic and electric field lines

These two fields exist independently but when combined form electromagnetic waves that propagate through space. Electromagnetic fields can be classified as *static* (time-independent, such as those generated by permanent magnets or static charges) or *dynamic* (time-varying, produced by oscillating charges or currents). Antennas and other radiating structures are examples of efficient sources of dynamic EMFs.

#### Electromagnetic Fields as a vector

EMFs can be represented as a vector field with a magnitude and a direction. Both the E-field and the B-field can be expressed as vector quantities like:

- B for the magnetic field vector
- E for the electric field vector

The interaction between E and B is described by the Maxwell equations: a set of four equations that describe the behavior of electric and magnetic fields and how they relate to each other. [3] One of the central aspects of electromagnetism is that a change in the electric field generates a magnetic field and a change in magnetic field induces an electric field. This is a result of how these two fields interact as a unified force.

#### EMFs importance

EMFs come from natural sources (Earth's magnetic field, lightning, solar radiation) or artificial sources (power lines and electrical appliances, wireless communication devices and medical equipments). Understanding how these fields work could be essential in:

• Health and safety: knowing how they interact with the human body can be useful to protect the body from them or to use them for treatment;

- Scientific curiosity: EMFs play a crucial role in physics and cosmology;
- Technological applications: since they are part of our modern lifestyle, they can be exploited for good reasons;
- Regulation and policy: especially the artificial sources need laws to regulate them to ensure public safety.

#### 2.1.2 Generation of EMFs

EMFs can be generated from both natural and artificial sources and the motion of electric charges governs their generation. A moving or oscillating electric charge is the core of the formation of EMFs and the motion of these charges creates a magnetic field [4]. Varying these two fields over time allows the formation of electromagnetic waves. There are two ways in which EMFs are generated:

- Dynamic sources: these generate oscillating fields that can radiate into space (e.g. antennas) [5];
- Static sources: these generate static electric or magnetic fields (e.g. a bar magnet).

One of the most known natural EMF is the Earth's magnetic field, which provides a protective shield against cosmic rays and solar wind. Other natural sources include lightning, solar and cosmic radiation and the cosmic microwave background [Lewzuck2014].

However, artificial sources come from human activities and cover the entire electromagnetic spectrum (power lines, electrical wiring, appliances, communication systems, medical equipment, and industrial applications). The most efficient way to generate EMFs is by using antennas: alternating current (AC) is applied to the antenna to accelerate charges back and forth. This movement produces oscillating electric and magnetic fields and waves that propagate outward at the speed of light [6].

#### EMF Energy and Power

EMFs carry energy that can be transferred from one place to another. This relationship is expressed by the Poynting vector:

$$\vec{S} = \vec{E} \times \vec{H} \tag{2.1}$$

where  $\vec{S}$  is the Poynting vector,  $\vec{E}$  is the electric field vector and  $\vec{H}$  is the magnetic field intensity vector. The average power is proportional to the square of the electric field amplitude.

#### Maxwell's Equations

In the 19<sup>th</sup> century, James Clerk Maxwell unified knowledge of electricity and magnetism into four equations:

• Gauss's Law for Electric Fields:

$$\oint_{S} \vec{E} \cdot d\vec{A} = \frac{Q_{enc}}{\varepsilon_{0}} \tag{2.2}$$

expresses how the electric flux through a closed surface is proportional to the enclosed charge;

• Gauss's Law for Magnetism:

$$\oint_{S} \vec{B} \cdot d\vec{A} = 0 \tag{2.3}$$

states that there are no magnetic monopoles;  $\vec{B}$  always forms closed loops;

• Faraday's Law of Induction:

$$\oint_C \vec{E} \cdot d\vec{l} = -\frac{d\Phi_B}{dt} \tag{2.4}$$

indicates that a changing magnetic field induces an electric field;

• Ampere's Law with Maxwell's Addition:

$$\oint_C \vec{B} \cdot d\vec{l} = \mu_0 I_{enc} + \mu_0 \varepsilon_0 \frac{d\Phi_E}{dt}$$
(2.5)

shows that electric currents and changing electric fields generate magnetic fields;

#### Lorentz Force Law

Another important principle in electromagnetism is the Lorentz Force Law, which states that the total force acting on a charged particle due to electric and magnetic fields is equal to the sum of the electric and magnetic forces acting on it:

$$\vec{F} = q \left( \vec{E} + \vec{v} \times \vec{B} \right) \tag{2.6}$$

This is fundamental to understanding how fields affect particles, as in electric motors, mass spectrometers and cyclotrons.

#### Wave Equation and Electromagnetic Waves

Combining Maxwell's equations in vacuum leads to electromagnetic wave equations for the electric and magnetic fields:

$$\nabla^2 \vec{E} - \mu_0 \epsilon_0 \frac{\partial^2 \vec{E}}{\partial t^2} = 0 \tag{2.7}$$

$$\nabla^2 \vec{B} - \mu_0 \epsilon_0 \frac{\partial^2 \vec{B}}{\partial t^2} = 0 \tag{2.8}$$

These relations show that electromagnetic waves propagate in vacuum at the speed of light and are transverse in nature. The energy carried by an electromagnetic wave is stored in both electric and magnetic fields. The energy density is

$$u = \frac{1}{2}\epsilon_0 E^2 + \frac{1}{2}\frac{B^2}{\mu_0} \tag{2.9}$$

and the associated energy flux is described by the Poyinting vector. An important aspect of EMFs is that when they encounter the boundary between two media (e.g. air and glass), they are partially transmitted and reflected. Moreover, the propagation of EMFs through a material depends on:

- Permittivity: determines how much the electric field is reduced in the medium;
- Conductivity: affects the attenuation of electromagnetic waves;
- Permeability: determines how the magnetic field interacts with the material.

#### 2.1.3 The electromagnetic spectrum

The electromagnetic spectrum is the range of all types of electromagnetic radiation. It spreads from extremely low frequencies to high frequencies and each region of the spectrum has unique properties, effects and uses. All waves in the spectrum, even if they move at different frequencies, travel at the speed of light in vacuum (approximately 299 792 458 m/s) and are characterized by the equation:

$$c = \lambda \cdot f \tag{2.10}$$

Where c is the speed of light,  $\lambda$  is the wavelength (m) and f is the frequency (Hz). This equation explains how different waves interact with matter and how they can be used in some devices.

# Electromagnetic Spectrum AM FM TV Phones Radar Remote Bulb Tanning Bed Various Radioactive Elements Radio waves Microwaves Infrared Ultraviolet X-rays Gamma rays NON-IONIZING IONIZING

Figure 2.2: Electromagnetic Field Spectrum

Electromagnetic fields are generally divided into two main categories. High-frequency EMFs, such as X-rays and gamma rays, belong to the ionizing part of the spectrum. These high-energy photons can remove tightly bound electrons, creating ions, and are associated with DNA and cellular damage. In contrast, low-and mid-frequency EMFs, including static fields, power-line magnetic fields, radio waves, microwaves, infrared, and visible light, fall within the non-ionizing region. Their energy is insufficient to ionize atoms and they are generally not linked to direct DNA or cell damage [7, 8, 9, 10, 11].

# 2.1.4 Interaction of Electromagnetic Fields with Matter

The interaction of EMFs with matter occurs mainly through polarization, magnetization, and conduction. In dielectrics, electric fields displace bound charges, creating dipoles aligned with the field (polarization), which enables energy storage and modifies permittivity. Magnetic fields influence magnetic dipoles such as electron spins, aligning them and producing magnetization, which depends on permeability and magnetic order. In conductors, free charges move under electric fields, generating currents and Joule heating; the ease of this process is determined by conductivity.

How EMFs interact with matter depends strongly on frequency:

- Low frequencies (< 300 Hz to MHz) penetrate deeply, with induction effects dominating and pass through the body without significant absorption;
- Microwaves(300 MHz 300 GHz) interact strongly with polar molecules like water, causing dielectric heating [Geist2012];

- Infrared (300 GHz 400 THz and visible light 400-900 THz) excite atomic and molecular vibrations, producing heat, fluorescence or photoelectric emission;
- Ultraviolet radiation (790 THz 30 PHz) excites electrons and alters chemical bonds;
- X-rays (~30 PHz) and gamma rays (>30 PHz) penetrate deeply into tissues and materials, breaking bonds, causing ionization and damaging DNA.

Beyond frequency, interactions are also shaped by boundaries and material properties. At interfaces, waves can be transmitted, reflected, or absorbed: metals efficiently reflect radio waves, while transparent media transmit visible light. Scattering occurs when, for example, the wavelength matches the particle dimensions. In conductors, the skin effect confines fields near the surface, with penetration depth decreasing as frequency increases:

$$\delta = \sqrt{\frac{2}{\mu\sigma\omega}} \tag{2.11}$$

Finally, resonance phenomena can strongly enhance EM interactions. Examples include dielectric resonance in capacitors, magnetic resonance in MRI and ESR and plasmon resonance in metallic nanoparticles, all of which intensify local fields and enable applications in diagnostics, imaging, and nanophotonics.

# 2.1.5 Application of EMFs in medicine and health and safety considerations

EMFs are fundamental to many technologies, from powering household appliances to advanced communication systems and life-saving medical imaging. For example, Magnetic Resonance Imaging (MRI) uses a static magnetic field, magnetic gradients and radiofrequency pulses: it detects how nuclei respond to EMFs. Radiofrequency and microwave therapies use non-ionizing EMFs to selectively heat tumor tissue, leading to controlled hyperthermia and cancer cell death. In contrast, high-energy EMFs, such as X-rays and gamma rays, is ionizing and directly damages DNA, ysed in radiotherapy to destroy tumors. In addition, transcutaneous electrical nerve stimulation uses Low Frequency electric fields for pain management.

Although EMFs are essential for modern technologies, their potential effects on health and the environment are under scientific investigation and public debate. The biological impact of EMFs depends on frequency, intensity, exposure duration and the specific context in which they interact.

Static fields, such as those produced by DC power lines or MRI systems, generally have little biological impact, although strong magnetic fields may interfere with implanted medical devices, such as pacemakers. Extremely Low Frequency

(ELF) fields, below 300 Hz and typically generated by power lines and household appliances, can induce weak currents in tissues; some studies have suggested a possible association with childhood leukemia but the evidence is inconclusive.[9]

At higher frequencies, radiofrequency and microwave fields, emitted by mobile phones, Wi-Fi networks, ovens, and radar, primarily act through tissue heating caused by energy absorption. Hypotheses about non-thermal effects remain debated and unproven: to minimize thermal risks, regulations impose exposure limits expressed as the Specific Absorption Rate (SAR).[10]

At the upper end of the spectrum lie ionizing radiations such as ultraviolet light, X-rays, and gamma rays. These carry enough energy to ionize atoms, break chemical bonds and damage DNA, with well-established links to cancer and mutations. Their use in medicine and industry is therefore tightly regulated to ensure safety and minimize exposure risks.[7]

# 2.2 Photobiomodulation

#### 2.2.1 Definition of Photobiomodulation

Photobiomodulation (PBM), also known as Low-Level Laser Therapy (LLLT), refers to the therapeutic use of light (the visible o near-infrared spectrum) emitted by non-ionizing sources such as lasers, LEDs or broad-spectrum lamps to modulate cellular behavior in a non-thermal manner. [12] This form of light therapy is characterized by its low energy output, without causing tissue heating while inducing photophysical and photochemical responses: this characteristic is what distinguishes PBM from photothermal or ablative therapies. The wavelength range corresponds to the so-called optical "window of tissue", where absorption is relatively low and penetration depth is maximized, enabling light to reach intracellular targets.

Light interacts with natural chromophores (molecules that absorb specific wavelengths), initiating downstream effects without directly damaging tissue. [13] Photobiomodulation includes incoherent (LED) and coherent (laser) light sources and has been defined by multiple sources as a non invasive and controlled intervention that stimulates endogenous processes. The light spectrum is in the range from 400 nm in the visible to 1100 nm in the near-infrared, aligning with peaks of tissue penetration and chromophore absorption. [14] PBM is a non destructive process that does not rely on heat or ablation to produce its effects. Instead, it makes use of the low-level energy input to trigger specific changes through light absorption and photon-tissue interactions. [15]

#### 2.2.2 Biological mechanisms of PBM

Photobiomodulation operates through light absorption by intracellular chromophores, such as cytochrome C-oxidase (CCO) inside mitochondrial compounds IV. Absorption of photons by CCO leads to enhanced electron transfer, increased mitochondrial membrane potential and elevated production of ATP.[16] This type of stimulation raises Reactive Oxygen Species (ROS) levels: they act as secondary messengers that modulate signaling pathways and gene expression.[17] Moreover, PBM affects intracellular calcium levels and downstream mediators, such as cytokines and growth factors: this improves cellular metabolism and adaptive responses.[18]

Few evidences suggest that PBM also influences cell membrane transporters and signaling receptors, broadening its mechanistic scope.[19]

Photobiomodulation can modulate cytoskeletal proteins through photophysical and biochemical pathways. For example, exposure of tubulin or microtubules to near-infrared light can induce structural disassembly that leads to a reduction in polymerization rates and alterations in microtubule stability in vitro. Interesting is that PBM's effects on tubulin appear concentration dependent: at high protein concentration, it appears to enhance polymerization and total polymer mass after irradiation.[20] In addition, Raman Spectroscopy has revealed that near-infrared PBM can trigger transitions in tubulin secondary structure: a decrease in  $\alpha$ -helix and increase in  $\beta$ -sheet content, leading to a destabilization of microtubule organization.[21] Similarly to tubulin, PBM causes reorganization of actin filaments in cells and restores cytoskeletal integrity under stress or nutrient-deprived conditions.[22]

## 2.2.3 Application of PBM

PBM has been widely applied clinically since it is not invasive, has a favorable safety profile and cost-effectiveness. This therapy has effects in alleviating pain and inflammatory responses associated with musculoskeletal conditions and sport injuries and it also stimulates hair growth and reduces fat deposits.[23] In dermatology, PBM is used to treat acne, promote wound healing and skin rejuvenation.[24] Furthermore, PBM has demonstrated therapeutic potential in neurological disorders: few studies indicate positive outcomes for stroke, Parkinson's disease, Alzheimer's disease and major depressive disorder.[25]

Preclinical studies demonstrate consistent mitochondrial responses, while clinical outcomes are more heterogeneous, reflecting the sensitivity of PBM to dose-response relationships and treatment parameters. Photobiomodulation has recently been investigated as a potential cancer therapy. Evidence suggests that PBM may mitigate side effects of conventional treatments and could even act as a therapeutic option. [26] Some *in vivo* studies indicate that PBM can inhibit tumor growth; for example, [27] reported reduced proliferation of cancer cell lines in animal models, suggesting possible anti-cancer effects. However, other studies present conflicting

data. [28] and [29] found that, under certain conditions, PBM could enhance tumor aggressiveness.

#### 2.2.4 Vielight device

Vielight is a pioneering company in the field of photobiomodulation that specializes in transcranial and intranasal light-based brain stimulation devices designed to promote mental wellness, cognitive functions and systemic health. The proprietary Vie-LED technology delivers near-infrared light with laser-like energy profiles to modulate brain activity in a non invasive manner. In addition, Vielight's therapeutic devices operate by delivering controlled photonic energy to identified brain networks, engaging neural oscillation entrainment, enhancing functional connectivity and promoting neuroplasticity and mental wellness. The integration of smart app control and protocol customization allows both researchers and users to precisely adjust stimulation parameters, addressing needs ranging from cognitive enhancement and stress relief to meditation support.

#### Neuro Pro1 with nasal applicator

Neuro Pro1 is a wearable device that delivers transcranial-intranasal photobiomodulation via a headset and an intranasal applicator. The nasal applicator offers a targeted intranasal delivery of near-infrared light and it serves as an efficient accessory to the Neuro Pro system, providing consistent photonic stimulation through nasal passages, an access route that bypasses hair and skull that enables unique engagement with the olfactory region and deeper brain areas.



Figure 2.3: Vielight Neuro Pro1 with nasal applicator

The device has the ability to experiment with different exposure times, a parameter that can be changed in order to investigate different outcomes. The Neuro Pro comes with the Neuro Pro app installed on a presynced smartphone and it is possible to customize certain parameters such as power density and pulse rate, as shown in Table 2.1

Table 2.1: Vielight Neuro Pro1 - Device specifications

Parameter	Specification
Wavelength	LED (810 nm)
Frequency pulse	10 Hz
Power setting	80%
Power density	$60 \text{ mW/cm}^2$
Run time	Tunable
Duty cycle	50%

#### Neuro Pro2

Therapeutically, the Neuro Pro 2 is engineered to improve cognition, memory, focus, sleep, creativity, and mental clarity through both its Alpha (10 Hz) and Gamma (40 Hz) pulsing modes. The Alpha mode supports relaxation, mindfulness, and learning, while the Gamma mode enhances focus, processing speed, and brain energy. This device also comes with a pre-synced smartphone where it is possible to customize some parameters shown in Table 2.2



Figure 2.4: Vielight Neuro Pro2

**Table 2.2:** Vielight Neuro Pro 2 — Device specifications

Parameter	Specification	
Wavelength	LED (810 nm )	
Frequency pulse	Programmable from 1 to $10000\mathrm{Hz}$	
Power setting	Adjustable from 0% to 140%	
Power density	Up to $400 \mathrm{mW/cm^2}$ (per module)	
Run time	Tunable	
Total output power	Up to $12000\mathrm{mW}$	
Phase control	Phase A and B (synchronous/asynchronous	
	patterns)	
Sweeps / coupling	Frequency sweep, power sweep, and cross-	
	frequency coupling	
Nasal applicator	810 nm LED; max $100 \mathrm{mW/cm^2} \times 2$ units	

# 2.3 Hyperpolarized Light

## 2.3.1 Definition of Hyperpolarized Light

Light, as an electromagnetic wave, comprises oscillating electric and magnetic fields. Polarization refers to the restriction of these oscillations to specific planes or patterns, commonly linear, circular, or elliptical.[30][31] Linear polarization confines the electric field to one plane, while circular and elliptical polarization involve rotation of the field vector, achieved with optical elements such as wave plates. These properties are crucial in optical sciences, telecommunications, and biomedical applications.

Hyperlight therapy uses specific wavelengths of light (350–3400 nm) to penetrate tissues and promote cellular-level healing. The light beam is polychromatic, incoherent and highly polarized, with approximately 95 % linear polarization, referred to as Hyperpolarized Light. [32]. This light is generated when conventional diffuse light (such as a halogen lamp) passes through an optical polarization system, resulting in perfectly photon wave oscillation in a singular linear plane. [33] Hyperpolarized light improves penetration into deeper tissue layers without introducing heat or damaging tissues, allowing it to reach approximately 1 cm below the skin surface.

Advanced approaches incorporate nanophotonic structures, including fullerene C60 molecules embedded in polymers, producing complex twisting polarization patterns described using Fibonacci sequence geometries and toroidal energy distributions. [34] The resulting output combines linear and circular polarization components, called 'quantum hyperlight'.

It is considered therapeutic because it has a biostimulative capacity: this kind of light enhances cellular metabolism, immune response, tissue regeneration and wound healing by improving microcirculation and promoting cell membrane energy dynamics.[35]

# 2.3.2 Biological mechanisms of Hyperpolarized Light

Hyperpolarized light exerts therapeutic effects primarily through biostimulation of cellular functions, including energy metabolism, membrane organization, immune modulation, and vascular improvement.[33] If this light is absorbed by the lipid bilayers of the cellular membrane, lipid molecules can be realigned to improve membrane fluidity and function, nutrient exchange and cell signaling.[36] Because it is similar to other photobiomodulation methods, it increases intracellular ATP production by stimulating mitochondrial enzymes and improving electron transport. In addition, hyperpolarized light improves blood circulation and oxygen delivery by stabilizing red blood cell membranes and enhancing their oxygen- carrying function.

Hyperpolarized light could indirectly influence the cytoskeleton by facilitating

the dynamic assembly/disassembly of actin filaments and microtubules, which rely on ATP-driven polymerization cycles. Enhanced mitochondrial ATP production supports the energy demands of actin nucleation and tubulin polymerization. Furthermore, polarized light can affect cell signaling pathways that regulate cytoskeletal remodeling, such as Rho GTPase pathways that are known to orchestrate actin filament dynamics and microtubule organization in optogenetic studies.

## 2.3.3 Application of Hyperpolarized Light

Hyoperpolarized light is applied across multiple therapeutic domains, optimizing its safety and deep tissue penetration. In dermatology and skin rejuvenation, clinical data show improvements in skin firmness and elasticity, reduction of wrinkles and increased collagen and elastin production through fibroblast activation. For these reasons, it is often used in cosmetic applications as anti-aging treatments. With regard to wound healing and regeneration, hyperpolarized light accelerates wound repair, supports healing of ulcers and surgical sites. Moreover, hyerpolarized light alleviates chronic and acute pain, reduces inflammation and supports recovery in sports injuries and joint pain. [33]

## 2.3.4 Bioptron device

The Bioptron MedAll is a modern LED-based photobiomodulation system designed for both professional and home use. This portable device emits incoherent, polychromatic light in the visible and near-infrared spectrum, typically spanning wavelengths from 350 to 1550 nm, ensuring deep gentle tissue penetration without generating heat. A defining feature of MedAll is its high degree of linear polarization, commonly around 95%, which improves directional light delivery and optimizes interaction with tissue structures.

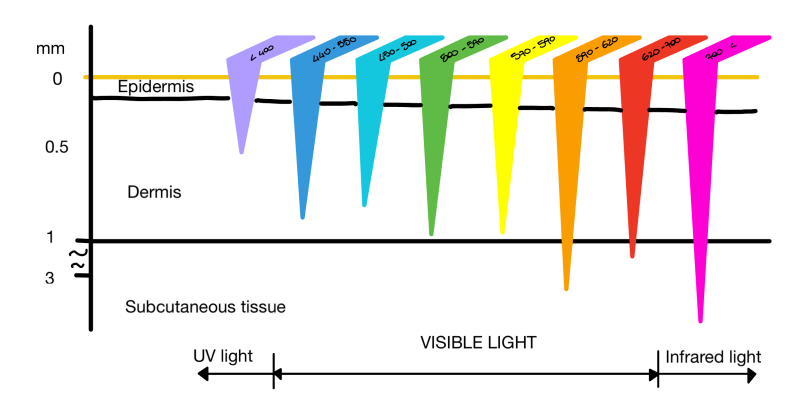


Figure 2.5: Bioptron spectrum

Designed for easy use, MedAll includes user-friendly settings, such as preset time modes (e.g. 3, 6, or 9 minutes) and adjustable intensity control, allowing users to adjust sessions to specific needs. It incorporates automatic timers and a lightweight, ergonomic housing that facilitates ease of handling in various areas of the body, from dermatology to wound care. This type of device has a fixed power density setting of  $40\,\mathrm{mW/cm^2}$  and an energy output of  $2.4\,\mathrm{J/cm^2}$  per minute. The device has a beam diameter of 5 cm, allowing the radiation to be evenly distributed. Being a mobile unit, it can be placed in any direction or angle and remains stable during irradiation.

Therapeutically, Bioptron MedAll supports wound healing, reducing inflammation, pain relief, and regeneration of superficial skin tissues. Its broad-spectrum, low-level light promotes mitochondrial activation, enhances collagen production, and modulates microcirculation, contributing to improved cell function and tissue repair. Importantly, its low energy density ensures a comfortable treatment experience with minimal risk. As a compact and versatile device, the MedAll exemplifies the accessibility of photobiomodulation technology for everyday clinical and consumer applications.



Figure 2.6: Bioptron MedAll

ParameterSpecificationLight sourceHalogen LampWavelength range350-1550 nmPolarization95%Power setting100%Power density $40 \text{ mW/cm}^2$ 

Tunable

50%

Table 2.3: Bioptron MedAll -Device specifications

# 2.4 Cytoskeletal proteins

Run time

Duty cycle

#### 2.4.1 Importance of cytoskeletal proteins in the cell

The cytoskeleton is a complex network of tubules and protein filaments that gives structural support, mechanical strength and shape to the cell. This structure maintains the integrity of the cell by organizing its internal components, enabling cellular movement and facilitating intracellular transport. The cytoskeleton is composed of three main types of proteins: microtubules, actin filaments and intermediate filaments.

Microtubules form a scaffold that supports cell shape and provides tracks for the transport of organelles and vesicles. Actin filaments are mainly involved in cell movements and shape changes but they are also important for processes like cytokinesis, endocytosis and muscle contraction. Intermediate filaments provide mechanical support and contribute to the preservation of cell resistance under mechanical stress.

The cytoskeleton is also essential for cell signaling because it links extracellular signals to cellular responses. With microtubules forming the mitotic spindle, it also regulates cell division. Severe diseases such as cancer, neurodegenerative disorders and developmental abnormalities can be the result of cytoskeletal disfunctions. [37]

#### 2.4.2 Tubulin

#### Overview of the protein: $\alpha$ and $\beta$ subunits

Tubulin is a globular protein produced in eukaryotic cells [38]. This protein is the building block of microtubules, so it plays an important role in maintaining cell shape, facilitating cell division, enabling intracellular transport and supporting

the structural integrity of neurons. Tubulin is also involved in cell signaling: microtubules can interact with signaling molecules and modulate signal transduction pathways. This influences the cellular response to external stimuli. Furthermore, this protein is involved in specialized cellular structures, such as the flagella and cilia, which are crucial for sensory functions and cell motility. [39]

The term 'tubulin' was coined by Professor Hideo Mohri in 1968 to name the unit of microtubules and, after that, became a focal point of cell biology and pharmacology due to its implications in various diseases. [40]

This protein exists in different isoforms:  $\alpha$ ,  $\beta$ ,  $\gamma$ ,  $\delta$ ,  $\epsilon$  and  $\zeta$ .  $\gamma$ -tubulin is essential for microtubule nucleation in centrosomes, while the other isoforms are more specialized and often found in basal bodies and centrioles. The  $\alpha$  and  $\beta$  monomers of tubulin exist as isotypes differing in their ammino acid sequence encoded by different genes[41], their mass is around 50 kDa and are in a similar range compared to actin (with a mass of 43 kDa). Both $\alpha$  and  $\beta$  tubulin spontaneously bind to form a stable heterodimer subunit of approximately 100 kDa (diameter 7 nm), where the  $\beta$ - subunit is +ve and the  $\alpha$ -subunit is -ve[42]. The surface of the tubulin dimer shows a predominantly negative electrostatic potential.



Figure 2.7: Tubulin hetero-dimer  $\alpha$  (yellow) and  $\beta$  (blue) subunits

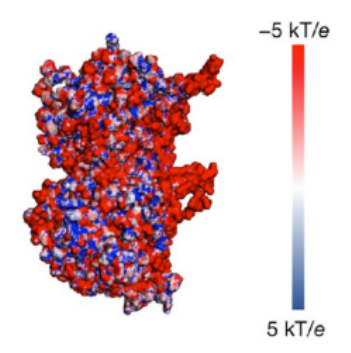


Figure 2.8: Electrical distribution of charge in tubulin

Both units are stored in eukaryotes and are essential for numerous cellular processes. Despite their structural similarities,  $\alpha$  and  $\beta$  tubulin have different functional and biochemical properties. They are both made of 450 amino acids and share about 40% amino acid identity and fold into a highly conserved tertiary structure composed of a core of two  $\beta$ -sheets surrounded by alpha helices. The main difference between these subunits is in the amino acid sequence in a specific region, which leads to a different way to bind and hydrolyze GTP (Guanosine Tri-Phosphate). Although both subunits bind to GTP, only  $\beta$ -tubulin is involved in GTP hydrolysis: this subunit plays an important role during polymerization and depolymerization dynamics.  $\beta$ -tubulin hydrolyzes GTP in GDP and this reaction

influences the stability of microtubules and structural changes. [41]

The heterodimer has a polar nature, a characteristic that is crucial for the directional behavior of microtubules: the  $\alpha$ -tubulin defines the minus and the  $\beta$ -tubulin defines the positive end.

Some tubulin dimers may have functions that do not involve the formation of microtubules: factors like geometry, dynamics and protein-protein interactions impose certain constraints on tubulin evolution and account for the high degree of conservatism in the amino acid sequences of both  $\alpha$  and  $\beta$  tubulin. [43]

#### Dynamics of Microtubules Assembly

Microtubules are rigid hollow cylinders made by polymerization of  $\alpha$  and  $\beta$  tubulin dimers. This process is reversible: in the backward reaction, microtubules depolymerize into tubulin dimers, while in the forward reaction, tubulin dimers bind non covalently and assemble into protofilaments, which subsequently associate to form microtubules.

The process of microtubule assembly starts with a structure known as the Microtubule Organizing Center (MTOC), where  $\gamma$  tubulin and other associated proteins form the complex  $\gamma$ -tubulin ring ( $\gamma$ -TuRC) that nucleates microtubule growth. Subsequently, the  $\alpha$ - $\beta$  tubulin heterodimers align longitudinally to form protofilaments, which typically assemble into 13 parallel protofilaments that organize into a helical network, creating the cylindrical architecture of microtubules. The lateral interactions between the dimers involve electrostatic and hydrophobic interactions: these phenomena contribute to the mechanical strength and flexibility of the microtubule.

Polymerization of tubulin occurs because the  $\alpha$  and  $\beta$  monomer bind to Guanosine –5'-Triphosphate (GTP): in the  $\alpha$ -tubulin the GTP remains exposed to inside while on the  $\beta$ -tubulin is outside. The GTP bound to  $\beta$ -tubulin is hydrolyzed to Guanosine-5'-Diphosphate (GDP). GTP hydrolysis is essential for microtubule dynamics and stabilization of the microtubule plus end has been attributed to the presence of a GTP-tubulin cap, so rapid depolymerization occurs.

The charge distribution on the tubulin dimer is fundamental to its function in polymerization: both  $\alpha$  and  $\beta$  tubulin contain charged residues in their structure, which facilitates electrostatic interactions between the GTP binding sites of the  $\alpha$  and  $\beta$  subunits. The microtubule exhibits polarity, with one end known as the 'plus end', where polymerization is faster and the other called 'minus end', where polymerization is slower. The minus end is anchored at the MTOC while the plus end is oriented towards the cell periphery.

Microtubules exhibit electrical properties: each tubulin dimer, under physiological pH, carries a charge of -52 e, with approximately 46% (-24 e) located at the c-termini of the monomers. [44] This charge is due to Aspartic and Glutamic Acid

residues, which are approximately 49% of the c-terminal amino acids. This uneven charge distribution gives each monomer a permanent dipole moment of roughly 4000 D. Within, the radial arrangement of tubulin amplifies this dipole, generating electrostatic polarity along the microtubule axis and length of the dipole moment.

The 'dynamic instability' is the process that regulates the dynamics of microtubule polymerization: this refers to the ends of microtubules where they grow rapidly[45]. In fact, when the concentration of GTP tubulin dimers is high, the microtubules tend to grow by adding more dimers to the plus end, maintaining a GTP cap that stabilizes the structure. However, when the concentration of GTP tubulin decreases, the GTP cap is lost, which leads to a rapid transition to depolymerization. Microtubules are essential structures for cell function and include mitototic and meiotic spindles (ensuring correct division of cells), anoxemes (molecular machines of cilia and flagella) and the neuronal cytoskeleton (controls the function of neurons and connectivity) [46]

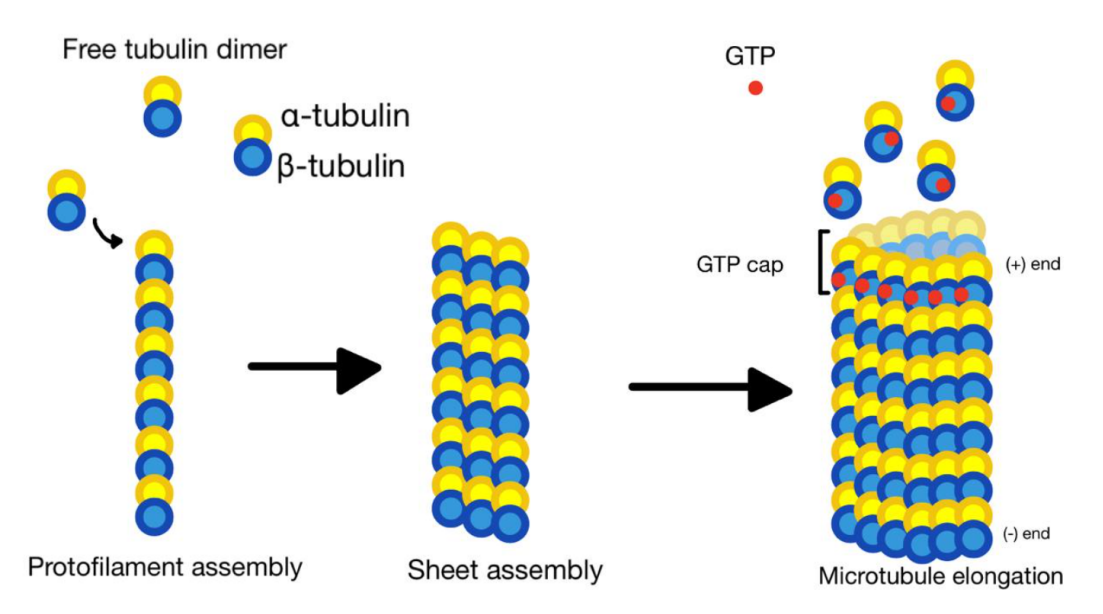


Figure 2.9: Process of Microtubule Assembly

#### Post-translational modifications of tubulin

To regulate its functions and dynamics, tubulin uses post-translational modifications (PTMs): these modifications influence microtubule stability, assembly and interaction with other cellular proteins, after tubulin is synthesized.

The most common PTMs are acetylation, tyrosination, detyrosination, phosphorylation, polyglutamylation and others. Acetylation of tubulin, such as on lysine of  $\alpha$  tubulin, is associated with stable and long-lived microtubule. This kind of modification is found in the flagella and cilia and plays a role in microtubule-based motility. Tyrosination in microtubules makes them more dynamic while detyrosinated microtubules are more stable and associated with centrosomes and stable microtubule arrays. Phosphorilated tubulin can alter microtubule dynamics, especially during mitosis: this modification regulates the assembly and disassembly of microtubules during cell division, contributing to the formation of the mitotic spindle. Lastly, polyglutamylation can influence microtubule interactions with other cellular proteins and is involved in controlling microtubule stability. All these modifications have a role in the response of cellular needs, influencing processes like motility, cell division and intracellular transport. [47]

#### Biological significance

Tubulin exists in different isotypes and, although they are structurally similar, they have unique expression patterns and functional roles in specific tissues. Their differences influence microtubule dynamics and are related to diseases such as

cancer and neurological disorders. [48] For example, mutations in tubulin genes (tubulinopathies) cause severe neurodegenerative diseases such as Alzheimer's disease: this disorder is associated with hyperphosphorylation of tau protein that dissociates from microtubules. This leads to microtubule destabilization, impaired axonal transport and neuronal death.

#### 2.4.3 Actin

#### Structural characteristics of actin

Actin is a protein (mass 43 kDa) composed of 374 amino acids with a monomeric globular form called G-actin. This monomer is divided into four subdomains: subdomains I and II form the outer layers and subdomains III and IV form the inner region. These domains are held together by a deep nucleotide-binding cleft that holds ATP and a divalent cation ( $Mg^{2+}$  or  $Ca^{2+}$ ) while DNAse-I binding (D-loop) in subdomain II can adopt multiple conformations with changes in nucleotide state. [49]

Actin consists of two major domains connected by two links, forming upper and lower clefts. The upper cleft binds ATP and  $\mathrm{Mg^{2+}}$ , while the lower cleft is hydrophobic and serves as a binding site for Actin-Binding Proteins (ABPs) and inter-subunit contacts. ATP hydrolysis triggers subtle conformational changes, mainly in the  $\mathrm{Ser_{14}}$   $\beta$ -hairpin loop and the sensor loop (His<sub>73</sub>), which modulate the stability of actin filaments. The D-loop in domain II is also involved in filament contacts. Hydrolysis weakens interactions, allowing rotational flexibility: this may activate  $\mathrm{Gln_{137}}$  to facilitate the catalysis of gamma-phosphate during filament formation.

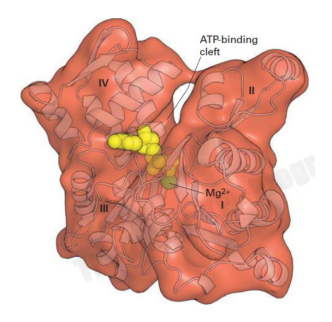


Figure 2.10: Monomer of G-actin

Two stranded helycal polymers of G-actin units form a filament called F-actin. The filament has a diameter of 7 nm and is composed of 14 subunits, with distinct barbed (+) and pointed (-) ends based on subdomain orientations. [50]. The transition from monomer to filament involves a flattening of the monomer and a

reorganization of water molecules and key residues such as  $Gln_{137}$  and  $His_{161}$  in the nucleotide cleft.

#### Function of actin in the cell

Since Straub's discovery of actin in muscle tissue in 1942 [51], actin has been proven to be the most prevalent cytoskeleton protein in many eukaryotic cells: it represents around 5% of the total protein in eukaryotic cells and can reach 10% in specific types of cells, such as muscle and microvilli-containing cells. [52]

G-actin and F-actin contribute to fundamental cellular processes such as intracellular transport, where actin-based motors like myosins move cargo along actin filaments.

Actin is involved in cytokinesis where it forms the contractile ring with myosin that drives cell division in many animal cells. Furthermore, in non-muscle cells, stress fibers (actin filaments organized with myosin and linking proteins) play a role in maintaining mechanical tension and regulating cell morphology and attachment to focal adhesions.[53]

Actin has a wide range of actin-binding proteins that allow it to modulate mechanical stiffness, organelle organization and signal transduction. In addition, the interaction of filamentous actin with myosin forms the basis of muscle contraction. Due to its central role in the cell, the actin cytoskeleton is also disrupted or taken over by numerous pathogens.

#### Dynamics of actin filament assembly

Actin filaments are rapidly assembled and disassembled, allowing them to generate force and support cell movement. The F-actin assembly consists in three phases: nucleation, elongation and steady state. This dynamic process is finely tuned by ABPs, nucleotide binding and environmental factors. In the first phase, two or three G-actin monomers slowly join to form a small oligomer (dimer or trimer) that will nucleate. Spontaneous nucleation is energetically unfavorable but it is catalyzed by nucleators such as the  ${\rm Arp}_{2/3}$  complex and formins:  ${\rm Arp}_{2/3}$  promotes the formation of branched filaments, while formins assemble linear filaments by stabilizing the (+) end and recruiting profilin-bound G-actin monomers.[54]

The second phase is the moment when the actin filament rapidly grows by adding actin-ATP-monomers to both ends: the monomers are added to the filament to the (+) end ten times faster than (-) end. Profilin enhances this process by catalyzing ADP to ATP exchange on G-actin and delivering ATP-G-actin to formin-mediated elongation.

In addition, with the filament occurs the hydrolysis of ATP, which triggers conformational changes toward the filament exterior. In the last phase, an equilibrium is reached, and the G-actin monomers join and leave the filament at the same rate

to maintain the filament's length (around 74 nm): the rate of subunit addition at the barbed end balances the rate of subunit dissociation at the pointed end. Since most monomers bind to the (+) end, there is a phenomenon called "treadmilling" where monomers are added to the (+) end and falling from the (-) end to maintain the length of the filaments.[55] These dynamics are strongly influenced by various acting-binding proteins such as profilin and thymosin.

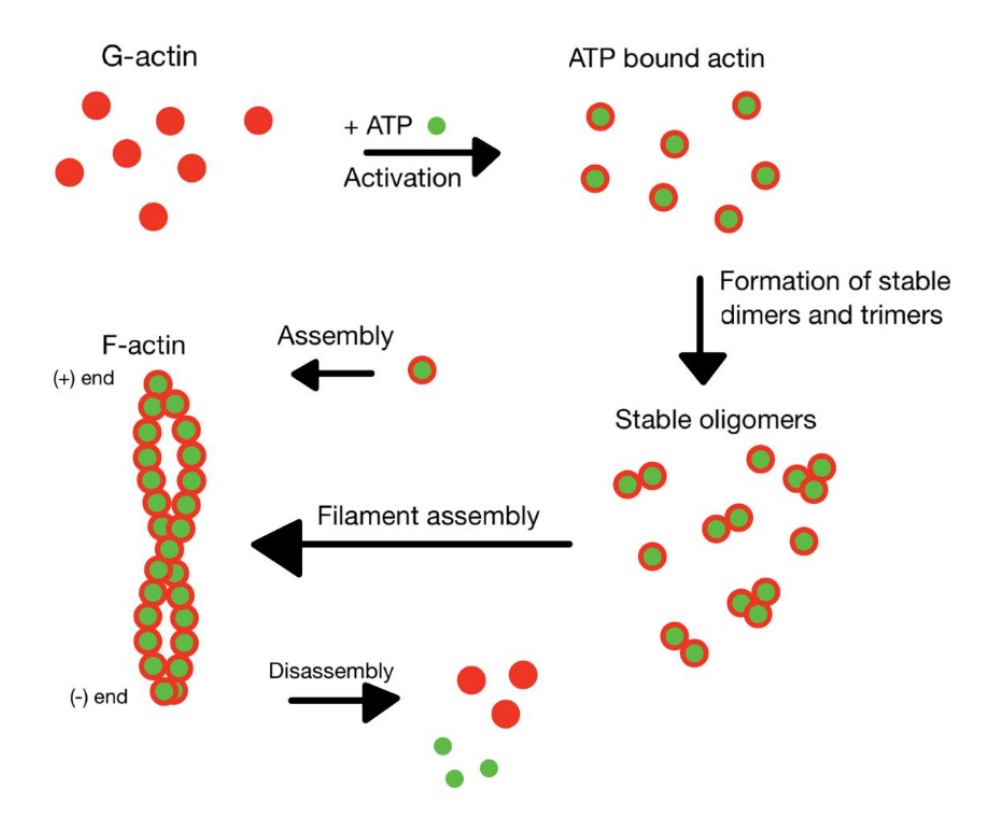


Figure 2.11: Dynamic of f-Actin Assembly

Nucleotide hydrolysis regulates the dynamic of actin filaments, with ATP-actin favoring assembly and ADP-actin promoting disassembly at the pointed end. ABPs bind to the actin cleft using amphipatic helices in various orientations. Proteins like gelsolin cut filaments upon Ca<sup>2+</sup> activation, profilin maintains the monomer pool and promotes barbed-end elongation, ADF/cofilin binds ADP-actin and promotes depolymerization and RPEL domains in nuclear regulators bind G-actin to modulate transcription. [49]

Another important molecule in the actin assembly is tropomodulin, which caps at the pointed end stabilize the filament length and prevent spontaneous subunit loss.

Polymerization kinetics are also modulated by molecular crowding, filament

packing and diffusion limits. Modifications such as ionic strength and the presence of  $Mg^{2+}$  or  $Ca^{2+}$  significantly affect actin addition rates and filament stability.[56]

ATP hydrolysis influences filament length fluctuations and growth velocity on the single filament: in high concentrations of G-actin, ATP caps remain large and govern the variability of length while at low concentrations, the spontaneous dissociation of ADP-actin becomes significant. [55]

#### Post-translational significance

Actin undergoes a wide range of post-translational modifications (PTMs) including His<sub>73</sub> methylation, N-terminal acetylation and argylation common in non muscle  $\beta$  -actin, phosphorylation, oxidation.

If a PTMs becomes aberrant, it can cause diseases such as dysregulated acetylation or methylation can impair actin's intrinsic interactions, thereby disrupting cytoskeletal organization in cancer cells. In cancer, these aberrations can cause changes in cell migration and mechanical stiffness. [49] For example, filament's destabilization can be caused by excessive oxidative modification or phosphorylation under stress; these are also linked to neurodegeneration and cardiovascular diseases.

# 2.4.4 Similarities and dissimilarities between tubulin and actin

#### Comparison of structures and assembly mechanisms

Actin and tubulin are key components of the cytoskeleton, but they differ in structure and polymerization. Actin forms thin, helical filaments from monomeric G-actin, which are able to rely on ATP-binding and hydrolysis to regulate assembly. In contrast, tubulin is a heterodimer of  $\alpha$ - and  $\beta$ -subunits that polymerizes into cylindrical microtubules, with GTP-bound  $\beta$ -tubulin. Although actin filaments grow at both ends with a preference for the (+) end, microtubules exhibit polarized growth and sudden transitions between growth and shrinkage. [57] Actin nucleation is often regulated by formins and the Arp<sub>2/3</sub> complex, while microtubules are nucleated from  $\gamma$ -tubulin ring complexes in microtubule organizing centers,[48] These fundamental differences reflect their different cellular roles and spatial organization in the cytoplasm.

#### Differences in stability and regulation of filaments

F-actin and microtubules exhibit very different dynamic behaviors. Actin filaments are stable but continuously remodel through 'treadmilling', influenced by actin-binding proteins such as cofilin, profilin, and thymosin- $\beta 4$ . However, microtubules undergo dynamic instability, rapidly transitioning between growth and shrinkage

phases depending on GTP hydrolysis and microtubule-associated proteins such as Tau and MAP2. Post-translational modifications also contribute to the stability of microtubules, such as tubulin acetylation and detyrosination, while actin is regulated by phosphorylation and ADP/ATP exchange [58]. Furthermore, cellular signals involving Rho-family GTPases differentially affect actin and microtubule organization [59]. These differences in regulation and filament turnover are essential for specific cellular processes, including rapid cytoskeletal remodeling during cell migration, mitosis, and intracellular trafficking.

#### Implications for cellular functions and cytoskeletal biology

The structural and regulatory differences between actin and microtubules have profound implications for their cellular roles. Actin filaments are central to the generation of contractile forces in muscle cells, the maintenance of cell shape and the ability to move through lamellipodia and filopodia [60]. Microtubules serve as pathways for intracellular transport of organelles and vesicles through motor proteins such as kinesin and dynein and play crucial roles in mitotic spindle assembly and chromosome segregation [61]. Their spatial organization also differs: actin forms dense networks near the plasma membrane, while microtubules radiate from the centrosome. The crosstalk between the two networks ensures the coordination of cellular processes such as polarity and migration [62]. Disruptions in either filament system can lead to diseases including cancer, neurodegeneration, and cardiomyopathies, highlighting their importance in maintaining cellular homeostasis.

# 2.5 Analytical techniques used

#### 2.5.1 DLS

The hydrodinamic diameter measured by DLS reflects the apparent size of a protein as it diffuses through a solution. This size accounts for not only the protein's molecular dimensions but also its hydration shell and any aggregation or oligomerization that may occur. Under different conditions (e.g. varying PH, temperature, ionic strength or solvent composition), the hydrodinamic diameter can change and it gives the possibility to evaluate protein stability and detect aggregation. DLS offers high sensitivity for detecting even small aggregates that are often undetectable by other techniques: this makes this method very valuable in biopharmaceutical research and structural biology.

DLS can also measure the **zeta potential**, this method measures the surface charge of proteins in solution. Reflects electrostatic interactions between the protein and its surrounding medium and provides information regarding colloidal stability. If the proteins have high absolute zeta potential (positive or negative), they tend

to repel each other and remain dispersed. However, if the zeta potential is low, it indicates a risk of aggregation. Studying the zeta potential under various solvent or buffer conditions can help optimize protein formulations to minimize instability or aggregation. The combination of both measurements at DLS gives a comprehensive picture of the behaviour of proteins in solution. This information is essential in fields like nanomedicine, drug design and protein engineering.

Dynamic Light Scattering serves as an invaluable tool for the examination of actin and tubulin, given that these cytoskeletal proteins exist in dynamic states that are highly susceptible to environmental variations. Actin is capable of transitioning between its globular (G-actin) and filamentous (F-actin) forms, whereas tubulin dimers undergo polymerization into microtubules or depolymerization in response to factors such as temperature, pH, ionic strength, and the presence of binding agents. DLS facilitates the real-time observation of these transitions by quantifying the hydrodynamic diameter without altering the sample.

For actin, DLS can reveal nucleation events or filament growth. For tubulin, it detects dimer stability, assembly and disassembly, and it can highlight effects of drugs or external stimuli. DLS also identifies subtle aggregation or oligomerization, which is important for understanding protein stability and misfolding. When combined with a zeta potential, it clarifies surface charge changes influencing polymerization.

### 2.5.2 Turbidity as a measure of aggregation formation

Turbidty analysis is a widely used technique to monitor protein aggregation, such as dynamics proteins like tubulin. The cloudiness or optical density of a solution is measured by recording its absorbance at a specific wavelength. When proteins start to aggregate, they scatter light more effectively, leading to an increase in turbidity: this makes this analysis a direct and simple indicator of aggregate formation and stability in solution. [45, 44] Tubulin exists as dimers that polymerize to microtubules, so turbidity analysis provides a real-time view of polymerization kinetics. When the formation of microtubules occurs, the number and size of particles in solution increase, enhancing light scattering and absorbance. Changes in absorbance over time can be used to assess the rate and extent of polymerization. [39] This technique is advantageous because it is non-invasive, requires minimal sample preparation and can be conducted under physiological conditions. It can also detect subtle changes in protein behavior caused by environmental factors, chemical agents or physical stimuli. In the case of tubulin, turbidity analysis can reveal how small molecules, temperature changes or even electromagnetic fields affect polymer stability.

By tracking absorbance, researchers can quantify assembly dynamics, compare

experimental conditions and evaluate the effects of drugs or inhibitors on microtubule formation. Therefore, turbidity remains a reliable and informative method for studying protein aggregation and structural transitions in tubulin and related systems.[41]

# 2.5.3 Characterization of actin and tubulin folding by raman spectroscopy

Raman spectroscopy is an important analytical method for proving the structural features and folding of proteins. It is based on inelastic light scattering: incident photons interact with molecular vibrations, providing a fingerprint of structural motifs and chemical bonds. When applied to proteins, Raman spectroscopy is particularly sensitive to secondary structure (random coils,  $\alpha$ -helices and  $\beta$ -sheets) and tertiary packing. For cytoskeletal proteins with highly dynamic conformations like tubulin and actin, this analysis offers valuable insights into folding and stability: this structural information is essential for linking molecular conformation to cellular function and pathology. Tubulin alternates between soluble dimers and polymerized microtubules, while actin exists in monomeric (G-actin) and filamentous (F-actin) forms. The structural transitions between these states are essential in cellular functions. For example, backbone conformation can be detected by looking at changes in amide I and III bands, while local folding or unfolding events can be identified by specific side chain vibrations (e.g. aromatic residues and disulfide bonds).[49, 53]. Recent studies used Raman spectroscopy to monitor microtubule assembly. Raman spectra could reveal transitions in tubulin from  $\alpha$ -helix-rich to  $\beta$ -sheet-rich conformations under photobiomodulation. [63] These insights are important because microtubule-targeting agents, such as colchicine or taxanes, bind to tubulin and induce conformational changes in situ. However, actin studies showed the role of nucleotide binding and cofactor interactions in structural stability. Key vibrations in the phosphate and carbonyl regions reflect the ATP/ADP states, which modulate the assembly of the filaments. [50] Raman peaks related to aromatic residues and C-N stretching can indicate folding or denaturation.

## 2.5.4 Conductivity as a parameter for protein behaviour

Electrical conductivity is an important physical parameter for understanding the behavior of proteins in solution because it reflects how charges move and interact within a medium. For proteins such as actin and tubulin, which are highly charged cytoskeletal components, conductivity measurements can provide insight into folding, assembly, stability and interactions with ligands or external fields. Proteins in solution contribute to the conductivity through their surface charges and the ions associated with them. Actin and tubulin contain multiple acidic and basic

residues, which give them net negative charges under physiological pH. As they undergo structural transitions, the distribution of charges changes. This affects how counterions arrange around the protein, modifying the ionic environment and thus the conductivity of the solution. For example, polymerization can reduce the mobility of charged residues, altering conductivity, while depolymerization or unfolding can expose buried charges and increase ionic movement [49, 50]. External factors, such as temperature, ionic strength, cofactors (ATP for actin, GTP for tubulin) and binding drugs, also influence conductivity. Changes in conductivity can reveal conformational shifts or aggregation. In addition, conductivity studies under external electromagnetic fields or photobiomodulation are gaining interest; changes in electrical properties could indicate altered protein dynamics or surface charge reorganization [63, 44]. Because actin and tubulin assembly is critical for cell structure and intracellular transport, understanding how conductivity correlates with their states is useful in drug development, nanobiophysics and pathology research. For example, agents that disrupt microtubules (taxanes, colchicine) or actin filaments alter the electrostatic balance, detectable as changes in solution conductivity. Similarly, mutations that modify charge patterns can be studied through conductivity measurements.

To investigate the conductivity of proteins, it is important to use a method that minimizes artifacts of electrode polarization and contact resistance. For this reason, the direct current (DC) four-point probe (4PP) technique can be used. In this configuration, a constant current is applied through two outer electrodes in contact with the sample, while the voltage drop is measured between two separate inner electrodes. Because the inner electrodes draw a small current, the potential difference can be measured without the influence of contact resistance, ensuring that the results reflect only the intrinsic electrical properties of the sample. [64] This approach is particularly suitable for low-conductivity systems such as films with protein, where even small electrode effects could significantly distort the measurement. [65]

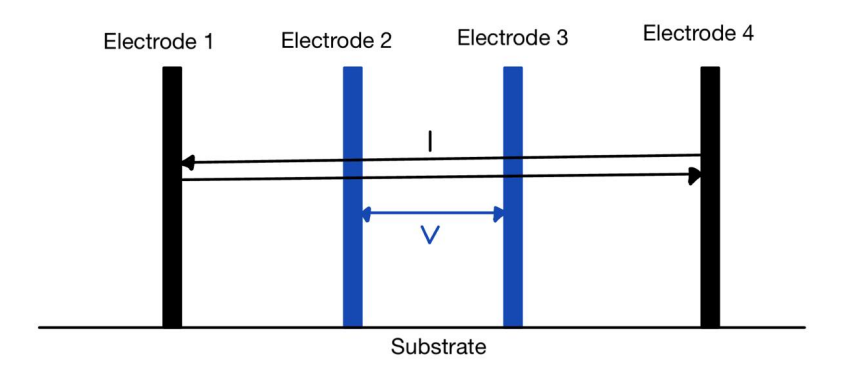


Figure 2.12: Schematic operation of Four-Point Probe

The 4PP directly provides the sheet resistance  $R_s$  of the sample. Since the resistance of the sheet is related to the resistivity  $\rho$  and the thickness of the sample t by the expression  $R_s = \rho/t$ , the conductivity can be obtained as

$$\sigma = \frac{1}{R_s \cdot t} \tag{2.12}$$

In this way, the technique provides a reliable and quantitative means of following structural or conformational changes in protein films through their electrical response.

The overview presented in this chapter underscores the relevance of electromagnetic fields and light-based stimulation in modulating cytoskeletal proteins such as tubulin and actin. To address the open questions identified in the literature, we designed a set of experiments that are introduced in the following chapter.

## Chapter 3

## Material and Methods

### 3.1 Reconstitution

#### Tubulin reconstitution

Tubulin has been reconstructed from 1 mg of lyophilized Porcine Brain Tubulin (Cytoskeleton, Tubulin protein (>99 % pure) source: Porcine Brain Cat #T240) as prescribed by the vendor. General Tubulin Buffer (80 mM PIPES, 2 mM MgCl2, 0.5 mM EGTA, pH 6.9, Cytoskeleton Inc, #BST01-010) was purchased in powder and reconstructed with de-ionized water and stored at 4 °C. Lyophilized tubulin was reconstructed using 20 µLof microtubule cushion buffer (General Tubulin Buffer supplemented with 60 % Glycerol, Cytoskeleton Inc, #BST-05-001) and 180 µL of G-PEM buffer (General Tubulin Buffer supplemented with 1 % GTP). The solution reached a final concentration of 5 mg/mL (45.45 µM). Tubulin solution was snap frozen in liquid nitrogen and stored in aliquots at -80 °C for subsequent use.

#### G-Actin reconstitution

The G-Actin has been reconstructed from 1 mg of lyophilized Rabbit Skeletal Muscle (Cytoskeleton, Actin protein (>99 % pure) source: rabbit skeletal muscle Cat #AKL99) in 250 µL of General Actin Buffer (Cytoskeleton, General Actin Buffer Cat #BSA01) to reach 4 mg/mL and by adding 0.5 µL of ATP (Cytoskeleton, Adenosine 5'-triphosphate disodium salt (ATP) Cat #BSA04, 100 mM stock) to yield a final ATP concentration of 0.2 mM. Also, 1.25 µL of DTT (100 mM stock) were added to reach a final concentration of 0.5 mM of DTT in the actin solution. The solution was incubated for one hour and then centrifugated at 4000 RPM for 20 minutes at 4°C. G-Actin solution was snap frozen in liquid nitrogen and stored in aliquots at -80 °C for subsequent use.

#### Irradiation with EMFs

Two different devices were used to irradiate the protein. The power density was fixated at  $40 \text{ mV/cm}^2$  so adjuments to the devices were made to irradiate the samples with the same amount of energy when the comparison between devices was done. Both devices were fixated at 12.5 cm away from the samples. During exposure the samples were stored at  $4^{\circ}\text{C}$  with the light off to not create interference with the radiation from the devices.

#### 3.2 DLS

#### 3.2.1 Hydrodinamic Diameter

#### Tubulin samples

DLS was performed using a final concentration of tubulin of 1.2  $\mu$ M and 1.4  $\mu$ M of colchicine solution in the presence of BRB8, as done by [66]. The colchicine solution was obtained by adding 2  $\mu$ Lof colchicine (dissolved in DMSO) into 498  $\mu$ Lof BRB8. BRB8 is a buffer obtained by a dilution of General Tubulin Buffer in a ratio 1:10. 17.6  $\mu$ L of colchicine solution was added to 0, 12, 24, 36 and 48  $\mu$ L of DMSO to create 0, 5, 10, 15 and 20 % DMSO (v/v) solution respectively. In every solution, 6.4  $\mu$ L of tubulin was added and the volume was made up to 240  $\mu$ L using de-ionized water.

#### G-Actin samples

DLS was performed using a final concentration of 1.2  $\mu$ M and 1.4  $\mu$ M of latrunculin solution in the presence of General Actin Buffer. The latrunculin solution was obtained by adding 2  $\mu$ L of latrunculin (dissolved in DMSO at 1 mM) into 498  $\mu$ Lof G-Buffer. 17.6  $\mu$ L of latrunculin solution was added to 0, 6 and 12  $\mu$ L of DMSO to create 0, 2.5 and 5 % DMSO (v/v) solution respectively. In every solution, 30.4  $\mu$ L of actin (previously diluted at 0.4 mg/mL with G-buffer supplemented with ATP and DTT) was added and the volume was made up to 240  $\mu$ L using de-ionized water.

#### DLS measurements for both protein

240  $\mu$ L of volume was sufficient to test the sample at 4 different time steps (0 – 3 – 6 – 24 h). For each time point 60  $\mu$ Lof solution were used. In addition, for each concentration of DMSO, 3 different samples were made to test a control, one stimulated with Bioptron (Bioptron MedAll) and one with Vielight (Vielight NeuroPro1 with Nasal applicator). The irradiations were done at 4°C: Bioptron

for 18:45 minutes and Vielight for 30 minutes. Between the different time points, the samples were sealed with aluminum foils and stored at 4°C in the dark.

The temperature of the system was set to 25 °C. The experiments were conducted using Nano-ZS (Malvern Instruments) at the Lewis's Laboratory (Edmonton, University of Alberta). Data acquisitions were performed by doing 5 measurements for each sample.

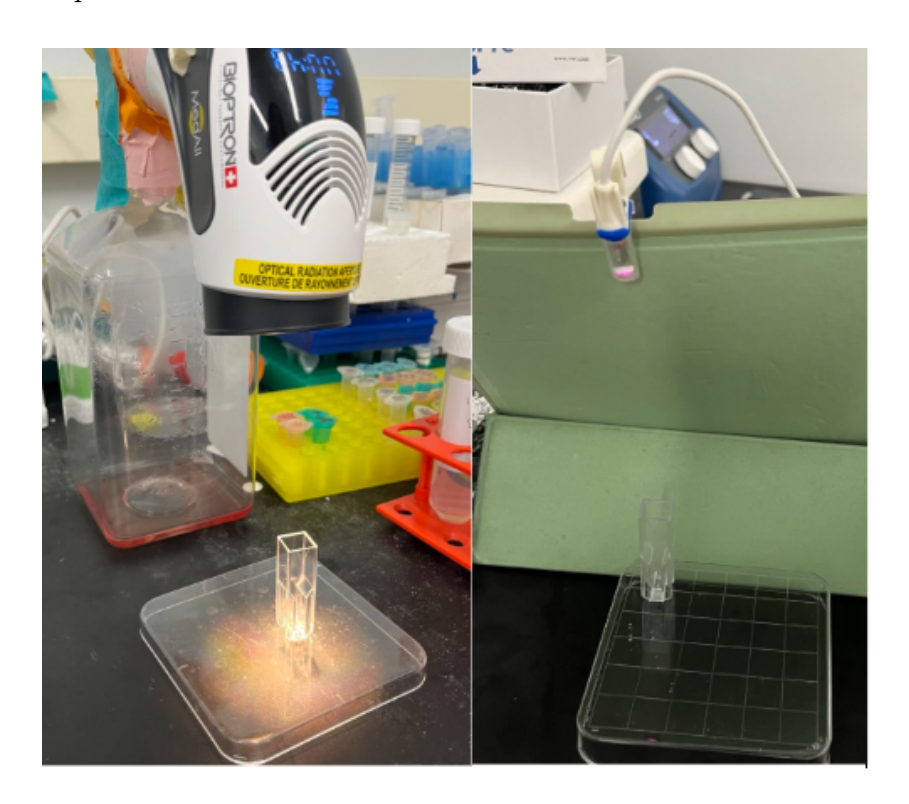


Figure 3.1: Irradiation with EMFs for DLS: Bioptron (left) and Vielight (right)

### 3.2.2 Zeta potential

MES80 10x buffer contained 800 MES, 2 mM MgCl², 0.5 mM EGTA was diluted with de –ionized water into MES80 3X (240 mM MES, 2 mM MgCl²,² 0.5 mM EGTA, pH 6) ,MES80 (80 mM MES, 2 mM MgCl², 0.5 mM EGTA, pH 6) and MES50 (50 mM MES, 2 mM MgCl², 0.5 mM EGTA, pH 6) to test how the tubulin and G-Actin react at different ionic strength. 6 μL of tubulin was added to 2394 μL of MES at each concentration to reach a final concentration of tubulin of 113.6 nM in the solution. While for G-Actin 28.8 μL (0.4 mg/mL) was added to 2371.2 μL of MES at every concentration to reach a final concentration of actin of 113.6 nM. This amount of volume was enough to cover 4-time steps (0 – 3 – 6 – 24 h). For each time point 600 μL of solution were used. In addition, for every concentration

of MES, 3 different samples were made to test a control, one stimulated with Bioptron (Bioptron MedAll) and one with Vielight (Vielight NeuroPro1 with Nasal applicator). The irradiations were done at 4  $^{\circ}$ C: Bioptron for 18:45 minutes and Vielight for 30 minutes. Between the different time points, the samples were sealed with aluminum foils and stored at 4  $^{\circ}$ C in the dark.

The analysis were done using NanoZS (Malvern Instruments) at the Lewis's Laboratory (Edmonton, University of Alberta).

## 3.3 Turbidity

Turbidity measurements were performed using  $100~\mu L$  of protein for every reading. Tubulin aliquots were collected from -80°C and diluted to 2.5~mg/mL with BRB80 to reach the volume established. The irradiations were conducted at 4 °C with Bioptron (Bioptron MedAll) and Vielight (Vielight NeuroPro2 with Nasal applicator) at three-time exposure: 10~minutes, 20~minutes and 30~minutes for each device. Both devices were set at  $40~mV/cm^2$ . The samples were pipetted into a 96~minutes and analyzed at the SpectraMax iD5 microplate reader in 340~m absorbance kinetic mode for 60~minutes at the Lewis's Laboratory (Edmonton, University of Alberta).

After the reading, the samples were collected and gradually cooled down to 4  $^{\circ}$ C and left there for 2 hours. Tubulin samples were re-collected and 1  $\mu$ L of GTP was added to the samples and another reading was performed to test if the irradiation could have caused damage to the microtubule assembly. The second readings were performed as the previous one.



Figure 3.2: SpectraMax iD5 microplate reader

Table 3.1: Microplate reader parameters

Parameters	Setting
Measurement mode Absorbance wavelength Temperature Shanking Designation of blank	Kinetic, 81 cycles of 1 reading per 30 seconds 340 nm 37°C 5s medium, orbital Blanks are not assigned. The first value is automatically set to zero.

## 3.4 Raman Spectroscopy

The samples for Raman Spectroscopy were collected from -80°C and diluted with BRB80 into a final concentration of 2.5 mg/mL for tubulin and diluited with 90  $\mu$ L of G-buffer into a final concentration of 0.4 mg/mL for G-Actin. For each protein 5  $\mu$ L were collected and analyzed at the Raman Spectroscopy. The solutions were irradiated with Bioptron (Bioptron MedAll) for 20 minutes and then analyzed using Renishaw inViaRaman Microscope at NanoFAB's Laboratory (Edmonton, university of Alberta). Raman spectra were acquired with 532 nm laser, 1200 lines per mm grating, 100 % power, exposition time 1s. The 50L magnification was used to focus the samples and multiple acquisitions (50) were made for each point and multiple points of the same samples were analyzed.



Figure 3.3: Renishaw inViaRaman microscope

## 3.5 Conductivity

#### **PVA** solution

PVA solution was made of 15 g of PVA powder in 100 mL of Milli-Q water. The solution was heated up to 90 °C and left at that temperature for about an hour, until it became gel-like and transparent. Then, it was left to cool down at room temperature. The solution was poured into a glass bottle and stored in the fridge at 4 °C.



Figure 3.4: PVA solution in gel-like phase

#### Tubulin samples

Tubulin samples were collected from -80 °C and diluted in BRB80 and BRB8 to test how the buffer can change conductivity: the dilutions were made with tubulin (45.45  $\mu M)$  and different volume of BRB80 or BRB8. For BRB80 four final different concentrations in the solution with PVA were tested: 2.27  $\mu M$ , 1.135  $\mu M$ , 0.7  $\mu M$  and 0.22  $\mu M$ . While, for BRB8 three final different concentrations in the solution with PVA were tested: 1.135  $\mu M$ , 0.7  $\mu M$  and 0.22  $\mu M$ . The irradiations were done at 4 °C for 20 minutes with Bioptron (Bioptron MedAll) and Vielight (Vieligh NeuroPro2 with Nasal applicator). Both devices were set at 40 mV/cm².

#### G-Actin samples

G-Actin samples were collected form -80 °C and diluted in G-Buffer to test how the buffer can change conductivity. G-Actin was tested at two final different concentrations in the solution with PVA: 4.65  $\mu$ M (no dilution of the protein) and 0.465  $\mu$ M. The irradiations were done at 4 °C for 20 minutes with Bioptron (Bioptron MedAll) and Vielight (Vieligh NeuroPro2with Nasal applicator). Both devices were set at 40 mV/cm².

#### **PVA** films

Once PVA solution reached room temperature, 95  $\mu$ L of this solution was collected and added to 5  $\mu$ L of protein solution (stimulated or non stimulated) to reach the established final concentrations of protein in the solution with PVA. This solution was poured on FTO substrate and stored at 70 °C oven overnight to create a solid film. Alpha-Step IQ surface profilometer was used to determine the films thickness at NanoFAB's Laboratory (Edmonton, university of Alberta). Then films were analyzed with the Four-Point-Probe (Lucus Pro4 4000 with Keithley2601 as source meter) at NanoFAB's Laboratory (Edmonton, university of Alberta) and the probe tips aligned to make proper contact with the dried tubulin. Probe spacing (1.016 mm). DC current was applied to the two outer probes (1  $\mu$ A) and the voltage (V) was measured between the two inner probes using a high sensitivity voltmeter. The experiments were conducted at 25 °C to study how conductivity changes.

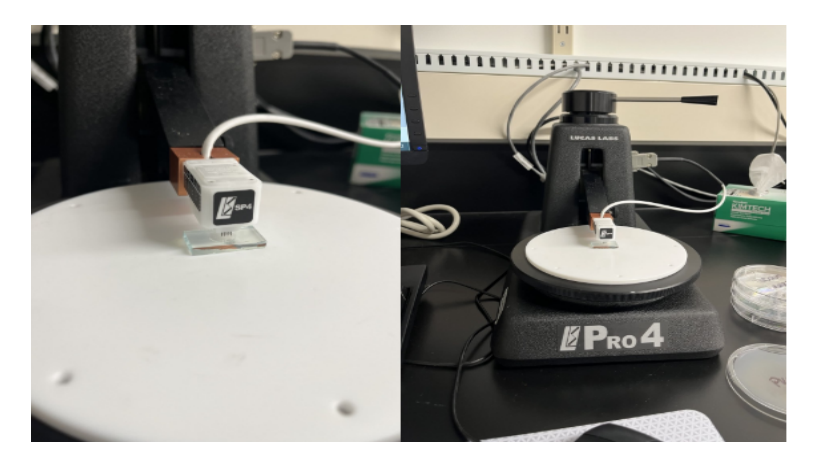
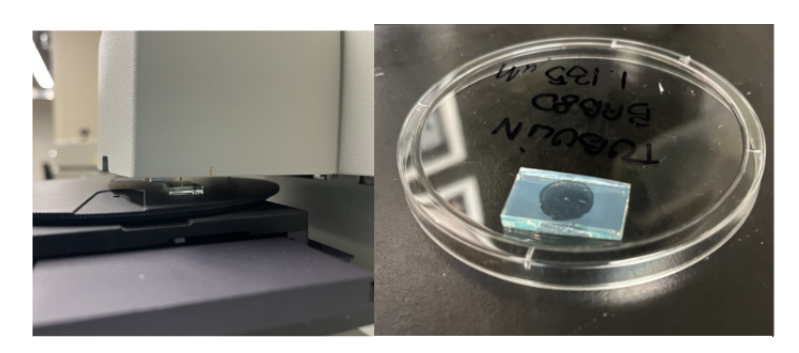


Figure 3.5: Four-Point Probe Lucus Pro4 4000



**Figure 3.6:** Alpha-Step IQ surface profilometer (left) and films on FTO substrate (right)

## 3.6 Data analysis

#### Hydrodinamic diameter

Data acquisition was performed by three runs for each sample and each run required five measurements of particle size to ensure statistical significance. To reconstruct the data, a Gaussian curve was used:

$$y(x) = y_0 + \frac{A \cdot e^{\frac{-4 \cdot \ln(2) \cdot (x - x_c)^2}{w^2}}}{w \cdot \sqrt{\frac{\pi}{4 \cdot \ln(2)}}}$$
(3.1)

 $y_0$  is the baseline length, w is the FWHM (Full Width at Half Maximum height) and A represents the area under the Gaussian curve, respectively, while  $x_c$  represents the position of the peak on the x-axis. For each value a Standard Error (SE) was calculated.

#### Zeta potential

Data acquisition was performed by three runs for each sample and each run required three measurements of z-potential to ensure statistical significance. For each sample, the standard deviation was calculated and an ANOVA test was performed on all samples to ensure scientific validity.

#### **Turbidity**

Data acquisition was performed in three runs for each sample to ensure statistical significance. The data collected were analyzed using the software OriginLab. To remove outliers, the curves were filtered with an FTT filter with five points of window and a cutoff frequency of 0.0033 Hz. The data were fitted with Boltzmann sigmoidal curve to obtain their slope and plateau values.

#### Raman Spectroscopy

The data were processed through OriginLab software OriginLab. After the acquisition, range reduction and baseline corrections were implemented. An asymmetric least-squares smoothing factor of 5 and 10 iterations was used for baseline correction. The data were smoothed using Savitzky-Golay with 20 points of window and normalized between 0 and 1.

#### Conductivity

Data acquisition was performed in three runs for each sample to ensure statistical significance (profilometer and 4PP). The Resistance, Resistivity and Resistance Sheet were given by a Four-Point Probe. The conductivity was measured by the following equation:

$$\sigma = \frac{1}{R_s \cdot t} \tag{3.2}$$

Where t is the thickness of the film.

## Chapter 4

## Results

For clearer interpretation of the graphs presented in this thesis, all plots labeled as 'Control' refer to results obtained with the unstimulated protein, whereas those labeled 'Bioptron' or 'Vielight' indicate that the protein was stimulated with the corresponding device prior to analysis.

#### 4.1 DLS

In this section of the thesis, the results obtained by using DLS will be presented. First, the results of the hydrodynamic diameter analysis of the proteins will be reported, followed by those related to the zeta potential, making a comparison between proteins exposed to EMFs and the control protein.

### 4.1.1 Hydrodinamic Diameter

The first experiment performed with the Malvern Zetasizer was the analysis of the hydrodynamic diameter of proteins, using the same buffer but varying the concentration of DMSO. It is well established that the concentration of DMSO affects the size of the protein: in fact, studies have shown that increasing concentrations of DMSO in solution lead to a linear increase in the hydrodynamic diameter of tubulin. [66] The DMSO concentrations used in the current experiments were carefully maintained below certain thresholds, as exceeding these limits would have led to protein aggregation, thereby impeding the accurate determination of the protein's diameter. To further prevent aggregation, colchicine (for tubulin) and latrunculin (for G-actin) were added to the solutions, as these inhibitors block polymerization and stabilize proteins in their monomeric forms.

The results are presented by 'size by number'; if a comparison with 'size by volume' or 'size by intensity' is required, the corresponding graphs and values are

available in the Appendix.

To perform a comparative analysis at different time points, we first examined the behavior of the unstimulated protein at different DMSO concentrations. As shown in Figure 6.10, at time 0 the trend observed for tubulin is consistent with the findings of [66]: the hydrodynamic diameter increases with increasing DMSO concentration. Comparing the plots at 3, 6, and 24 hours after preparation of the solution, no major changes in size are detected, indicating that the protein remains stable without significant alterations in hydrodynamic diameter. Only at 24 hours do the values at 10%, 15% and 20% DMSO appear to converge toward similar diameters. However, it should be noted that after 24 hours protein stability cannot be fully guaranteed and measurements may be affected.

The graphs presented show 'size by number' distributions obtained with the Malvern Zetasizer. For a clearer understanding of the results, the corresponding hydrodynamic diameter values for the control are reported in Table 4.1.

Next, it was analyzed how stimulation with the Bioptron device affected the protein (Figure 6.11. Compared with the control, the changes are already detectable at time 0, the most evident being at concentration of 15% DMSO, where a marked decrease in the average hydrodynamic diameter of tubulin is observed. At the other concentrations, the behavior remains similar to that of the control across the different time points. At 3 and 6 hours, additional peaks appear at lower diameters, suggesting that stimulation may have induced partial dissociation of the tubulin dimer, generating a reduced size population. At 10% DMSO and 24 hours, no distinct peak could be detected, as the hydrodynamic diameter values for all tubulin samples were around 2000 nm. The peak values obtained under Bioptron stimulation are reported in Table 4.2. With Vielight stimulation, at time 0 the 0-5% and 10-15% DMSO concentrations appear to cluster in pairs, showing similar trends. These similarities are lost over time and the behavior of each concentration gradually resembling that of the control. As observed with Bioptron, additional populations merge at lower hydrodynamic diameters, suggesting that radiation may have disrupted the bond between the  $\alpha$ - and  $\beta$ -tubulin subunits. This effect is most evident 3 and 6 hours after stimulation.

G-actin was analyzed at only three concentrations of DMSO, as it tends to aggregate more easily. Even in the control at time 0 and 5% concentration, a peak is observed around 6 nm together with additional populations. Similarly to tubulin, G-actin remains stable over time, showing no major changes at the different time points, as reported in Table 4.4. In contrast to tubulin, its globular shape results in a smaller hydrodynamic diameter, approximately 4 nm at a concentration of 0%. Significant differences are observed with Bioptron stimulation at time 0, where all concentrations display populations with larger diameters, which then disappear at later time points (Figure 4.5). Vielight shows a similar trend to Bioptron at a concentration of 5% but does not appear to induce an increase in diameter at lower

#### concentrations Figure 4.6.

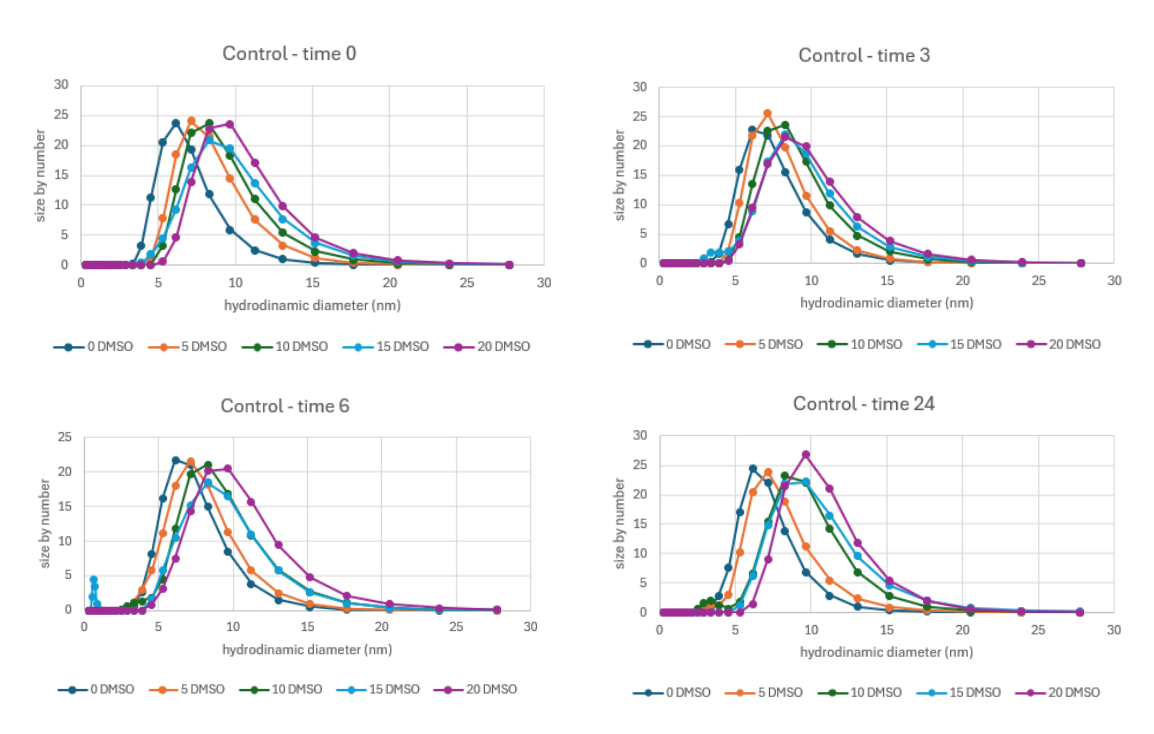


Figure 4.1: Tubulin control at time points 0, 3, 6, and 24.

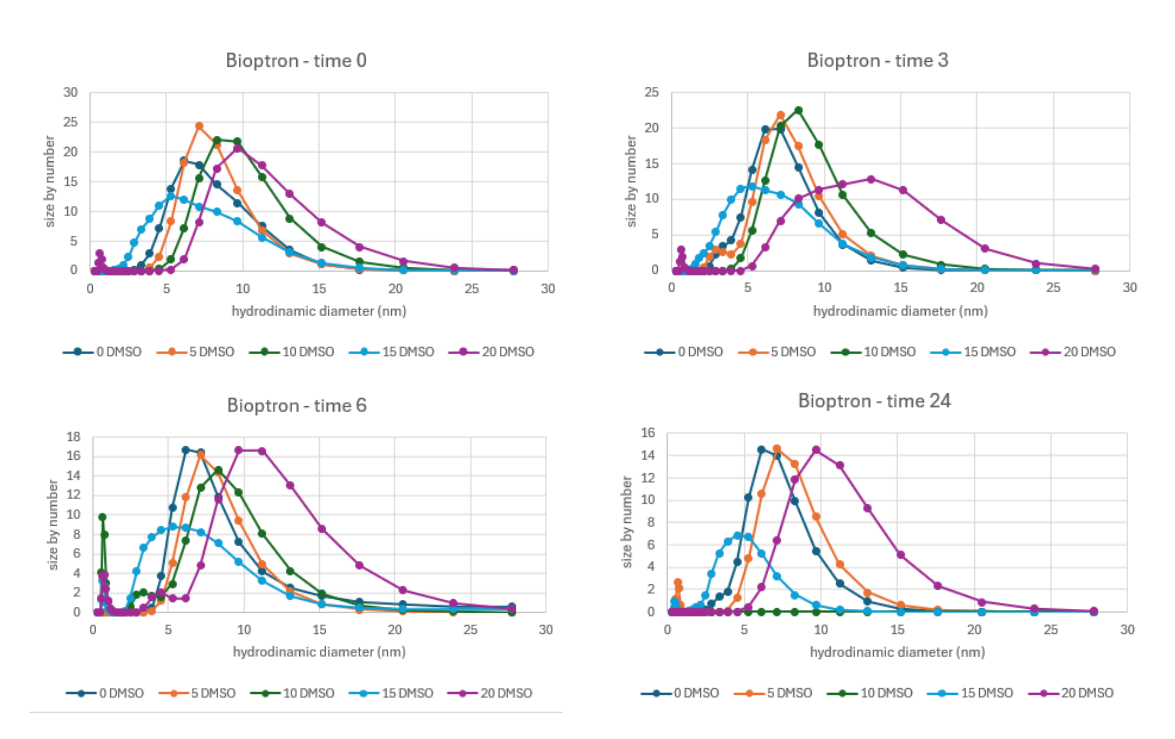


Figure 4.2: Tubulin Bioptron at time points 0, 3, 6, and 24.

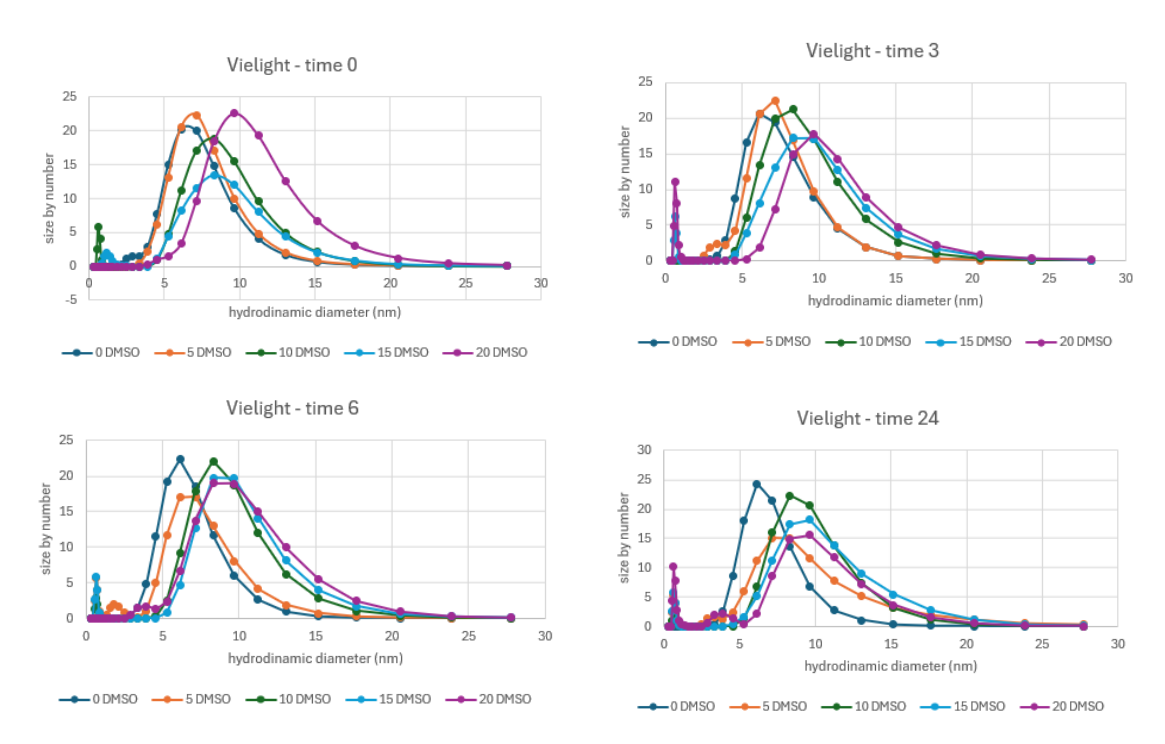


Figure 4.3: Tubulin Vielight at time points 0, 3, 6, and 24.

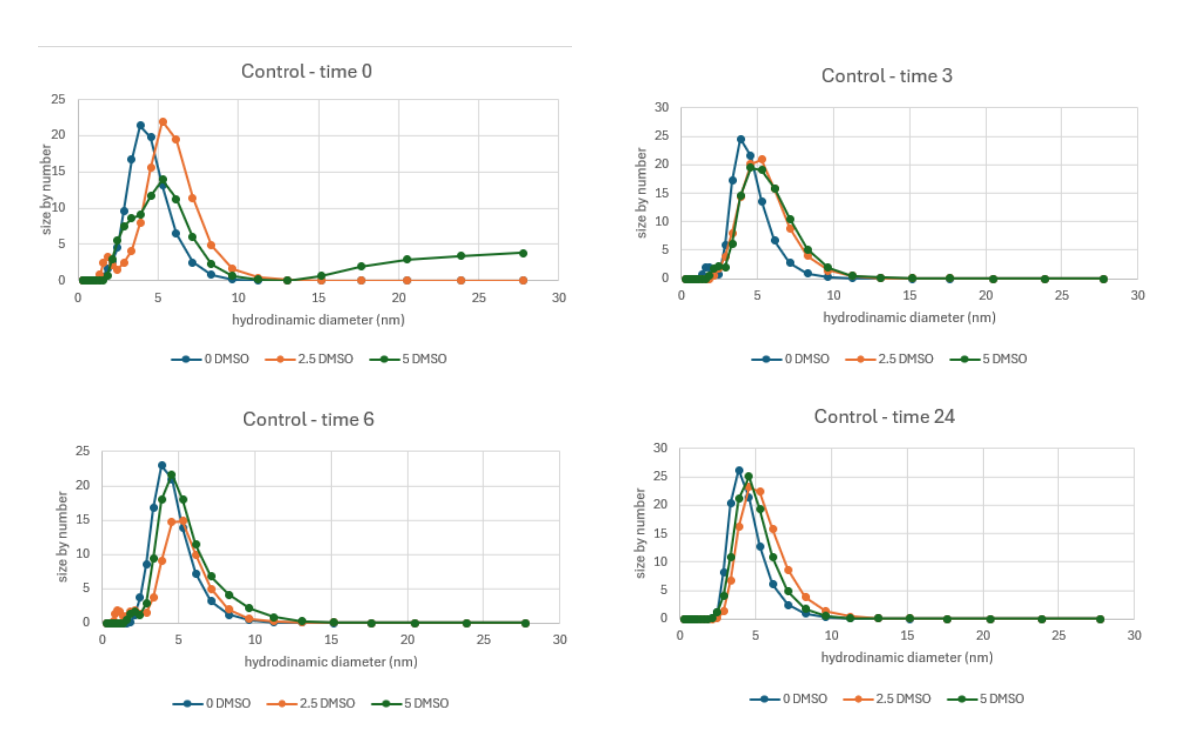


Figure 4.4: G-actin Control at time points 0, 3, 6, and 24.

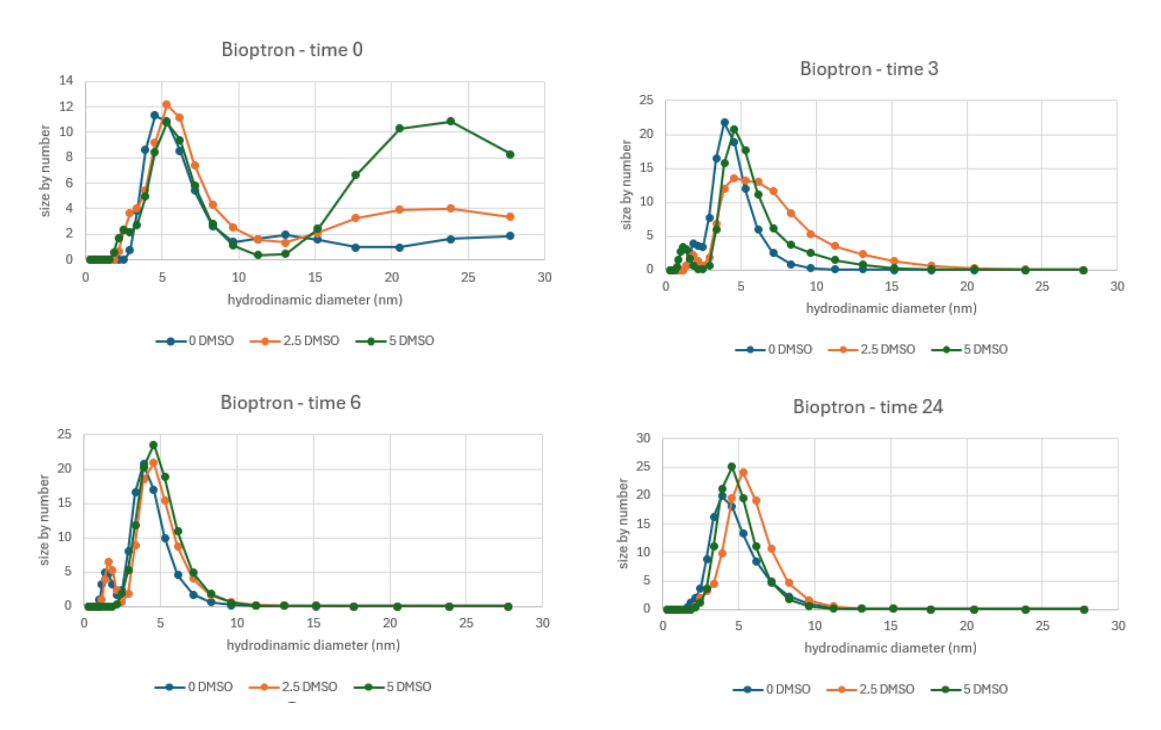


Figure 4.5: G-actin Bioptron at time points 0, 3, 6, and 24.

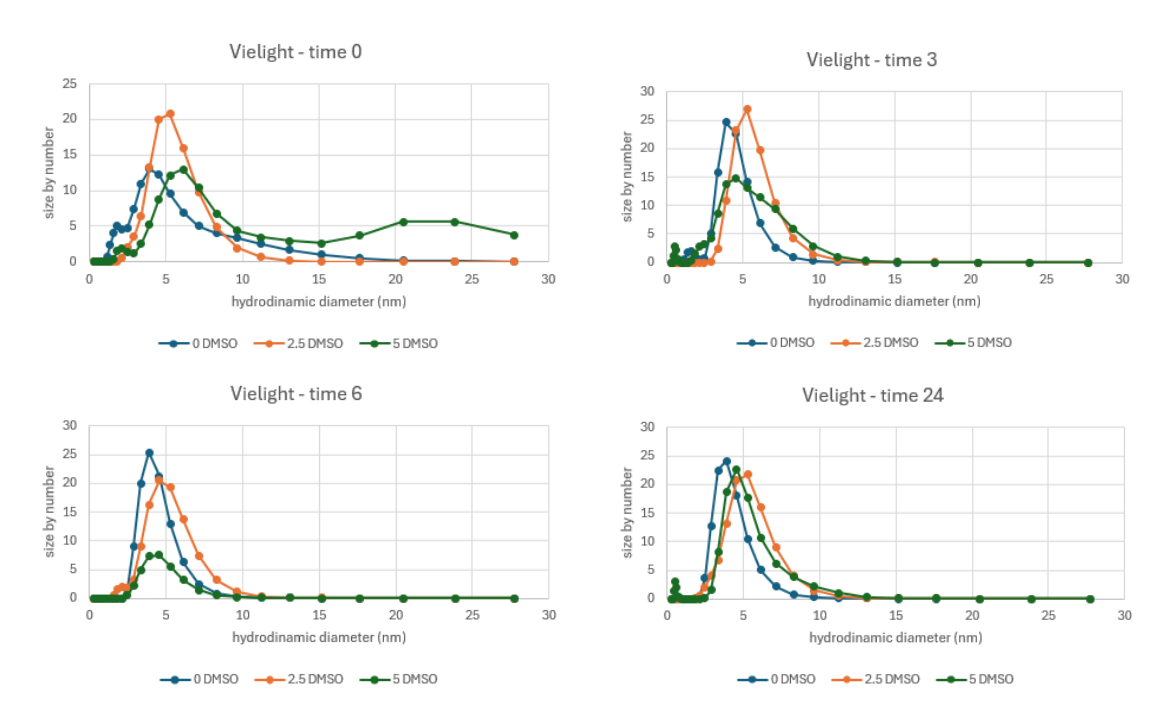


Figure 4.6: G-actin Vielight at time points 0, 3, 6, and 24.

Table 4.1: Control on Tubulin

% DMSO (V/V)		Xc by number						
	Time 0	SE	Time 3	SE	Time 6	SE	Time 24	SE
0	6.095	0.0162	6.463	0.0576	6.291	0.1028	6.379	0.00652
5	7.285	0.0900	6.516	0.1276	6.715	0.0512	6.811	0.0196
10	8.0172	0.0608	7.716	0.0134	7.740	0.0860	7.620	0.0054
15	7.833	0.2140	7.389	0.1296	7.989	0.1770	7.981	0.1912
20	9.051	0.0960	8.403	0.0984	7.524	0.1872	9.384	0.0440

Table 4.2: Bioptron on Tubulin

% DMSO (V/V)		Xc by number						
	$\overline{\text{Time 0}}$	SE	Time 3	SE	Time 6	SE	Time 24	SE
0	6.786	0.065	6.100	0.039	7.940	0.298	6.139	0.036
5	7.180	0.020	6.425	0.024	7.287	0.019	6.371	0.158
10	8.753	0.112	7.772	0.146	8.753	0.112	2082	340
15	6.573	0.763	6.969	0.188	7.444	0.264	5.300	0.148
20	9.483	0.177	10.726	0.448	8.997	0.173	9.458	0.166

Table 4.3: Vielight on Tubulin

% DMSO (V/V)				Xc by	number			
	Time 0	SE	Time 3	SE	Time 6	SE	Time 24	SE
0	6.247	0.0180	6.291	0.0374	5.853	0.0464	6.184	0.0398
5	6.606	0.0568	6.457	0.0476	5.514	0.0696	6.756	0.0830
10	6.952	0.2460	7.767	0.0622	7.674	0.1210	7.931	0.0922
15	8.1178	0.4860	7.482	0.2720	7.758	0.1940	8.163	0.1412
20	9.050	0.0976	9.249	0.0984	7.524	0.1872	9.384	0.0440

Table 4.4: Control on G-actin

% DMSO (V/V)				Xc by	number			
	Time 0	SE	Time 3	SE	Time 6	SE	Time 24	SE
0	4.227	0.0608	4.385	0.0326	4.536	0.0198	4.193	0.0500
2.5	4.834	0.846	4.782	0.0922	4.541	0.0304	4.807	0.0524
5	5,727	0.040	5.21	0.10	5.021	0.035	5.046	0.032

 Table 4.5:
 Bioptron on G-actin

% DMSO (V/V)				Xc by	number			
	Time 0	$\mathbf{SE}$	Time 3	$\mathbf{SE}$	Time 6	$\mathbf{SE}$	Time 24	SE
0	4.978	0.516	4.219	0.0552	4.004	0.0778	4.653	0.0604
2.5	4.922	0.002	5.225	0.325	4.205	0.694	4.900	0.00916
5	6.916	0.234	4.824	0.0368	4.843	0.022	4.969	0.053

Table 4.6: Vielight on G-actin

% DMSO (V/V)				Xc by	number			
	$\overline{\text{Time 0}}$	SE	Time 3	SE	Time 6	SE	Time 24	SE
0	5.072	0.233	4.605	0.0236	4.602	0.0190	4.255	0.0158
2.5	4.834	0.165	5.032	0.0098	4.534	0.0440	4.710	0.0426
5	6.034	0.072	5.126	0.108	4.707	0.822	5.22	0.97

#### 4.1.2 Zeta potential

Another analysis performed with the Malvern Zetasizer was the measurement of the zeta potential to investigate how it changes around the proteins depending on the buffer conditions. The same buffer was used at different concentrations, since modifying the buffer composition or ionic strength alters the interaction with the protein surface charge. In particular, G-actin and tubulin are both negatively charged proteins at physiological pH; therefore, attention was given to how positive counterions interact with the protein surface, forming the electrical double layer. The zeta potential reflects the electrostatic potential at the slipping plane within this double layer, rather than directly at the protein surface. MES was chosen as the solvent because it is zwitterionic and therefore does not directly interact with the surface charges of the proteins.

The effect of the same buffer at constant pH on the zeta potential of both proteins was compared. In MES80 (isoelectric point around 5 [67]), the control samples for tubulin and G-actin remained relatively stable (approximately -8/-9 mV for tubulin and -13/-14 mV for G-actin). The only notable difference was observed at 24 h, when tubulin became less negative, whereas G-actin remained stable. This result is consistent with the lower stability of tubulin compared to G-actin after 24 h at 4 °C. With Bioptron stimulation, tubulin showed a trend toward less negative values over time, while Vielight-treated samples exhibited a behavior comparable to the control.

Conversely, significant differences were observed in the MES80 3X measurements. Initially, the controls exhibited lower negative zeta potentials, approximately –3 mV for tubulin and –7 mV for G-actin, which can likely be attributed to the elevated buffer concentration and the subsequent increase in positive counterions interacting with the protein surface. Over time, both proteins achieved stabilization towards more negative zeta potential values. Notably, at time point zero, samples treated with Bioptron and Vielight showed more negative zeta potentials in comparison to the control samples, indicating that irradiation may have induced a rearrangement of surface charges.

In contrast, the MES50 condition revealed no significant differences either between the proteins or across the treatments, suggesting that this buffer concentration may be inadequate to detect measurable variations in zeta potential.

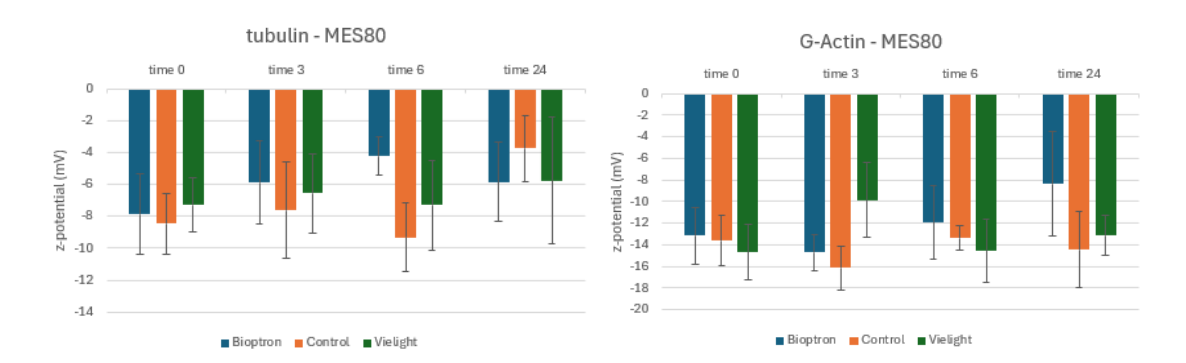


Figure 4.7: Zeta potential in MES80

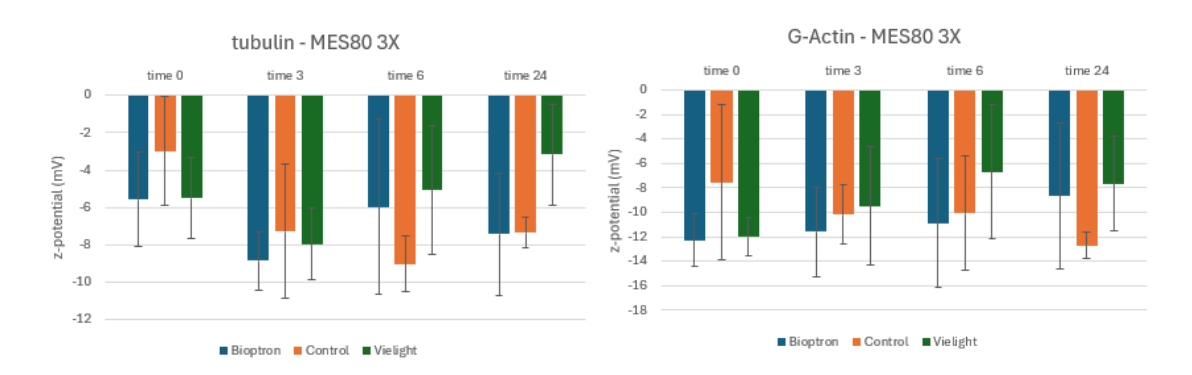


Figure 4.8: Zeta potential in MES80 3X

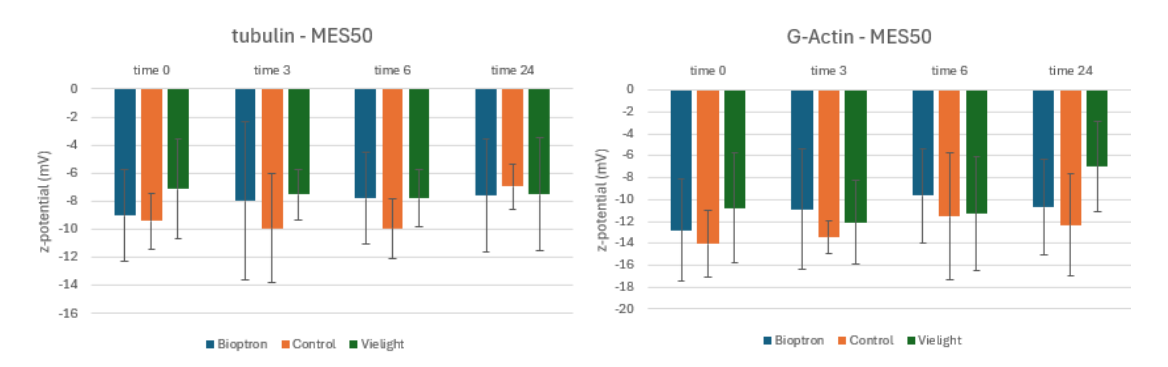


Figure 4.9: Zeta potential in MES50

## 4.2 Turbidity

The turbidity analysis of tubulin was used to evaluate its stability, solubility and polymerization capacity under experimental conditions. Light scattering at 340 nm was monitored as an indicator of microtubule assembly.

As illustrated in Figures 4.10–4.12, all stimulated samples demonstrated enhanced absorbance relative to the control during the initial polymerization assay, of the exposure duration. This increased light scattering, which is typically indicative of the formation of larger assemblies or aggregates. Under Bioptron and Vielight conditions, there was an acceleration in tubulin polymerization, with Bioptron generally exhibiting the most pronounced increase in Optical Density values ( $\mathrm{OD}_{340}$ ), particularly with shorter durations of stimulation. Following the cooling phase and the subsequent replenishment of GTP, which occurred three hours after stimulation, a different trend was observed:

- 10 min stimulation: Bioptron stimulated samples showed a marked decrease in turbidity (approximately 50% lower OD) and a slower polymerization rate, while Vielight produced the opposite behavior, with turbidity curves indicating depolymerization at 37 °C;
- 20 min stimulation: Bioptron increased the maximum turbidity compared to the control, while Vielight samples maintained values comparable to their initial measurement;
- 30 min stimulation: Bioptron mainly affected the kinetics, slowing down the polymerization process without substantially changing the turbidity, while Vielight stimulation enhanced OD and accelerated polymerization.

Collectively, these findings propose that electromagnetic stimulation modulates tubulin assembly in a manner dependent on both time and device type: Bioptron seems to predominantly affect polymerization kinetics, whereas Vielight influences both turbidity levels and stability, with contrasting effects at short versus extended stimulation durations.

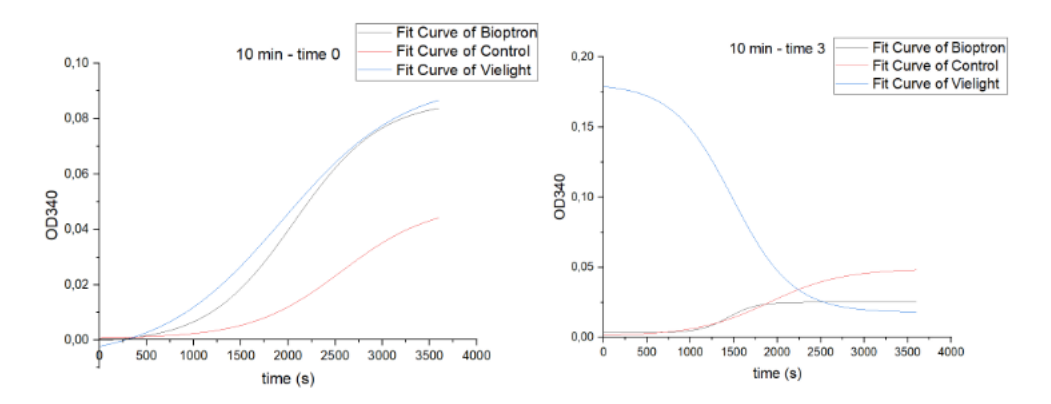


Figure 4.10: Turbidity - 10 min stimulation

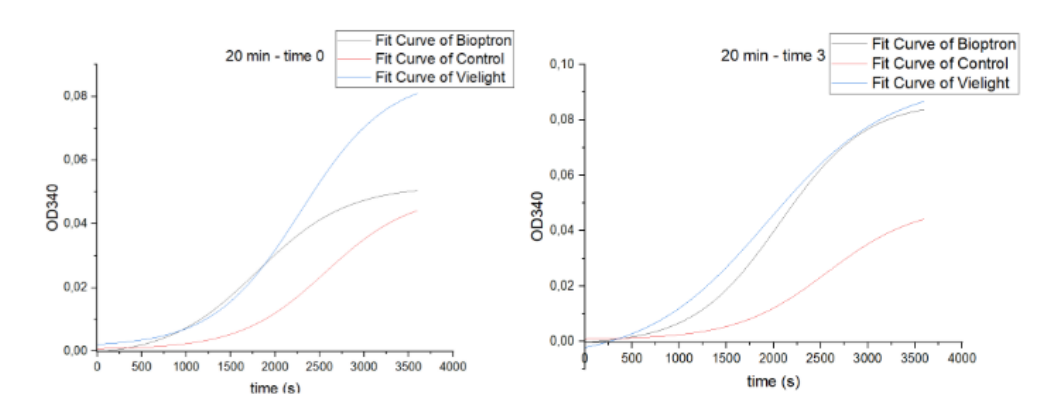


Figure 4.11: Turbidity - 20 min stimulation

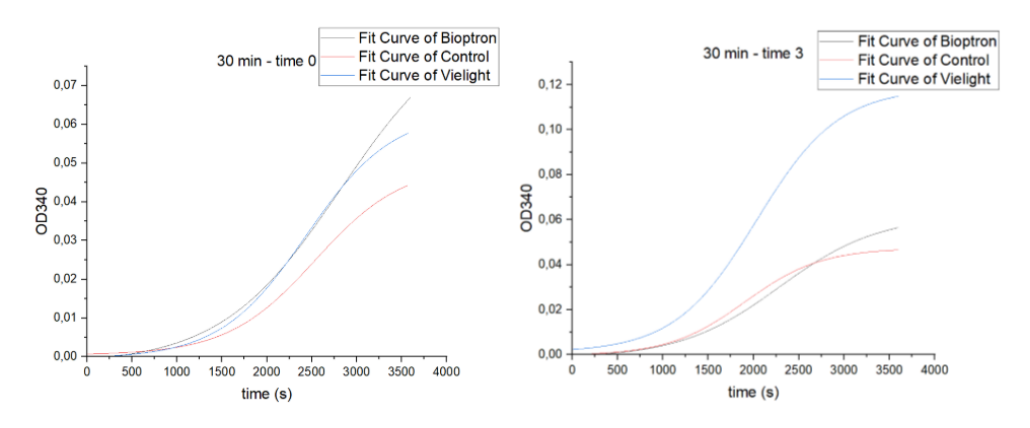


Figure 4.12: Turbidity - 30 min stimulation

## 4.3 Raman Spectroscopy

Raman spectroscopy was performed to probe the molecular vibrations of tubulin and G-actin and to discover potential structural changes induced by light stimulation. This technique is particularly suited for detecting modifications in the protein secondary structure, such as shifts in the amide I, II and III bands. Comparing stimulated and control samples allowed evaluation of whether irradiation affected the backbone conformation or side-chain environment.

In the 1500–1700 cm<sup>-1</sup> spectral window, Raman spectra of both tubulin and G-actin lacked the canonical Amide I and II bands typically observed at  $\sim 1650$  cm<sup>-1</sup> and  $\sim 1550$  cm<sup>-1</sup>. Tubulin displayed a single band centered at  $\sim 1595-1600$  cm<sup>-1</sup>, whereas G-actin showed only a broad, low-intensity signal with no distinct peaks. In both proteins, the Bioptron-stimulated and control spectra were nearly the same, indicating that irradiation did not induce detectable changes in the peptide backbone vibrations under the tested conditions.

An analysis of the spectral region between 1200 and 1400 cm<sup>-1</sup>, which includes the Amide III band as well as  $\rm CH_2/COO^-$  vibrations, produced comparable results. The findings revealed that tubulin exhibited two distinct peaks at  $\sim 1300$  and  $\sim 1380$  cm<sup>-1</sup>, with G-actin displaying Amide III characteristics. In both proteins, the Bioptron spectra demonstrated a marginal decrease in overall intensity without any significant shifts in peak positions, suggesting that illumination did not substantially alter the secondary structure. Nevertheless, the possibility of a slight decrease in scattering efficiency cannot be entirely ruled out.

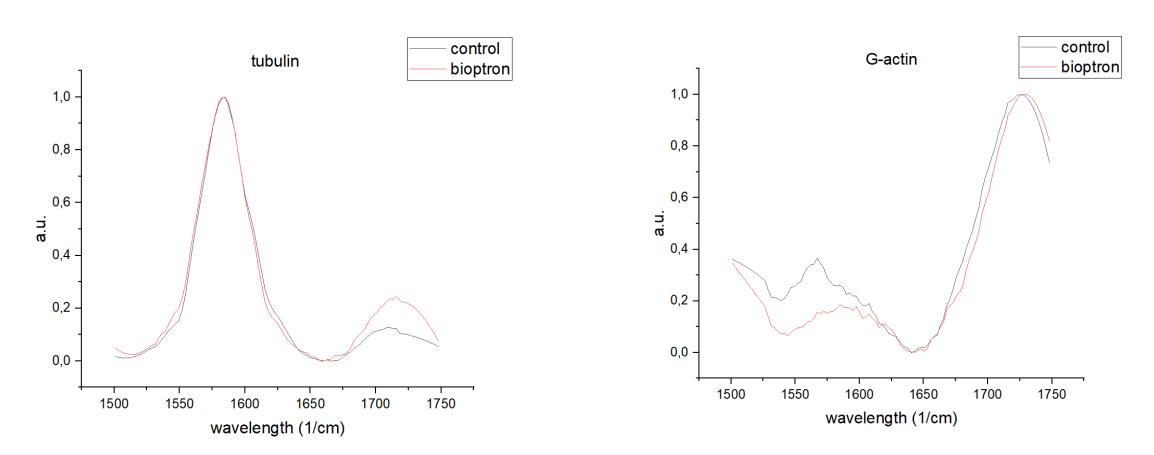
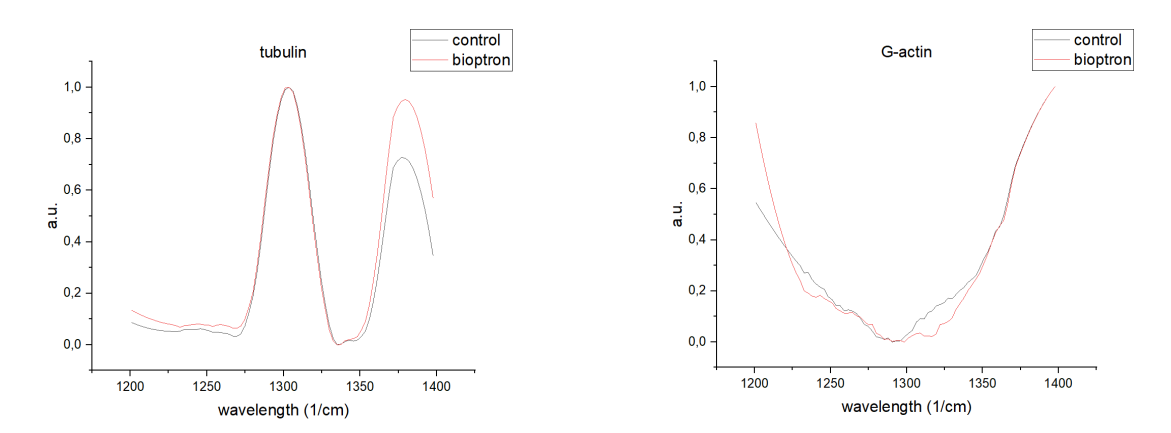


Figure 4.13: Raman spectra at  $1500-1750 \text{ cm}^{-1}$ 



**Figure 4.14:** Raman spectra at 1200-1400 cm<sup>-1</sup>

## 4.4 Conductivity

#### 4.4.1 Conductivity in reconstitution buffer

The analysis of Direct Current (DC) conductivity of proteins encapsulated in PolyVinyl Alcohol (PVA) provides valuable insights into their structural and functional behavior in some environments. Conductivity measurements allow the detection of charge transport mechanisms, ion mobility and protein-matrix interactions. Encapsulation of PVA mimics a biocompatible semi-solid environment that preserves protein integrity while allowing systematic electrical characterization.

To analyze the conductivity proteins, an initial assessment was performed on PVA films containing unstimulated protein, followed by comparisons with films incorporating stimulated protein. As shown in Figures 4.17 and 4.18, the control films containing unstimulated protein display a decreasing conductivity trend as the protein concentration decreases. For example, at low concentration (0.222  $\mu$ M) in the tubulin films, the conductivity value remains quite close to that of PVA with BRB80 (1.147  $\mu$ S/m). The same happens for G-actin, where at a concentration of 0.465  $\mu$ M the conductivity of the control is practically identical to that of the film containing G-buffer (1.763  $\mu$ S/m). These reference films were prepared to include the same proportion of all reconstitution components except the protein itself. They were specifically designed to allow subtraction of the background conductivity contributed by other conductive substances, such as BRB80 and G-buffer, and to isolate the contribution of protein alone when encapsulated in the PVA film. The values of conductivity are shown in Table 4.7 and 4.8.

On the other hand, the stimulated films show a completely different trend compared to the unstimulated ones. In tubulin films, Bioptron exhibits an opposite behavior to the control: the radiation appears to have a stronger effect at higher concentrations, resulting in a protein conductivity comparable to that of the film containing only BRB80. In contrast, Vielight drastically reduces the conductivity values, bringing them to nearly one-quarter of the control, with little to no dependence on protein concentration. Even more relevant are the results obtained with G-actin, where at the highest concentration (4.65  $\mu$ M) conductivity decreased from 54.58  $\mu$ S/m to 2.62  $\mu$ S/m with Bioptron and 2.54  $\mu$ S/m with Vielight, corresponding to nearly one order of magnitude difference. At lower G-actin concentrations, however, electromagnetic field stimulation appeared to have little effect.

The Vielight treatments produced consistent conductivity values regardless of the protein concentration, while the Bioptron treatment exhibited a distinct concentration-dependent effect.

Films with protein can be modeled as an electrical circuit in which tubulin or G-actin is embedded in a poorly conductive medium such as PVA. On this basis, it is possible to estimate the conductivity of the protein itself by considering the

PVA—buffer matrix as a resistive element arranged in series and parallel with the protein. In dry films, proteins are immobilized and cannot diffuse, as the absence of free water prevents molecular mobility, even under electrical stimulation. Charge transport occurs primarily through the salts of the reconstitution buffer and via the protein molecules.

By taking into account parameters such as the diameter of the Four-Point Probe tips (80  $\mu$ m), the spacing between them (1.106 mm) and the film thickness (different for each film, around 50  $\mu$ m), the behavior of charge transport within the film can be modeled. It is assumed that the current flows from one probe tip and is collected by the adjacent one, such that the active volume for conduction can be approximated as a parallelepiped. Within this volume, PVA acts as a highly resistive component, while the buffer contributes as an additional resistance in series. The protein can then be represented as another resistive element, either in series or in parallel with the matrix. Given the film thickness, this elementary circuit is effectively repeated both in series and in parallel throughout the structure.

The conductivity of the pure protein can be obtained by employing a series of equations to evaluate its measurement across different concentrations.

To begin, the average separation a is defined as:

$$a = \frac{N}{V} = \frac{C \cdot N_A}{V},\tag{4.1}$$

where C is the molar concentration,  $N_A$  is Avogadro's number and V is the volume  $(1 \text{ mm}^3)$ .

From this value, it can be derived the characteristic length l of each block as:

$$l = \frac{1}{\sqrt[3]{a}},\tag{4.2}$$

which represents the effective length of the circuit  $R_{eff}$ .

The effective resistance of the circuit is then given by:

$$R_{\text{eff}} = R_{pb} + R_p, \tag{4.3}$$

where  $R_{pb}$  denotes the resistance arising from the contribution of the buffer and PVA and  $R_p$  denotes the resistance due only to the protein.

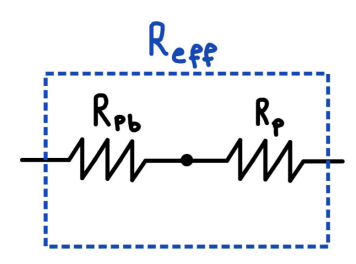


Figure 4.15: Effective Resistance circuit of Tubulin

If l is considered as the total length of the block including PVA + buffer and protein,  $\Delta l$  can be defined as the length corresponding to the protein and  $l - \Delta l$  as the length corresponding to  $R_{pb}$ . By rewriting the equation, we obtain:

$$R_{pb} = \frac{1}{\sigma_{pb}} \cdot \frac{(l - \Delta l)}{A}, \qquad R_p = \frac{1}{\sigma_p} \cdot \frac{\Delta l}{A},$$
 (4.4)

where  $\sigma_{pb}$  is the conductivity of the PVA–buffer film,  $\sigma_p$  is the conductivity of the protein and A is the cross-sectional area.

Experimentally, the resistance of the whole film can be written as:

$$R_{\text{eff}} = \frac{1}{\sigma_{\text{exp}}} \cdot \frac{l}{A},\tag{4.5}$$

where  $\sigma_{\text{exp}}$  is the measured conductivity of the composite film.

By combining the equations Eq. 4.3 and 4.4 and defining the fraction  $f = \frac{\Delta l}{l}$ , the conductivity of the single circuit can be expressed as:

$$\sigma_{\text{exp0}} = \frac{\sigma_{pb} \cdot \sigma_p}{\sigma_p (1 - f) + \sigma_{pb} f}.$$
 (4.6)

At this stage, the following quantities can be calculated:

• The number of blocks in series:

$$n_s = \frac{L}{l},\tag{4.7}$$

where L is the distance between the two probe tips  $(L = 1.016 \,\mathrm{mm})$ .

• The number of blocks in parallel:

$$n_p = \frac{W \cdot T}{l^2},\tag{4.8}$$

where W is the film thickness and T is the probe diameter  $(T = 80 \,\mu\text{m})$ .

Combining these equations, the experimental conductivity of the composite film can be written as:

$$\sigma_{\text{exp}} = \frac{n_p}{n_s} \cdot \sigma_{\text{exp0}} = \frac{n_p}{n_s} \cdot \frac{\sigma_{pb} \cdot \sigma_p}{\sigma_p (1 - f) + \sigma_{pb} f}, \tag{4.9}$$

where  $\sigma_{pb}$  is the conductivity of the PVA-buffer matrix,  $\sigma_p$  is the intrinsic conductivity of protein, and  $f = \Delta l/l$  as defined earlier.

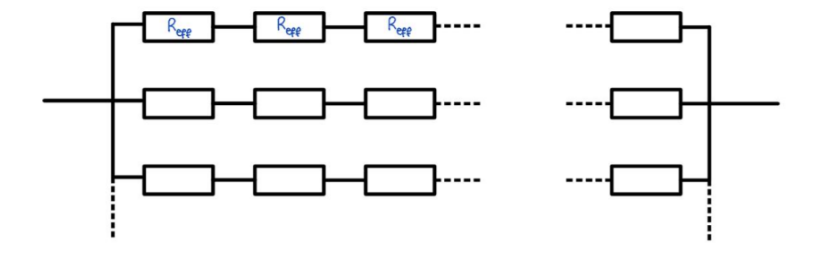


Figure 4.16: Hypothetic circuit

By substituting all known parameters and rearranging the expression, the conductivity of pure tubulin can be obtained as:

$$\sigma_p = \frac{\theta \cdot \sigma_{pb} \cdot f}{1 - \theta(1 - f)},\tag{4.10}$$

where  $\theta$  is an auxiliary variable introduced to simplify the algebric steps of the calculation as:

$$\theta = \frac{n_s \, \sigma_{\text{exp}}}{\sigma_{pb} \, n_p}.\tag{4.11}$$

Therefore, it was possible to calculate the conductivity values of the solely protein using the previous equation. At high concentrations, this conductivity is approximately 73.42 nS/m for tubulin and 723.7 nS/m for G-actin.

As shown in Figure 4.19(left), Bioptron significantly reduced the conductivity of tubulin in BRB80 (3.639 nS/m), and Vielight also induced a reduction (6.947 nS/m), compared to the control, which appears to be nearly ten times higher. A similar behavior is observed in G-actin, where conductivity decreases by two orders of magnitude compared to the control. Specifically, Bioptron reduces conductivity to 6.384 nS/m, while Vielight reduces it to 6.351 nS/m.

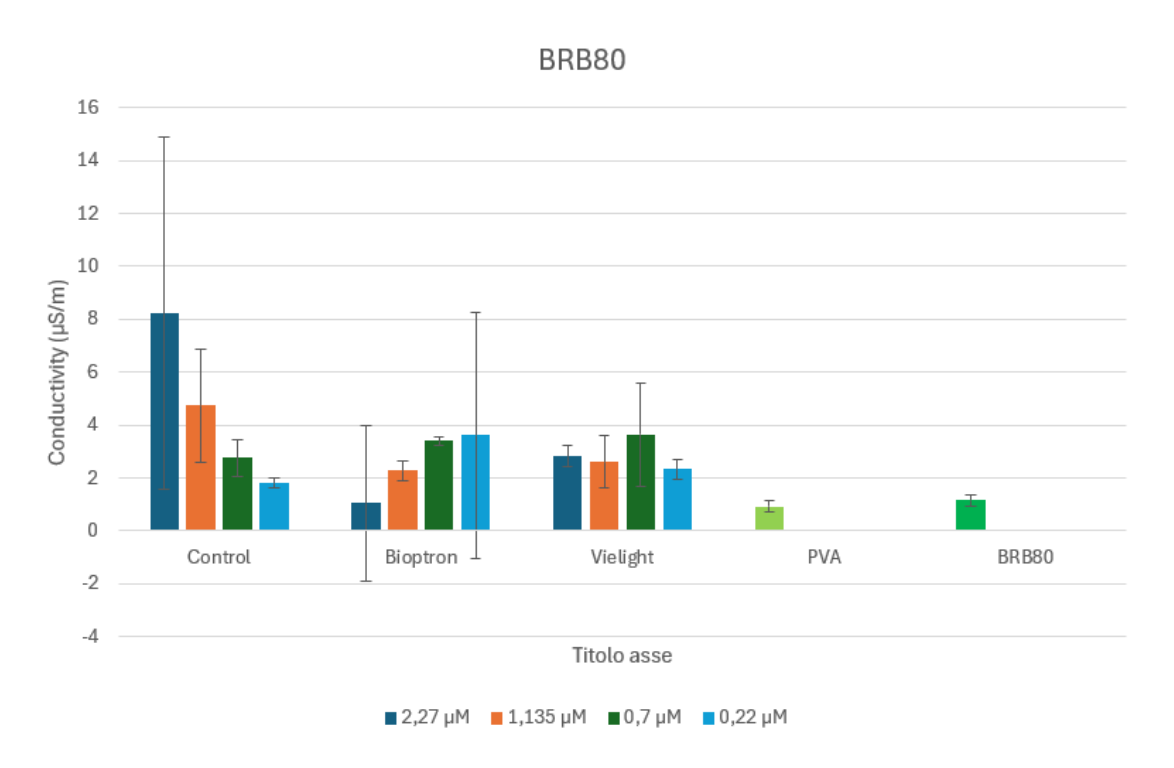


Figure 4.17: Conductivity of tubulin in BRB80

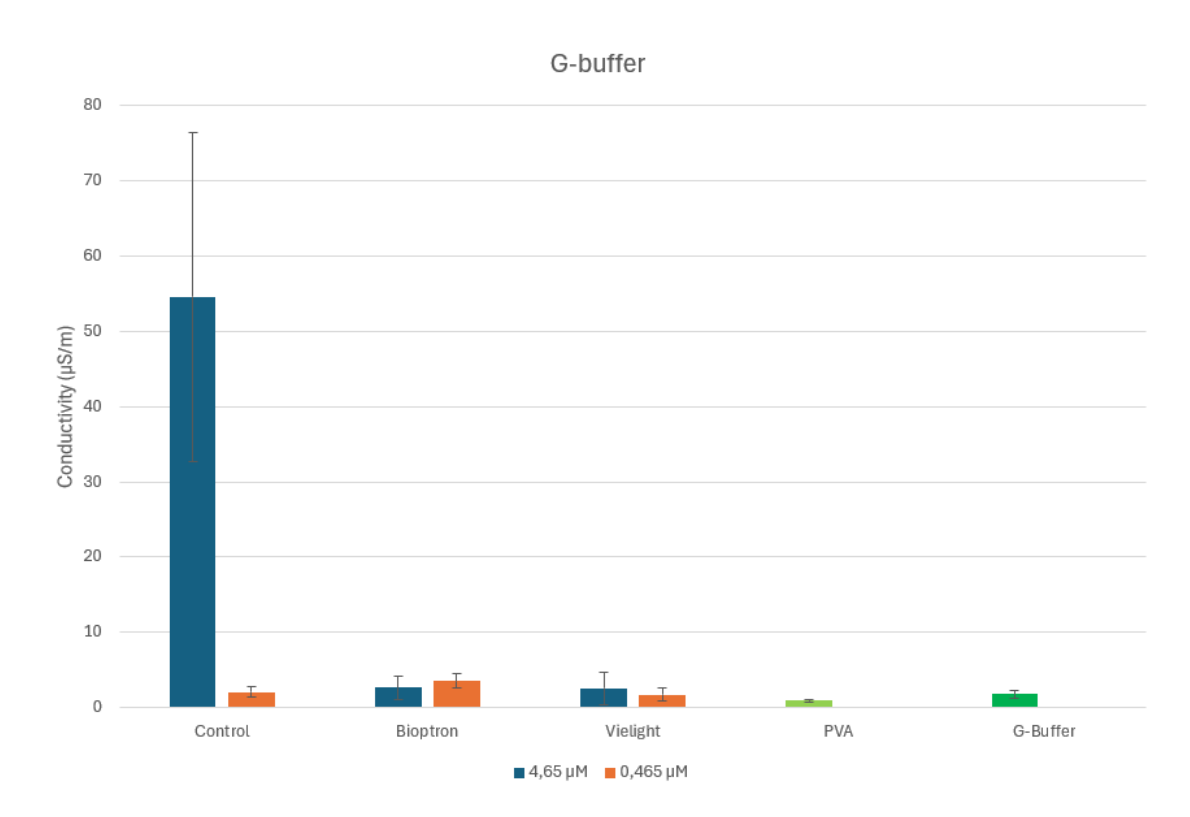


Figure 4.18: Conductivity of actin in G-Buffer

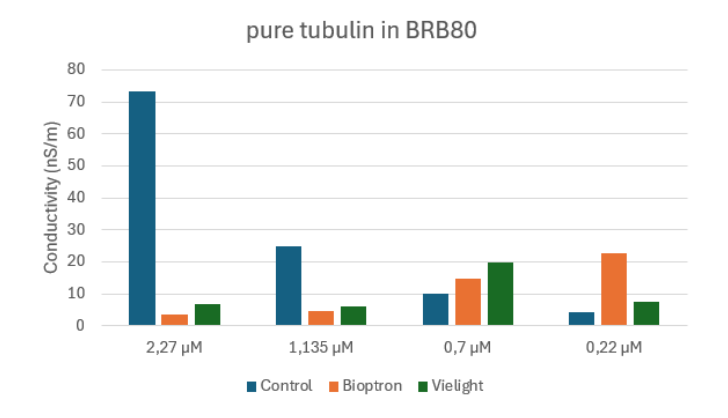


Figure 4.19: Conductivity of pure tubulin in BRB80

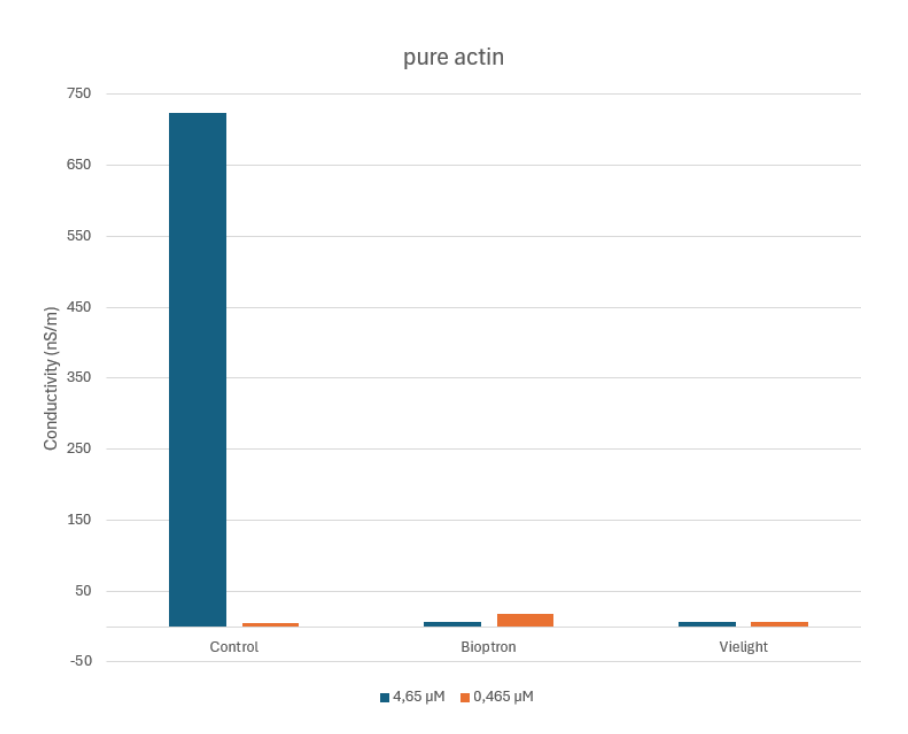


Figure 4.20: Conductivity of G-actin

Table 4.7: Conductivity of tubulin in BRB80 ( $\mu S/m$ )

Concentration	Control	Bioptron	Vielight
$2.27~\mu\mathrm{M}$	8.223	1.041	2.821
$1.135~\mu\mathrm{M}$	4.74398	2.27521	2.61178
$0.7~\mu\mathrm{M}$	2.77367	3.40512	3.64674
$0.222~\mu\mathrm{M}$	1.80899	3.61966	2.33266

Table 4.8: Conductivity of G-actin in G-buffer ( $\mu S/m$ )

$4.65 \mu M$ $54.587$ $0.465 \mu M$ $2.068$	2.627 $3.562$	2.540 1.712	0.9214	1.763

**Table 4.9:** Conductivity of pure tubulin in BRB80 (nS/m)

Concentration	Control	Bioptron	Vielight
$2.27~\mu\mathrm{M}$	73.42	3.639	6.947
$1.135~\mu\mathrm{M}$	24.97	4.562	6.102
$0.7~\mu\mathrm{M}$	10	14.65	19.842
$0.22~\mu\mathrm{M}$	4.168	22.66	7.549

**Table 4.10:** Conductivity of pure G-actin in G-buffer (nS/m)

Concentration	Control	Bioptron	Vielight
$4.65~\mu\mathrm{M}$	723.7	6.384	6.351
$0.465~\mu\mathrm{M}$	5.437	17.36	6.539

### 4.4.2 Conductivity in diluted buffer for tubulin

From the literature, it is well established that when tubulin is reconstituted or diluted in a buffer different from BRB80, such as its diluted form BRB8, the surface charge distribution of the protein is altered, leading to an increased electrostatic interaction field. [68] As shown in Figure 4.21, tubulin was tested at various concentrations in BRB8, and it was observed that this buffer drastically decreases the conductivity of tubulin. Remarkably, the conductivity values of these films were even lower than those of films prepared with BRB8 alone, without protein. This effect can be explained by the fact that BRB8, having a lower ionic strength than BRB80, produces a broader and less screened ionic cloud around the protein. Consequently, the effective charge mobility is reduced, resulting in decreased conductivity in the protein-loaded films compared to the buffer-only control.

In contrast, when the protein was diluted in BRB8, Vielight maintained conductivity values similar to the control, while Bioptron increased conductivity only at higher concentrations. These results highlight how the type of electromagnetic stimulation and the buffer composition strongly influence the electrical properties of tubulin films.

As can be observed, electromagnetic irradiation with either Vielight or Bioptron does not significantly affect the conductivity of tubulin when the protein is diluted in BRB8.

By following the equations outlined in the previous paragraph, it was possible to calculate the specific contribution of tubulin to conductivity when diluted in BRB8. The results show that the values remain within the same order of magnitude in both BRB8 and BRB80. Table 4.12

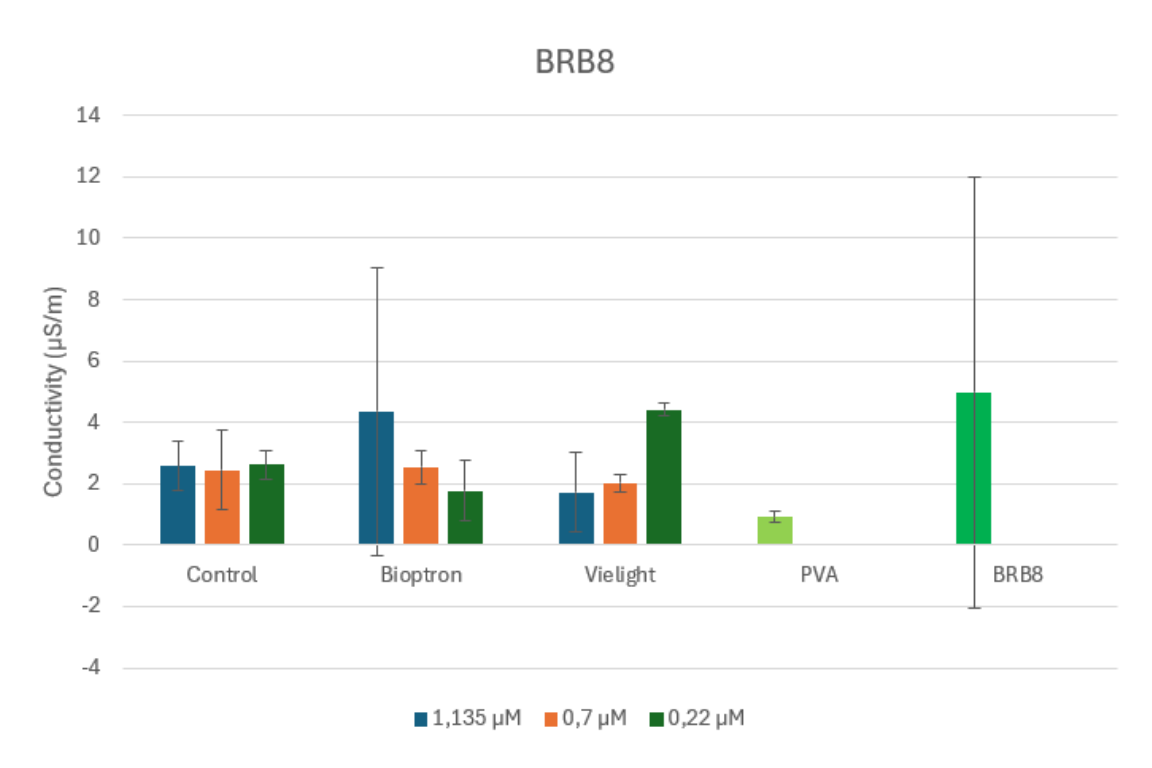


Figure 4.21: Conductivity of tubulin in BRB8

**Table 4.11:** Conductivity of tubulin in BRB8 ( $\mu$ S/m)

Concentration	Control	Bioptron	Vielight
$1.135 \; \mu \text{M}$	2.58513	3.34972	1.72176
$0.7~\mu\mathrm{M}$	2.45038	2.55164	2.01816
$0.222~\mu\mathrm{M}$	2.62188	1.76681	4.11686

Table 4.12: Conductivity of pure tubulin in BRB8 (nS/m)

Concentration	Control	Bioptron	Vielight
$1.135 \; \mu { m M}$	8.527	31.67	3.597
$0.7~\mu\mathrm{M}$	8.404	14.96	4.835
$0.22~\mu\mathrm{M}$	10.48	3.811	38.51

## Chapter 5

## Discussion

## 5.1 DLS analysis

Dynamic Light Scattering (DLS) provided detailed insights into the effects of buffer composition and electromagnetic field stimulation on tubulin and G-actin. As expected, the hydrodynamic diameter measurements confirmed that the concentration of dimethyl sulfoxide strongly influences protein behavior. Increasing DMSO concentration led to a larger size, consistent with previous studies showing that DMSO alters the hydration shells and can trigger the early stages of aggregation. [66] The use of colchicine and latrunculin successfully prevented spontaneous polymerization, allowing an accurate assessment of monomer stability over time. The control samples exhibited only minor changes over 24 hours, consistent with the known partial instability of tubulin and G-actin, supporting the reliability of the experimental setup.

The introduction of electromagnetic field stimulation introduces additional complexity. In tubulin, Bioptron induced an immediate reduction in the average diameter at 15% DMSO, alongside the emergence of smaller populations over time. This observation suggests that polarized broad-spectrum irradiation may interfere with  $\alpha$ - $\beta$  dimer interactions or cause partial unfolding. However, for all other DMSO concentrations, Bioptron was associated with a slight increase in hydrodynamic diameter, implying that this of stimulation typically results in an expansion of the protein hydration shell. Vielight, which delivers narrowband near-infrared light, exhibited more subtle effects, yet still led to the appearance of low-diameter populations at certain concentrations. These findings suggest that both devices modulate tubulin structure.

G-actin, on the contrary, showed greater resilience: Bioptron stimulation transiently increased the heterogeneity of size distributions at baseline, but the effect dissipated at later time points, while Vielight induced minimal changes. Overall,

stimulation led to an increase in the hydrodynamic diameter.

Zeta potential measurements provided further insight into the electrostatic behavior of G-actin and tubulin upon exposure to light stimulation. Under all experimental conditions, a moderate increase in the hydrodynamic diameter was observed, implying a minor conformational expansion or enhanced hydration.

For tubulin in MES80, Bioptron induced a gradual shift toward less negative zeta potential values, most evident at 6 h, while G-actin remained largely stable, indicating lower sensitivity. In the MES80 3X, both proteins initially exhibited more negative zeta potential values and demonstrated variable trends in response to Bioptron stimulation, culminating in less negative values after 24 hours. This behavior aligns with phenomena such as ionic screening and dynamic surface rearrangements. Vielight produced a similar pattern in MES80 but caused a progressive zeta potential reduction over time in MES80 3X, starting from more negative values than controls, suggesting a distinct time-dependent relaxation effect.

In MES50, the variations among treatments were minimal, reflecting weaker modulation at reduced ionic strength. Overall, these results suggest that light stimulation causes a minor expansion of the protein shell and influences the surface charge in a buffer- and protein involved, with Bioptron demonstrating more potent and variable effects compared to Vielight..

#### 5.2 Turbidity assays

Turbidity assays investigating the dynamics of polymerization through light stimulation demonstrated that initial measurements indicated a faster rise in absorbance in samples stimulated with Bioptron and Vielight compared to the control. This suggests that exposure to light impacts the nucleation and elongation phases of microtubule assembly. The steeper slopes and higher final optical density values observed in the stimulated samples suggest an enhancement of the assembly process due to photostimulation.

However, when the samples at 4 °C for a duration of two hours followed by reanalysis post-GTP addition revealed a divergent trend. The findings demonstrate that electromagnetic stimulation affects tubulin polymerization, which is significantly contingent on both the duration of exposure and the specific device employed. Notably, Bioptron stimulation predominantly influenced the kinetics of assembly: after a period of 10 minutes, there was an observed 50% reduction in turbidity and a delay in polymerization, which implies either a partial destabilization of nucleation centers or the generation of non-productive aggregates. However, Bioptron at 20 minutes improved turbidity, while after 30 minutes the effect was mainly a slowing of the polymerization rate, consistent with altered

nucleation efficiency but preserved final assembly. In contrast, Vielight stimulation exhibited a distinct pattern. Following 10 minutes of exposure, the turbidity curves post-storage presented an inverse trend compared to the initial measurement, suggesting measurements, indicative of thermal depolymerization at 37 °C. This destabilizing phenomenon was absent with prolonged exposure. At 20 minutes, the turbidity levels remained largely unaltered compared to the baseline, while at 30 minutes, Vielight accelerated assembly and an increase in turbidity, signifying enhanced polymerization proficiency. The results align with prior findings [20], which documented a concentration-dependent biphasic effect of near-infrared photobiomodulation on tubulin. Mechanistically, these divergent outcomes may result from photostimulation-induced alterations in the interfacial water layer or the expansion of exclusion zone water, both of which can impact tubulin conformations and the efficacy of dimer-dimer interactions. In this context, the observed immediate enhancement of polymerization may reflect conformational states that temporarily encourage nucleation and elongation, while the reduced ability to reassemble after storage could imply long-term destabilization or the formation of non-productive aggregates.

#### 5.3 Raman Spectroscopy

The appearance of a single band at ~1595–1600 cm<sup>-1</sup> with no resolvable Amide I at ~1650 cm<sup>-1</sup> and Amide II ~1550 cm<sup>-1</sup> is most plausibly explained by buffer contributions and pre-processing effects rather than by a genuine loss of the peptide C=O signal. In BRB80 with GTP and cushion buffer, intense ring vibrations (PIPES/GTP) in the 1570–1610 cm<sup>-1</sup> region, together with fluorescence/background removal and smoothing, can dominate the 1500–1700 cm<sup>-1</sup> window and mask the broad Amide I and Amide II envelope. This interpretation is consistent with the lack of differences between stimulated and control spectra. Notably, FT-Raman is known to exhibit minimal water interference in the Amide I region, while accurate analysis of overlapping peaks requires advanced fitting methods (e.g., second-derivative or Voigt profiles) to resolve hidden Amide I components [69]. Furthermore, suppression of the Amide I band has been documented in surface-enhanced Raman contexts, where aromatic or side-chain vibrations dominate due to selection rules [70].

A similar interpretation applies to G-actin, which exhibited neither distinct Amide I nor Amide II bands, presenting instead a broad, low-intensity signal spanning  $1500-1700~\rm cm^2$ . In the G-buffer formulation used here, ATP contributes pronounced adenine ring vibrations within the  $\sim 1570-1610~\rm cm^3$  range, whereas Tris/HEPES and DTT introduce additional background and fluorescence. These factors, following baseline correction and smoothing procedures, may flatten or obscure the Amide I region. The lack of spectral variation between stimulated and

control conditions supports the notion that the observed profiles are primarily influenced by buffer and preprocessing effects, rather than by light-induced structural alterations.

Analysis of the 1200–1400 cm<sup>-1</sup> region, encompassing the Amide III band and  $\rm CH_2/COO^-$  vibrations, further confirmed the lack of irradiation-induced alterations. Tubulin spectra displayed two clear peaks at ~1300 and ~1380 cm<sup>-1</sup>, whereas G-actin showed a smoother profile without well-resolved Amide III features. In both cases, Bioptron-stimulated spectra exhibited a modest, uniform decrease in intensity but no appreciable peak shifts, indicating that secondary structure was largely preserved and that the reduced signal may reflect experimental factors such as scattering efficiency rather than genuine conformational rearrangements.

### 5.4 Conductivity analysis

The conductivity measurements provide a comprehensive view of how tubulin and G-actin respond to different buffer conditions and light stimulation, offering complementary information to the structural and polymerization data obtained with DLS and turbidity. Conductivity reflects not only the intrinsic properties of the proteins but also their interactions with the surrounding ionic environment, therefore providing insights into how cytoskeletal proteins contribute to charge transport in solution. In this context, changes in conductivity correspond to alterations in the flow of ions within the medium, which can be influenced by protein concentration, conformational state and light-induced rearrangements of the solvent network.

In BRB80 buffer, the electrical conductivity associated with free tubulin was relatively low, measured within the nano Siemens per meter range. At the maximum concentration examined (2.27  $\mu$ M), the conductivity attained a peak value of approximately 73 nS/m, gradually declining to 4 nS/m at a concentration of 0.22  $\mu$ M. These observations suggest that free tubulin exhibits a limited contribution to ionic conduction, with the effect being directly proportional to protein concentration. In particular, tubulin exposed to electromagnetic fields showed opposite trends for the two light sources. Under infrared stimulation, conductivity decreased compared with the control, especially at higher concentrations. This reduction may result from the absorption of infrared light by the solution, which can disrupt the water network and reduce ionic mobility. In contrast, under hyperpolarized light, there was an increase in conductivity, indicating that the light is primarily absorbed by the protein, leading to release or rearrangement of ions into the surrounding medium, which enhances charge flow. Although conductivity in tubulin is frequently associated with its polymerized microtubule form, in these PVA films, the protein maintained its dimeric state. The effects observed are thus likely reflect

light-induced conformational or electrostatic changes in the tubulin dimers, which modulate their interaction with the polymer matrix and subsequently influence charge transport. In the BRB8 buffer, tubulin demonstrated contrary behavior: Vielight stimulation resulted in an enhancement of conductivity, potentially attributable to increased protein absorption within this buffer, which facilitates the reorganization of charges and improved ionic translocation. Conversely, Bioptron application resulted in decreased conductivity, likely due to differential wavelength absorption and constrained ion release under these specific conditions. This underscores the significant influence of the ionic environment in modulating light-protein interactions, consequently yielding varied electrical outcomes contingent upon the buffer composition.

In contrast, G-actin in G-buffer demonstrated extraordinarily high conductivity at elevated concentration: at 4.65  $\mu$ M, values reached 724 nS/m. This remarkable property suggests that even monomeric G-actin can facilitate charge transfer, likely cause of the abundance of acidic surface residues that interact strongly with ions in solution. However, G-actin was also highly sensitive to light stimulation. Following exposure to either Bioptron or Vielight, conductivity collapsed to values below 10 nS/m, representing a drop of nearly two orders of magnitude compared with the non-stimulated condition. This effect highlights how conformational or electrostatic rearrangements triggered by irradiation can drastically alter the charge transport capacity of actin. At lower concentrations, tubulin and actin exhibited more comparable conductivity values, with Bioptron in some cases producing slight increases. These observations emphasize that conductivity in actin is strongly dependent on protein concentration but also on conformational stability and its ability to respond to external perturbations.

A comparative analysis of the two proteins reveals distinct electrical properties. Tubulin, in its dimeric form, demonstrates relatively low conductivity and appears to necessitate polymerization into microtubules to efficiently serve as a conduit for charge transport. In contrast, G-actin demonstrates high conductivity as a monomer; however, this property is significantly diminished upon exposure to irradiation. This dichotomy may reflect their diverse biological roles: microtubules operate as relatively stable 'biological wires,' facilitating long-range charge or signal transmission, whereas actin functions as a flexible regulator of the local ionic microenvironment, exhibiting high dynamism but less reliability for sustained conduction.

The divergence between Bioptron and Vielight effects can be linked to their irradiation characteristics. Vielight delivers a single near-infrared wavelength, likely producing uniform structural or electronic modifications across proteins, resulting in more consistent conductivity values. Bioptron, in contrast, emits broad-spectrum polarized light, increasing the probability of multiple wavelengths interacting with

distinct protein residues or conformational states, thereby producing concentration-dependent and less predictable effects. This interpretation agrees with previous studies indicating that protein–light interactions can vary substantially depending on wavelength specificity.

In conclusion, the findings demonstrate that cytoskeletal proteins exhibit a differential sensitivity to light stimulation, which is influenced by their structural attributes and the spectral properties of the irradiation. Across all examined conditions, both Bioptron and Vielight induced a modest enhancement in hydrodynamic diameter, suggestive of conformational expansion or increased hydration of the protein shell. These structural rearrangements directly affect ionic mobility and charge flow, explaining the conductivity changes observed under stimulation: larger protein shells and modified hydration layers can alter the local distribution of ions, either facilitating or blocking their movement depending on the irradiation type and buffer composition.

Tubulin responded in a dual, context-dependent manner: broad-spectrum polarized light from Bioptron produced heterogeneous and concentration-dependent effects, temporarily accelerating polymerization but reducing reassembly after storage, whereas single-wavelength near-infrared irradiation from Vielight induced more uniform, though overall less disruptive, modifications. Actin, on the contrary, showed marked alterations in conductivity and filament diameter under broad-spectrum stimulation, suggesting that its electrostatic properties and hydration shell are more strongly perturbed than those of tubulin.

Taken together, these findings highlight that wavelength composition in determining the magnitude of structural and electrostatic alterations. This positions the cytoskeleton as an active component of cellular electrostatics and presents opportunities for the targeted modulation of protein dynamics and charge transport through photostimulation.

## Chapter 6

# Conclusions and Future developments

This work investigated how cytoskeletal proteins, specifically tubulin and G-actin, respond to electromagnetic stimulation, combining DLS, turbidity, raman spectroscopy and conductivity measurements. The results revealed distinct and complementary behaviors: tubulin showed low intrinsic conductivity and modest stability in its dimeric form, but evidence suggests that its polymerized microtubules may act as biological conductors. [44] Light stimulation improved short-term polymerization, but also induced destabilization on longer time scales. In contrast, actin showed unexpectedly high conductivity in its monomeric form, attributable to surface-exposed acidic residues, but was highly sensitive to irradiation.

These findings underscore that the cytoskeleton should not be regarded as merely a static scaffold but an electrostatically active system responsive to external light stimuli. The dual sensitivity of tubulin and G-actin implies that different filamentous structures may be selectively modulated contingent upon the wavelength and polarization of the applied stimulus. These insights hold significant implications for fundamental biological research as well as therapeutic methodologies. For tubulin, the observation that microtubule stability and charge distribution can be altered by irradiation points to possible strategies for influencing neuronal transport and mitosis. Since microtubule dysfunction contributes to neurodegenerative diseases such as Alzheimer's, controlled stimulation might stabilize microtubules or counteract pathological aggregation. For actin, extreme sensitivity to light could be relevant for synaptic plasticity and immune responses, where actin turnover plays a critical role. Modulation of actin dynamics with near-infrared or polarized light could therefore influence neuronal connectivity, learning and immune function.

In Alzheimer's disease, cytoskeletal breakdown is a key pathological characteristic. Devices like Vielight, already explored in clinical pilot studies, could

be refined to preserve microtubule function or modulate neuronal electrostatics. [20] Bioptron, while showing stronger effects, may require careful optimization to avoid destabilization. Similarly, in depression, where impaired synaptic plasticity is associated with actin dysfunction, photostimulation could improve dendritic spine remodeling and improve mood and cognition. Beyond the nervous system, actin-related diseases, such as cardiomyopathies or immune disorders, may also benefit from approaches that restore actin function through external light-based modulation. On a mechanistic level, the findings indicate that photostimulation disrupts protein electrostatics by modifying hydration shells, dimer interfaces, or surface charge distributions. The differential responses of tubulin and actin highlight their unique structural principles: microtubules function as stable pathways for long-range conduction, whereas actin operates as a versatile regulator of the local ionic microenvironment. This perspective reconceptualizes the cytoskeleton as an active biophysical entity in intracellular communication, rather than merely a passive framework.

Under the current experimental conditions, Raman spectroscopy yielded limited information. Consequently, ongoing efforts will focus on optimizing sample preparation, buffer selection, and spectral deconvolution to enhance the resolution of the Amide I and Amide III regions.

Several limitations must be acknowledged. The investigations were conducted in simplified systems comprising purified proteins, whereas the cellular environment includes regulatory proteins, post-translational modifications, and compartmentalized ionic gradients. Consequently, *in vivo* responses may differ substantially. Furthermore, although the findings indicate concentration- and device-dependent effects, the precise molecular mechanisms remain unclear. Future studies should utilize advanced structural and spectroscopic techniques, in conjunction with live-cell imaging, to elucidate how light modulates cytoskeletal function.

Animal models of Alzheimer's disease, depression and actin-related disorders represent critical next steps to determine whether these effects translate into physiological or therapeutic benefits. Equally important will be systematic optimization of device parameters, such as wavelength, intensity, polarization and duration, to maximize benefits while minimizing risks.

In conclusion, this study shows that electromagnetic stimulation can differentially modulate tubulin and actin, altering their structural stability and electrostatic properties. The data highlight the promise of photobiomodulation as a means of influencing cytoskeletal biology and potentially treating diseases where cytoskeletal dysfunction plays a role. At the same time, they caution that the effects are complex, context-dependent and require rigorous validation. Therefore, more studies are essential to confirm these observations, elucidate mechanisms and assess clinical relevance. Only through such research will the potential for light-based modulation of the cytoskeleton be fully realized.

## Appendix

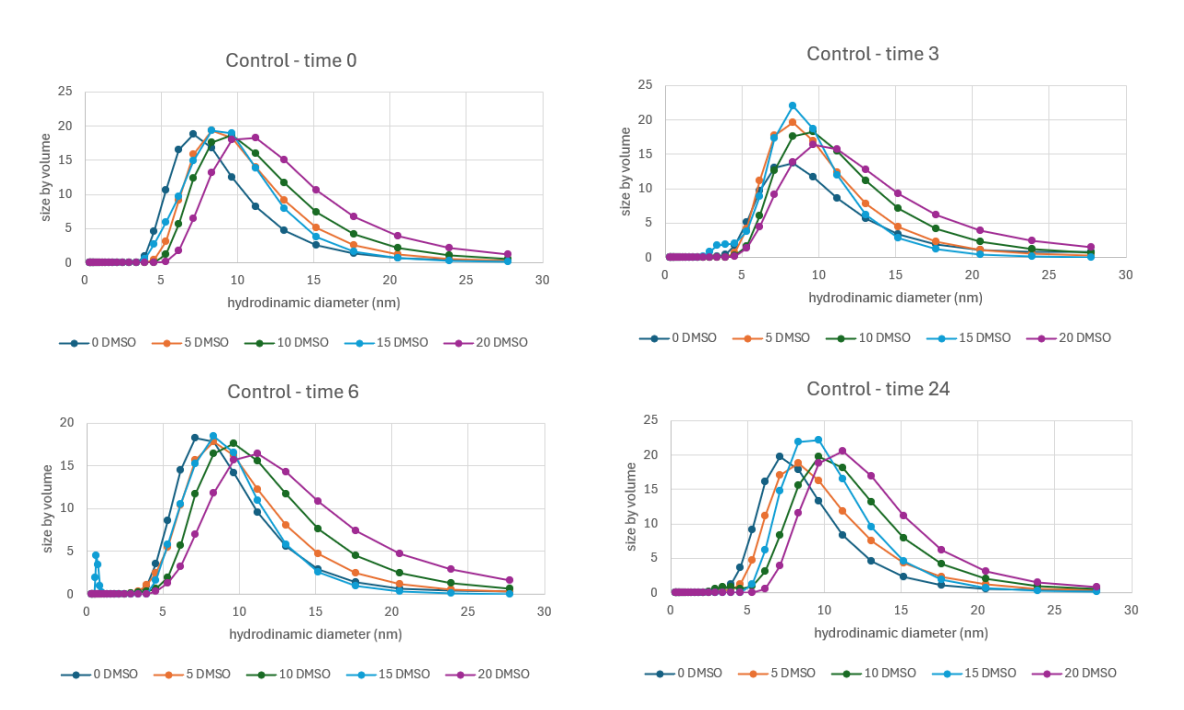


Figure 6.1: Size by volume: tubulin control at time points 0, 3, 6, and 24.

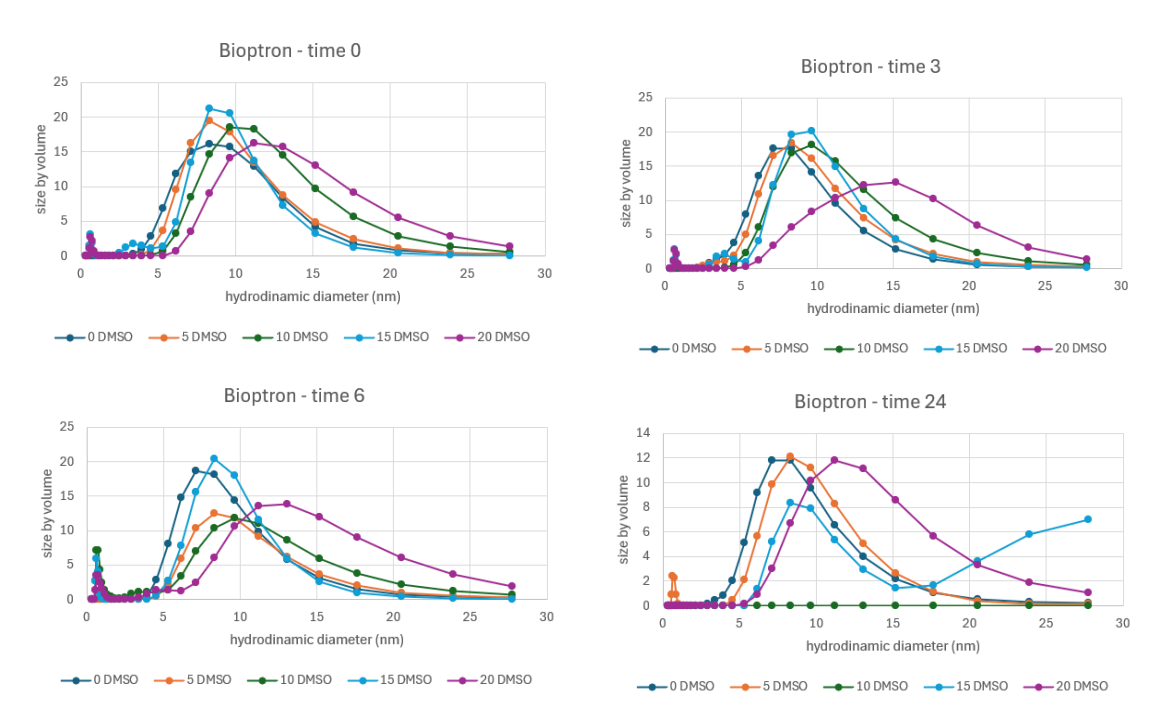


Figure 6.2: Size by volume: tubulin Bioptron at time points 0, 3, 6, and 24.

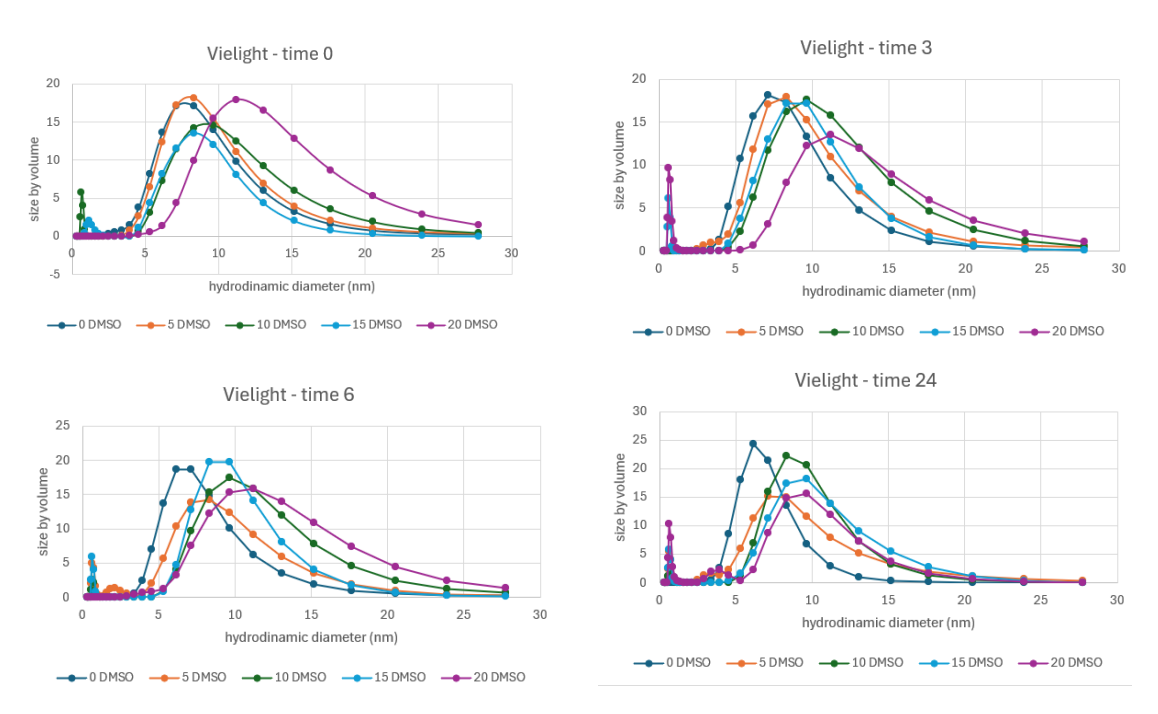


Figure 6.3: Size by volume: tubulin Vielight at time points 0, 3, 6, and 24.

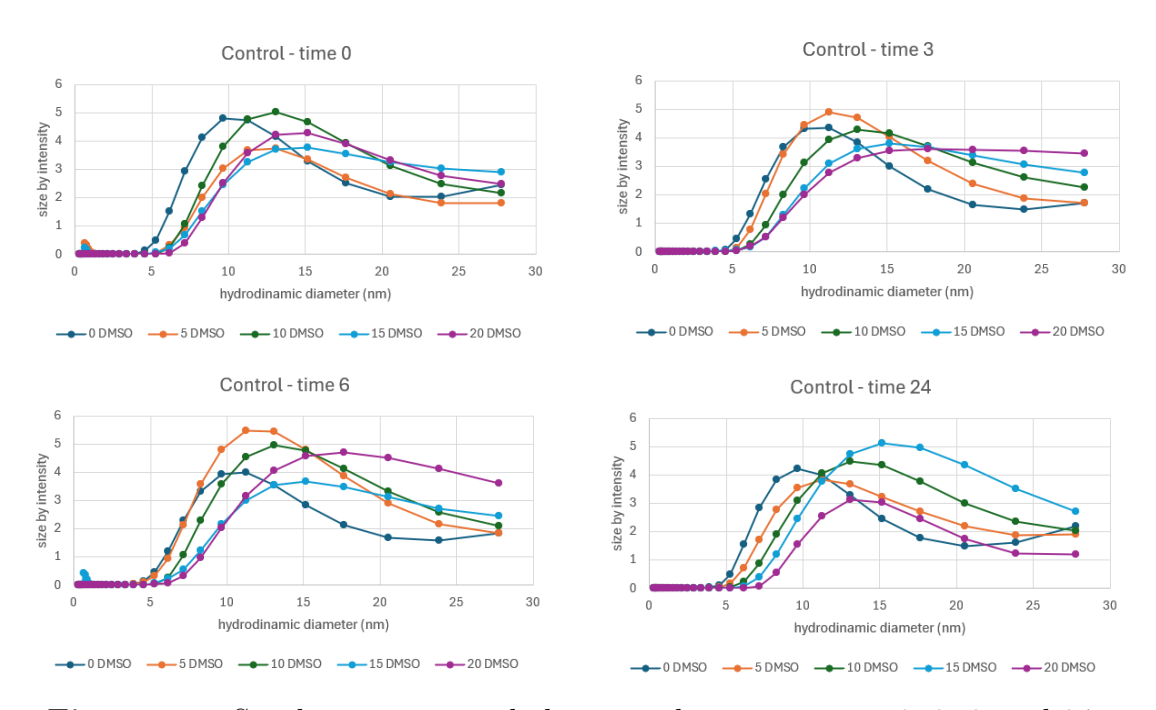


Figure 6.4: Size by intensity: tubulin control at time points 0, 3, 6, and 24.

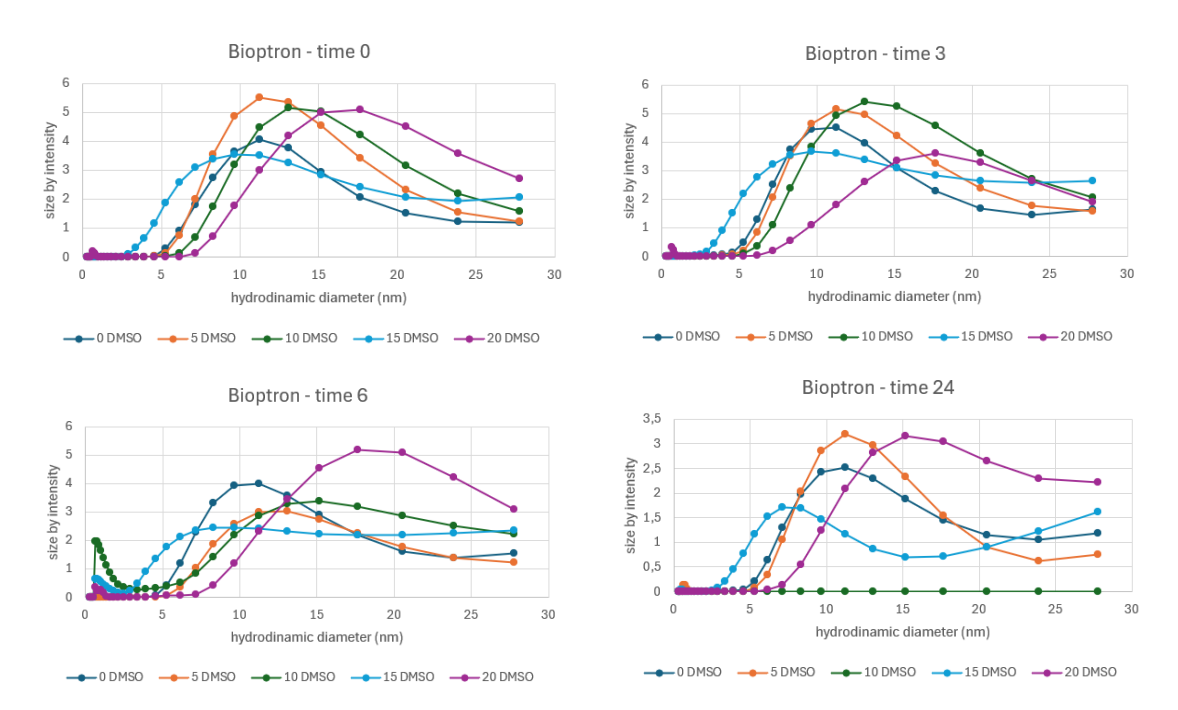


Figure 6.5: Size by intensity: tubulin Bioptron at time points 0, 3, 6, and 24.

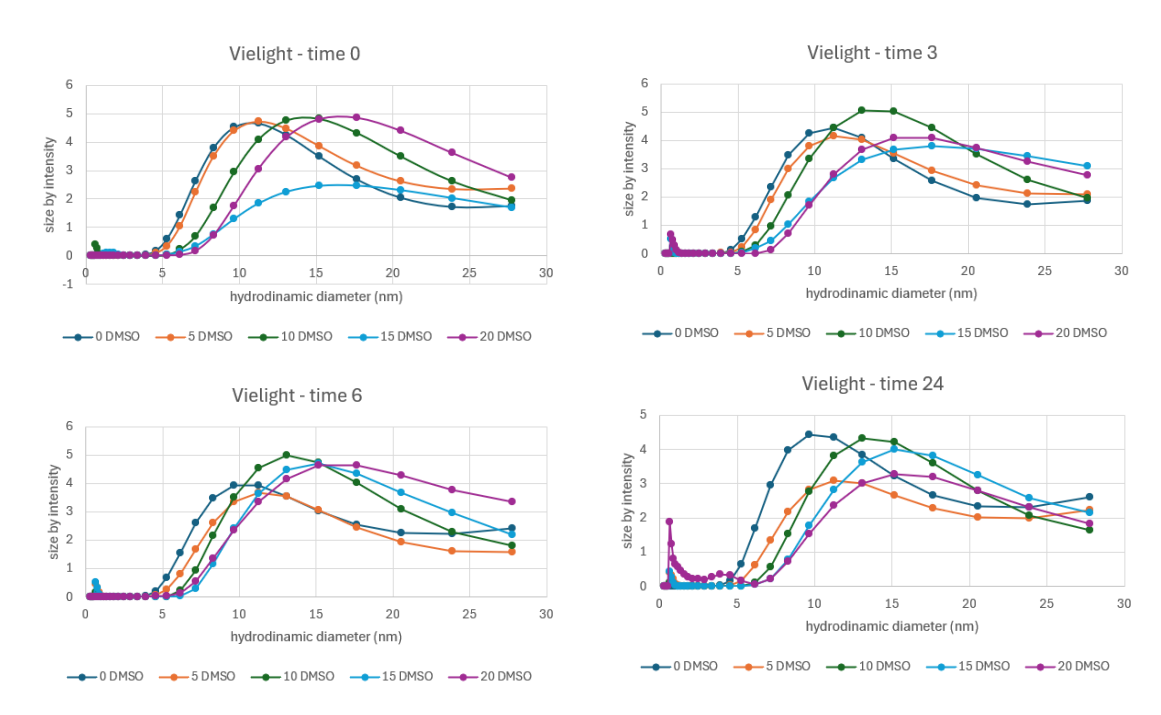


Figure 6.6: Size by intensity: tubulin Vielight at time points 0, 3, 6, and 24.

Table 6.1: Control on tubulin

% DMSO (V/V)				Xc by	volume			
	Time 0	SE	Time 3	SE	Time 6	SE	Time 24	SE
0	6.8553	0.094	8.311	0.724	7.226	0.567	6.969	0.024
5	8.340	0.302	7.733	0.587	8.084	0.394	8.028	0.290
10	9.246	0.384	8.855	0.156	9.187	0.486	8.826	0.062
15	9.011	1.340	8.759	0.860	9.105	1.076	9.358	1.146
20	10.512	0.571	9.983	0.624	9.037	1.261	10.915	0.257

Table 6.2: Bioptron on tubulin

% DMSO (V/V)				Xc b	y volume						
	$\overline{\text{Time 0}}$	Time 0 SE Time 3 SE Time 6 SE Time 24 SE									
0	7.484	0.345	7.231	0.191	7.537	0.149	6.142	0.750			
5	8.260	0.041	8.082	0.145	8.475	0.110	7.089	0.420			
10	10.600	0.000	9.183	0.739	8.912	2.272	2082.850	1700.395			
15	7.547	0.531	9.437	0.319	8.352	1.388	21.660	9.280			
20	12.107	0.753	12.388	2.222	10.400	1.060	11.225	0.989			

Table 6.3: Vielight on tubulin

% DMSO (V/V)				Xc by	volume			
	$\overline{\text{Time 0}}$	SE	Time 3	SE	Time 6	SE	Time 24	$\mathbf{SE}$
0	7.280	0.094	6.934	0.148	6.644	0.325	7.201	1.360
5	7.581	0.395	7.530	0.229	6.543	0.556	7.552	0.075
10	7.914	1.725	9.200	0.445	9.917	0.710	9.083	0.339
15	9.294	1.322	8.871	1.699	9.255	0.897	9.178	0.741
20	10.903	0.570	9.353	2.405	10.073	1.178	9.737	3.220

Table 6.4: Control on tubulin

% DMSO (V/V)			-	Xc by i	intensity			
	$\overline{\text{Time 0}}$	SE	Time 3	SE	Time 6	SE	Time 24	$\mathbf{SE}$
0	10.196	1.764	10.529	0.559	12.687	1.516	9.812	0.128
5	11.632	0.243	12.878	1.299	12.223	0.428	12.388	0.230
10	13.942	0.519	14.786	0.878	13.956	0.896	13.844	1.487
15	15.650	0.424	14.907	2.048	16.953	0.918	16.580	1.400
20	19.176	1.440	21.543	4.104	16.755	0.790	17.756	3.480

Table 6.5: Bioptron on tubulin

% DMSO (V/V)			]	Xc by i	intensity			
	$\overline{\text{Time 0}}$	SE	Time 3	SE	Time 6	SE	Time 24	SE
0	12.658	2.090	12.600	1.621	13.846	1.490	13.230	4.560
5	11.754	0.357	11.615	0.228	14.281	1.547	11.413	0.149
10	13.683	0.826	13.400	0.715	14.350	2.626	5468	0.000
15	12.348	2.156	13.766	0.706	11.272	2.225	9.070	8.862
20	17.749	2.550	16.786	2.313	17.023	1.299	21.509	0.423

Table 6.6: Vielight on tubulin

% DMSO (V/V)			-	Xc by i	intensity			
	$\overline{\text{Time 0}}$	SE	Time 3	SE	Time 6	SE	Time 24	SE
0	12.021	1.736	12.648	1.867	10.442	0.304	10.645	0.343
5	11.667	0.209	11.940	0.053	11.728	0.473	13.134	0.473
10	14.264	0.818	13.927	0.472	13.381	0.580	14.155	0.990
15	9.951	4.708	19.480	2.910	16.304	0.843	15.258	0.290
20	17.208	0.822	18.267	2.560	18.800	1.924	15.830	4.633

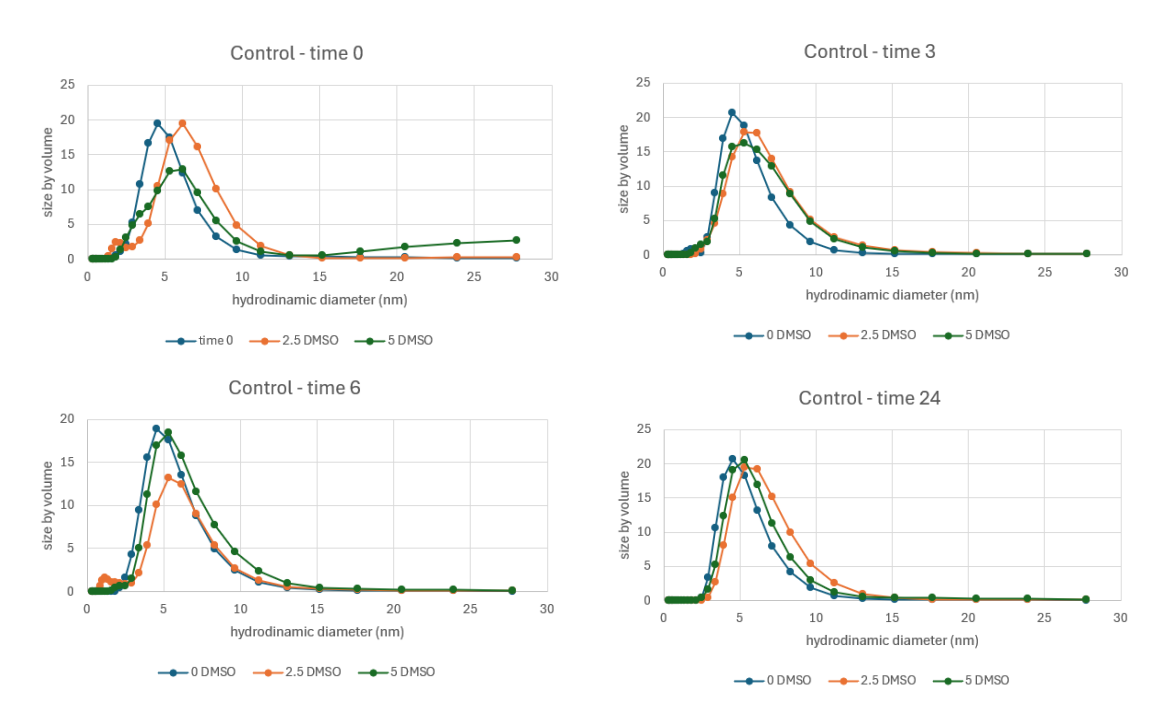


Figure 6.7: Size by volume: G-actin control at time points 0, 3, 6, and 24.

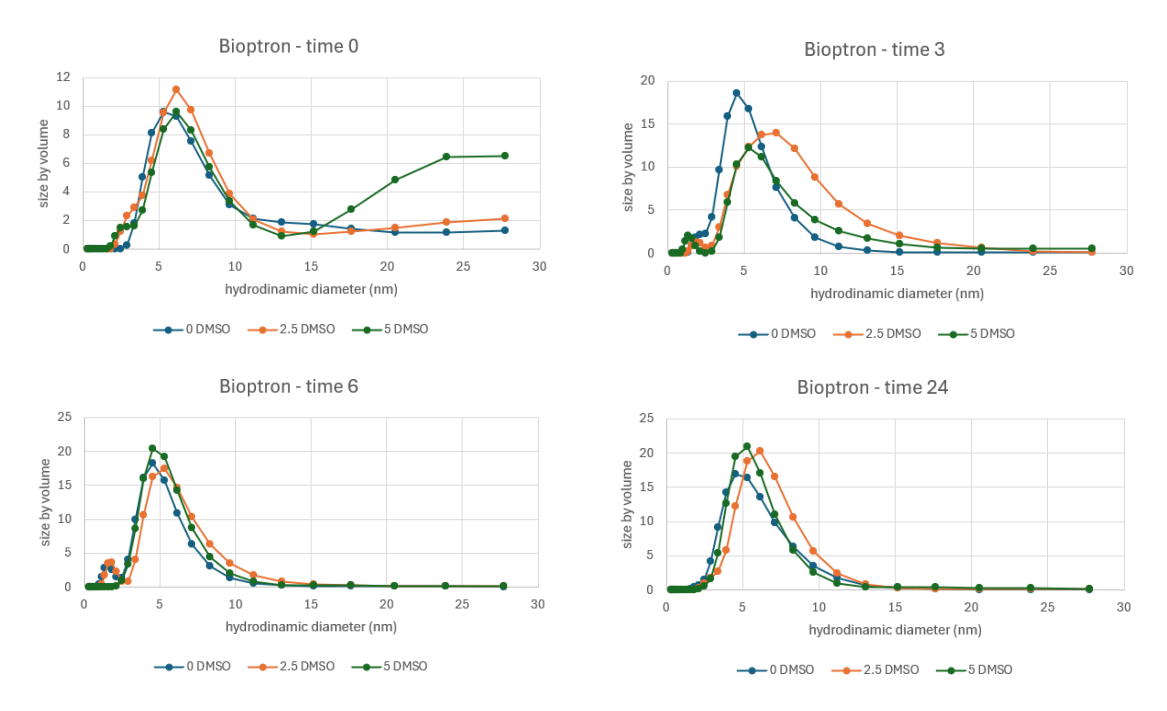


Figure 6.8: Size by volume: G-actin Bioptron at time points 0, 3, 6, and 24.

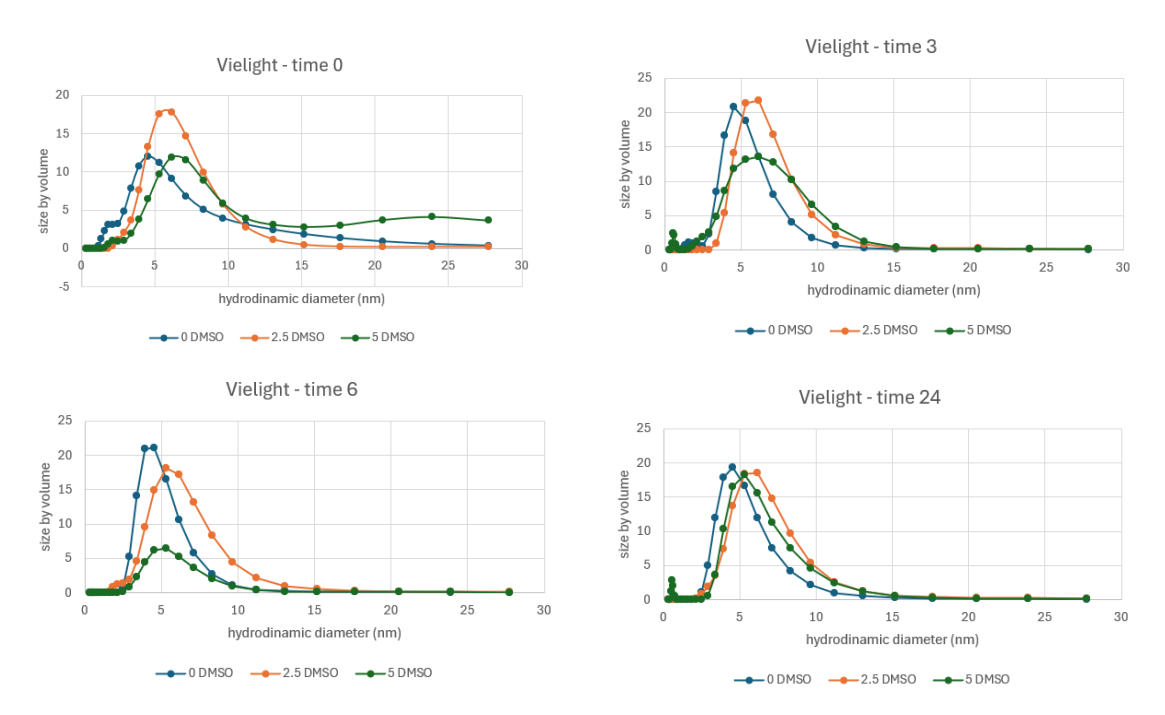


Figure 6.9: Size by volume: G-actin Vielight at time points 0, 3, 6, and 24.

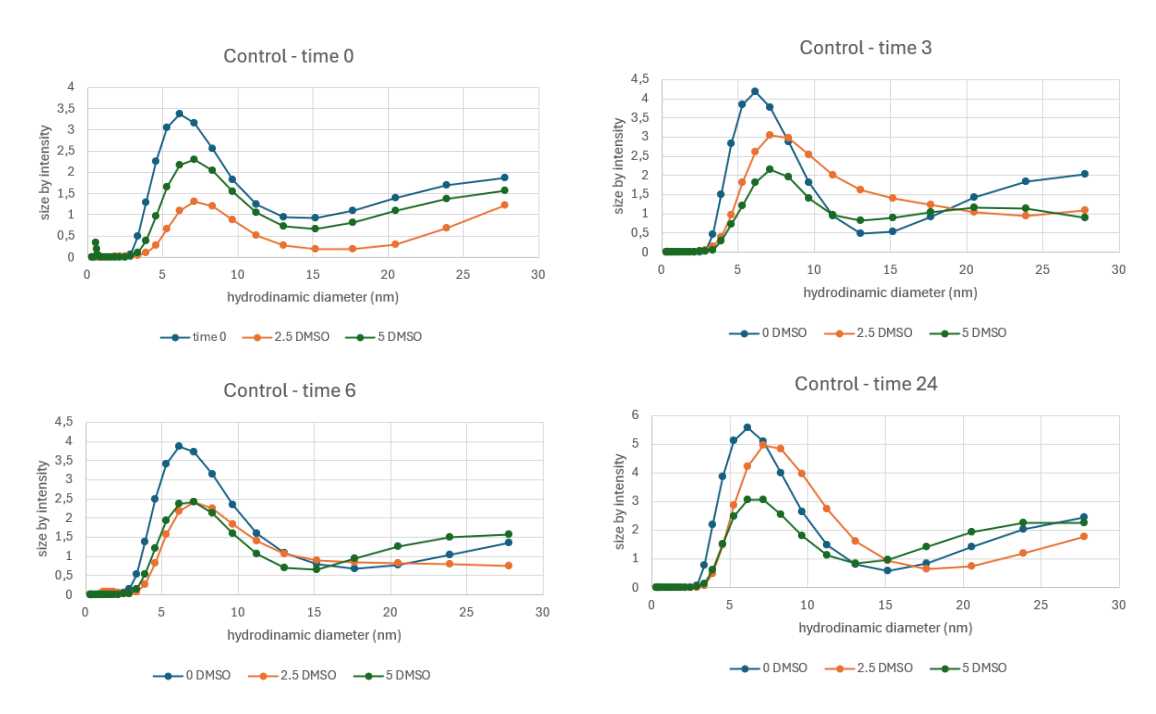


Figure 6.10: Size by intensity: G-actin control at time points 0, 3, 6, and 24.

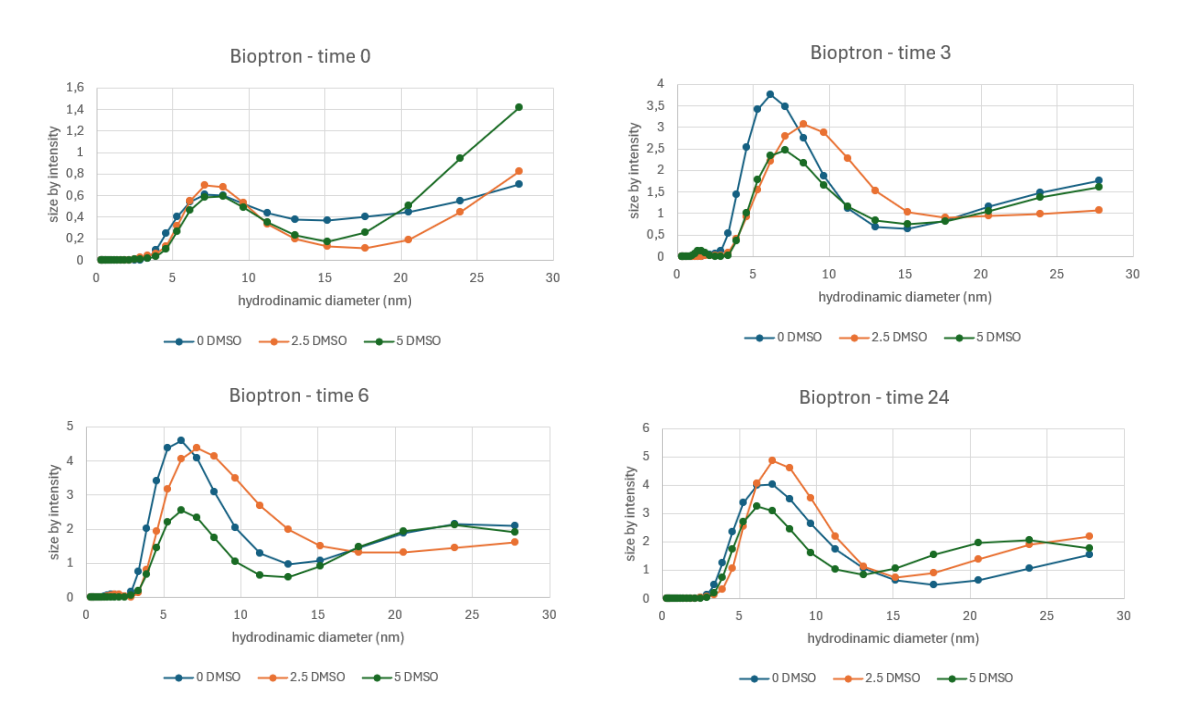


Figure 6.11: Size by intensity: G-actin Bioptron at time points 0, 3, 6, and 24.

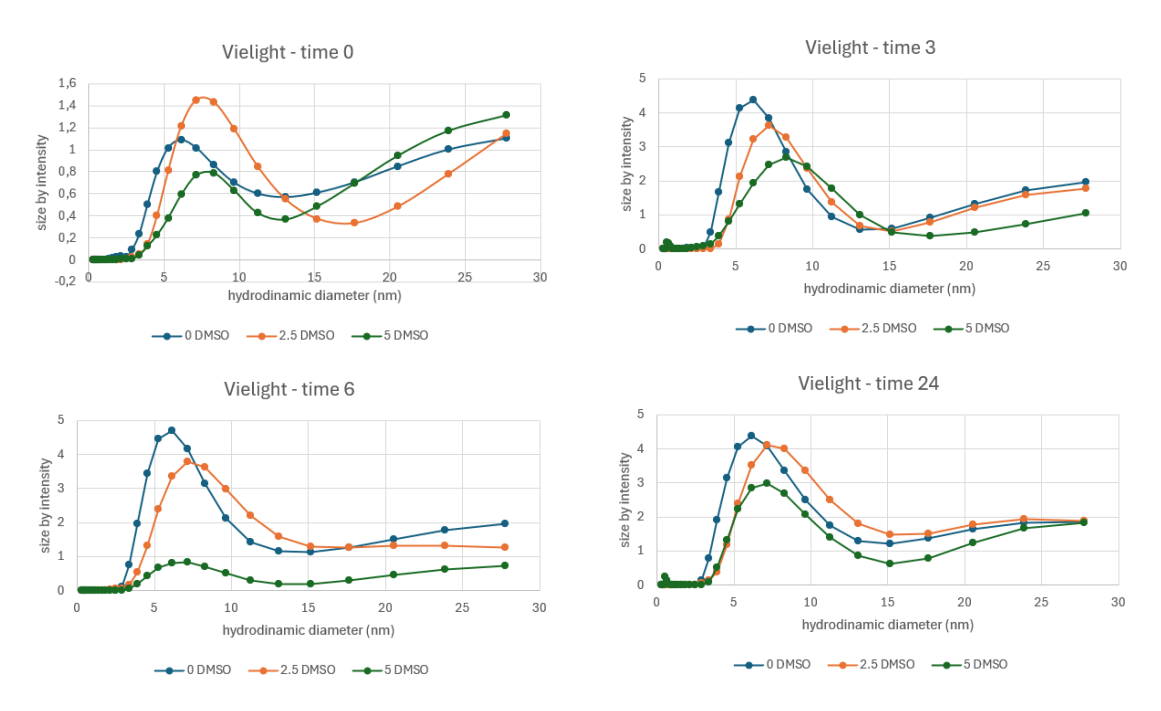


Figure 6.12: Size by intensity: G-actin Vielight at time points 0, 3, 6, and 24.

**Table 6.7:** Control — Xc by volume

% DMSO (V/V)				Xc by	volume			
	$\overline{\text{Time 0}}$	SE	Time 3	SE	Time 6	SE	Time 24	SE
0	4.961	0.344	5.336	0.057	5.334	0.058	5.016	0.206
2.5	3.799	1.530	5.371	0.527	3.772	1.303	5.476	0.199
5	7.520	1.859	6.065	0.594	6.180	0.359	5.917	0.144

**Table 6.8:** Bioptron — Xc by volume

% DMSO (V/V)				Xc by	volume			
	$\overline{\text{Time 0}}$	SE	Time 3	SE	Time 6	SE	Time 24	SE
0	8.034	0.456	4.856	0.372	4.445	0.383	5.137	0.406
2.5	10.519	2.540	6.370	1.460	4.474	0.416	5.3618	0.206
5	9.769	1.830	6.718	1.501	5.583	0.437	5.453	0.452

**Table 6.9:** Vielight — Xc by volume

% DMSO (V/V)				Xc by	volume			
	Time 0	SE	Time 3	SE	Time 6	SE	Time 24	SE
0	5.880	1.669	5.172	0.119	5.048	0.229	5.139	0.085
2.5	5.575	0.514	5.737	0.114	5.181	0.293	5.326	0.328
5	7.306	0.184	6.112	0.934	5.623	0.457	6.006	0.586

**Table 6.10:** Control — Xc by intensity

% DMSO (V/V)			-	Xc by	intensity			
	Time 0	$\mathbf{SE}$	Time 3	SE	Time 6	SE	Time 24	SE
0	17.673	5.453	7.238	0.083	8.456	1.317	7.227	0.197
2.5	16.123	8.140	9.939	2.422	6.872	3.188	7.604	0.006
5	10.182	1.461	12.890	1.564	12.145	4.197	11.185	0.134

**Table 6.11:** Bioptron — Xc by intensity

% DMSO (V/V)			-	Xc by	intensity			
	Time 0	$\mathbf{SE}$	Time 3	$\mathbf{SE}$	Time 6	$\mathbf{SE}$	Time 24	$\mathbf{SE}$
0	8.037	4.007	7.117	0.204	6.883	0.144	8.676	1.405
2.5	19.732	6.950	9.952	1.290	7.996	0.456	8.693	1.258
5	17.454	6.986	10.385	2.064	11.445	1.574	12.442	3.355

Table 6.12: Vielight — Xc by intensity

% DMSO (V/V)	Xc by intensity							
	$\overline{\text{Time 0}}$	SE	Time 3	SE	Time 6	SE	Time 24	SE
0	10.646	1.265	7.038	0.066	6.959	0.232	7.699	0.354
2.5	10.813	1.345	8.225	0.813	8.040	0.664	8.022	0.435
5	13.777	2.816	9.912	1.147	4.412	4.112	8.117	0.402

## **Bibliography**

- John Roche. «Introducing electric fields». In: *Physics Education* 51.5 (2016),
   p. 055005. DOI: 10.1088/0031-9120/51/5/055005 (cit. on p. 3).
- [2] David C. Jiles. *Introduction to Magnetism and Magnetic Materials*. 2nd ed. CRC Press, 1998, p. 3. ISBN: 978-0412798603 (cit. on p. 3).
- [3] A. Lahiri. «Electromagnetic Theory and Optics». In: *Basic Optics*. Elsevier, 2016, pp. 1–140. DOI: 10.1016/b978-0-12-805357-7.00001-0 (cit. on p. 4).
- [4] J. Zhang, D. Xiao, T. Xie, and Q. Ji. «Analysis of Characteristics of the Electric Field Induced by an Angularly Rotating and Oscillating Magnetic Object». In: *Applied Sciences* 14.3 (2024), p. 1321. DOI: 10.3390/app140313 21 (cit. on p. 5).
- [5] Jürgen König. «Eur. J. Phys.» In: European Journal of Physics 42 (2021), p. 045204 (cit. on p. 5).
- [6] M. E. Maffei. «Magnetic Fields and Cancer: Epidemiology, Cellular Biology, and Theranostics». In: *International Journal of Molecular Sciences* 23.3 (2022), p. 1339. DOI: 10.3390/ijms23031339 (cit. on p. 5).
- [7] International Agency for Research on Cancer. *Non-ionizing Radiation, Part 2: Radiofrequency Electromagnetic Fields.* IARC Monographs on the Evaluation of Carcinogenic Risks to Humans, Volume 102. Lyon, France: IARC, 2013 (cit. on pp. 8, 10).
- [8] G. A. Boorman, D. L. McCormick, J. C. Findlay, and et al. «Chronic toxicity/oncogenicity evaluation of 60 Hz (power frequency) magnetic fields in F344/N rats». In: *Toxicologic Pathology* 27.3 (1999), pp. 267–278 (cit. on p. 8).
- [9] S. J. London, J. M. Pogoda, K. L. Hwang, and et al. «Residential magnetic field exposure and breast cancer risk: A nested case—control study from a multiethnic cohort in Los Angeles County, California». In: *American Journal* of Epidemiology 158.10 (2003), pp. 969–980 (cit. on pp. 8, 10).

- [10] S. Davis, D. K. Mirick, and R. G. Stevens. «Residential magnetic fields and the risk of breast cancer». In: *American Journal of Epidemiology* 155.5 (2002), pp. 446–454 (cit. on pp. 8, 10).
- [11] F. D. Groves, W. F. Page, G. Gridley, and et al. «Cancer in Korean war navy technicians: Mortality survey after 40 years». In: *American Journal of Epidemiology* 155.9 (2002), pp. 810–818 (cit. on p. 8).
- [12] C. Dompe et al. «Photobiomodulation-Underlying Mechanism and Clinical Applications». In: *Journal of Clinical Medicine* 9.6 (June 2020), p. 1724. DOI: 10.3390/jcm9061724 (cit. on p. 10).
- [13] LightForce Medical. *Photobiomodulation Therapy (PBM)*. https://lightforcemedical.com/photobiomodulation-therapy-pbm/?utm\_source=chatgpt.com. Accessed: 2025-08-26. 2023 (cit. on p. 10).
- [14] Author(s) Unknown. «Article on photobiomodulation». In: Ageing Research Reviews (2021). DOI: 10.1016/j.arr.2021.101415 (cit. on p. 10).
- [15] Juanita J. Anders, Raymond J. Lanzafame, and Praveen R. Arany. «Low-level light/laser therapy versus photobiomodulation therapy». In: *Photomedicine* and Laser Surgery (2015) (cit. on p. 10).
- [16] Praveen R. Arany. *Photobiomodulation Therapy*. BDS, MDS, MMSc, PhD. n.d. (Cit. on p. 11).
- [17] Li-Chern Pan, Nguyen-Le-Thanh Hang, Mamadi M. S. Colley, Jungshan Chang, Yu-Cheng Hsiao, Long-Sheng Lu, Bing-Sian Li, Cheng-Jen Chang, and Tzu-Sen Yang. «Single Cell Effects of Photobiomodulation on Mitochondrial Membrane Potential and Reactive Oxygen Species Production in Human Adipose Mesenchymal Stem Cells». In: Journal of Forensic Sciences (2025). DOI: 10.1016/j.jfscie.2025.100045 (cit. on p. 11).
- [18] Jalal Maghfour, David M. Ozog, Jessica Mineroff, Jared Jagdeo, Indermeet Kohli, and Henry W. Lim. «Photobiomodulation CME part I: Overview and mechanism of action». In: *Photobiomodulation, Photomedicine, and Laser Surgery* (2025). In press (cit. on p. 11).
- [19] David W. Frankowski et al. «Light buckets and laser beams: mechanisms and applications of photobiomodulation (PBM) therapy». In: Geroscience 47.3 (June 2025), pp. 2777–2789. DOI: 10.1007/s11357-025-01505-z (cit. on p. 11).

- [20] Michael Staelens, Elisabetta Di Gregorio, Aarat P. Kalra, Hoa T. Le, Nazanin Hosseinkhah, Mahroo Karimpoor, Lew Lim, and Jack A. Tuszyński. «Near-Infrared Photobiomodulation of Living Cells, Tubulin, and Microtubules In Vitro». In: Frontiers in Medical Technology (2022). DOI: 10.3389/fmedt. 2022.871196. URL: https://www.frontiersin.org/journals/medical-technology/articles/10.3389/fmedt.2022.871196/full (cit. on pp. 11, 65, 70).
- [21] Elisabetta Di Gregorio, Michael Staelens, Nazanin Hosseinkhah, Mahroo Karimpoor, Janine Liburd, Lew Lim, Karthik Shankar, and Jack A. Tuszyński. «Raman Spectroscopy Reveals Photobiomodulation-Induced -Helix to -Sheet Transition in Tubulins: Potential Implications for Alzheimer's and Other Neurodegenerative Diseases». In: Nanomaterials 14.13 (2024), p. 1093. DOI: 10.3390/nano14131093. URL: https://www.mdpi.com/2079-4991/14/13/1093 (cit. on p. 11).
- [22] Ana Carolina de Magalhães, Zwinglio Guimarães-Filho, Elisabeth Mateus Yoshimura, and Lothar Lilge. «Photobiomodulation therapy can change actin filaments of 3T3 mouse fibroblast». In: Lasers in Medical Science (2020). DOI: 10.1007/s10103-020-02983-8. URL: https://link.springer.com/article/10.1007/s10103-020-02983-8 (cit. on p. 11).
- [23] Jessica Mineroff, Jalal Maghfour, David M. Ozog, Henry W. Lim, Indermeet Kohli, and Jared Jagdeo. «Photobiomodulation CME part II: Clinical applications in dermatology». In: *Photobiomodulation, Photomedicine, and Laser Surgery* (2025). In press (cit. on p. 11).
- [24] Qi Wang, Phil-Sun Oh, and Hwan-Jeong Jeong. «From molecular mechanisms to clinical applications: A comprehensive review of photobiomodulation in cancer treatment». In: *Lasers in Medical Science* (Apr. 2025). First published online: 21 April 2025 (cit. on p. 11).
- [25] Muyue Yang, Zhen Yang, Pu Wang, and Zhihui Sun. «Current application and future directions of photobiomodulation in central nervous diseases». In: *Journal of Photochemistry and Photobiology B: Biology* (2025). In press (cit. on p. 11).
- [26] Michael R. Hamblin. «Mechanisms and applications of the anti-inflammatory effects of photobiomodulation». In: *AIMS Biophysics* 4.3 (2017), pp. 337–361. DOI: 10.3934/biophy.2017.3.337 (cit. on p. 11).
- [27] R. Zein, W. Selting, and Michael R. Hamblin. «Review of light parameters and photobiomodulation efficacy: Dive into complexity». In: *Journal of Biomedical Optics* 23.12 (2018), p. 1. DOI: 10.1117/1.JBO.23.12.120901 (cit. on p. 11).

- [28] T. I. Karu, L. V. Pyatibrat, and N. I. Afanasyeva. «Cellular effects of low power laser therapy can be mediated by nitric oxide». In: *Lasers in Surgery and Medicine* 36.4 (2005), pp. 307–314. DOI: 10.1002/lsm.20148 (cit. on p. 12).
- [29] T. I. Karu. «Cellular and molecular mechanisms of photobiomodulation (low-power laser therapy)». In: *IEEE Journal on Selected Topics in Quantum Electronics* 20.2 (2014). DOI: 10.1109/JSTQE.2013.2273411 (cit. on p. 12).
- [30] Dragomir Koruga. Hyperpolarized Light. Fundamentals of Nanobiomedical Photonics. Zepter Book World, 2018 (cit. on p. 15).
- [31] M. Willemse, J. Tuszynski, and B. Fertig. Hyperlight Therapy: A Breakthrough for Healing and Enhancing Your Well-Being. Clinically proven efficacy for treating chronic wounds, rheumatoid symptoms, back pain, shoulder and neck pain, sport injuries, skin diseases, psoriasis, dermatitis, acne, seasonal affective disorder, sleeping problems, skin aging. n.d. (Cit. on p. 15).
- [32] Seyed Ahmad Raeissadat, Seyed Mansoor Rayegani, Sajad Rezaei, Leyla Sedighipour, Mohammad Hasan Bahrami, Dariush Eliaspour, and Afshin Karimzadeh. «The Effect of Polarized Polychromatic Noncoherent Light (Bioptron) Therapy on Patients with Carpal Tunnel Syndrome». In: *Journal of Lasers in Medical Sciences* 5.1 (2014), pp. 35–42. DOI: 10.22037/2014.v5i1.4557 (cit. on p. 15).
- [33] HFA Clinic. Bioptron Hyperlight Therapy. https://www.hfaclinic.com.au/bioptron-hyperlight-therapy?.com. Accessed 26 August 2025. 2025 (cit. on pp. 15, 16).
- [34] Max Born and Emil Wolf. *Principles of Optics*. Cambridge University Press, 2019 (cit. on p. 15).
- [35] Edward J. Calabrese. «Nitric Oxide: Biphasic Dose Responses». In: *Critical Reviews in Toxicology* 31.4-5 (2001), pp. 489–501. DOI: 10.1080/2001409111 1776 (cit. on p. 15).
- [36] Ezgi Kalay. Bioptron Hyperlight Therapy Technical Overview. https://epic-photonics.com/wp-content/uploads/2022/05/Ezgi-Kalay-Biopt ron.pdf?.com. Accessed 26 August 2025. 2022 (cit. on p. 15).
- [37] Frans C. Ramaekers and Fred T. Bosman. «The cytoskeleton and disease». In: Journal of Pathology 204.4 (Nov. 2004), pp. 351–354. DOI: 10.1002/path. 1665 (cit. on p. 18).
- [38] Tim Mitchison and Marc Kirschner. «Cytoskeletal dynamics and nerve growth». In: *Neuron* 1.9 (1988) (cit. on p. 18).

- [39] Carsten Janke and Maria M. Magiera. «The tubulin code and its role in controlling microtubule properties and functions». In: *Nature Reviews Molecular Cell Biology* 21 (2020), pp. 307–326. DOI: 10.1038/s41580-020-0214-3 (cit. on pp. 19, 28).
- [40] William A. Wells. «The discovery of tubulin». In: Journal of Cell Biology 169.4 (May 2005), p. 552. DOI: 10.1083/jcb1694fta1 (cit. on p. 19).
- [41] Pavla Binarová and Jack Tuszynski. «Tubulin: Structure, Functions and Roles in Disease». In: Cells 8.10 (Oct. 2019), p. 1294. DOI: 10.3390/cells8101294 (cit. on pp. 19, 20, 29).
- [42] Gary P. Sackett. «Toward a more temporal view of organism-environment interaction». In: Conceptualization and measurement of organism-environment interaction. Ed. by Theodore D. Wachs and Robert Plomin. American Psychological Association, 1991, pp. 11–28. DOI: 10.1037/10100-001 (cit. on p. 19).
- [43] Richard F. Ludueña. «A hypothesis on the origin and evolution of tubulin». In: *International Review of Cell and Molecular Biology* 302 (2013), pp. 41–185. DOI: 10.1016/B978-0-12-407699-0.00002-9 (cit. on p. 20).
- [44] Aarat P. Kalra, Boden B. Eakins, Sahil D. Patel, Vahid Rezania, Jack A. Tuszynski, and Karthik Shankar. «All Wired Up: An exploration of the electrical properties of microtubules and tubulin». In: *ACS Nano* (2020) (cit. on pp. 20, 28, 30, 69).
- [45] Tim Mitchison and Marc Kirschner. «Dynamic instability of microtubule growth». In: *Nature* 312 (1984), pp. 237–242. DOI: 10.1038/312237a0 (cit. on pp. 21, 28).
- [46] Chia-Hao Yu, Stephanie Redemann, Hsin-Yu Wu, Robert Kiewisz, Tae Young Yoo, William Conway, Reza Farhadifar, Thomas Müller-Reichert, and Daniel Needleman. «Central-spindle microtubules are strongly coupled to chromosomes during both anaphase A and anaphase B». In: *Molecular Biology of the Cell* (2019) (cit. on p. 21).
- [47] Carsten Janke and Magdalena M. Magiera. «The tubulin code and its role in controlling microtubule properties and functions». In: *Nature Reviews Molecular Cell Biology* 21.6 (2020), pp. 307–326. DOI: 10.1038/s41580-020-0214-3 (cit. on p. 22).
- [48] Bruce Alberts, Alexander Johnson, Julian Lewis, David Morgan, Martin Raff, Keith Roberts, and Peter Walter. *Molecular Biology of the Cell.* 6th ed. Garland Science, 2014 (cit. on pp. 23, 26).

- [49] Roberto Dominguez and Kenneth C. Holmes. «Actin structure and function». In: Annual Review of Biophysics 40 (2011), pp. 169–186. DOI: 10.1146/annurev-biophys-042910-155359 (cit. on pp. 23, 25, 26, 29, 30).
- [50] Felipe Merino, Samara Pospich, and Stefan Raunser. «Towards a structural understanding of the remodeling of the actin cytoskeleton». In: Seminars in Cell and Developmental Biology 102 (2020). Epub 2019 Dec 10, pp. 51–64. DOI: 10.1016/j.semcdb.2019.11.018 (cit. on pp. 23, 29, 30).
- [51] F. B. Straub. «Studies in International Medical Chemistry». In: *Studies Int med Chem Univ Szeged*. Ed. by Szent-Györgyi. Vol. 2. Karger, 1942, pp. 3–15 (cit. on p. 24).
- [52] A. Uzman. Molecular Cell Biology (4th edition): Harvey Lodish, Arnold Berk, S. Lawrence Zipursky, Paul Matsudaira, David Baltimore and James Darnell. Biochem. Mol. Biol. Educ. 29, 126–128 (2001). New York, NY: Freeman & Co., 2000. ISBN: 0-7167-3136-3 (cit. on p. 24).
- [53] Tatyana Svitkina. «The Actin Cytoskeleton and Actin-Based Motility». In: Cold Spring Harbor Perspectives in Biology 10.1 (2018), a018267. DOI: 10.1101/cshperspect.a018267 (cit. on pp. 24, 29).
- [54] Dominique Pantaloni et al. «Actin dynamics and polymerization». In: *Nature* (2001). DOI: 10.1038/35017011 (cit. on p. 24).
- [55] Evgeny B. Stukalin et al. «Mechanics of actin networks». In: *Biophysical Journal* (2005). DOI: 10.1529/biophysj.105.074211 (cit. on pp. 25, 26).
- [56] A. Demosthene et al. «Actin-related study». In: *Biomolecules* (2023). DOI: 10.3390/biom13050786 (cit. on p. 26).
- [57] Arshad Desai and Timothy J. Mitchison. «Microtubule polymerization dynamics». In: Annual Review of Cell and Developmental Biology 13 (1997), pp. 83–117 (cit. on p. 26).
- [58] Carsten Janke and Jean-Baptiste Bulinski. «Post-translational regulation of the microtubule cytoskeleton: mechanisms and functions». In: *Nature Reviews Molecular Cell Biology* 12 (2011), pp. 773–786 (cit. on p. 27).
- [59] Alan Hall. «Rho GTPases and the actin cytoskeleton». In: Science 279.5350 (1998), pp. 509–514 (cit. on p. 27).
- [60] Laurent Blanchoin, Renaud Boujemaa-Paterski, Catherine Sykes, and Julie Plastino. «Actin dynamics, architecture, and mechanics in cell motility». In: *Physiological Reviews* 94.1 (2014), pp. 235–263 (cit. on p. 27).
- [61] Claire E. Walczak and Sarah L. Shaw. «A MAP for bundling microtubules». In: Cell 133.1 (2008), pp. 8–10 (cit. on p. 27).

- [62] Marileen Dogterom and George H. Koenderink. «Actin-microtubule crosstalk in cell biology». In: Nature Reviews Molecular Cell Biology 14 (2013), pp. 38– 48 (cit. on p. 27).
- [63] Elisabetta Di Gregorio, Michael Staelens, and Jack A. Tuszyński. «Raman Spectroscopy Reveals Photobiomodulation-Induced  $\alpha$ -Helix to  $\beta$ -Sheet Transition in Tubulins». In: *Journal of Functional Science* (2025). Advance online publication (cit. on pp. 29, 30).
- [64] F. M. Smits. «Measurement of Sheet Resistivities with the Four-Point Probe». In: Bell System Technical Journal 37.3 (1958), pp. 711–718. DOI: 10.1002/j. 1538-7305.1958.tb03883.x (cit. on p. 30).
- [65] D. Lee, S. Kim, and J. Park. «Electrical Conductivity Measurements of Protein-Based Thin Films Using a Four-Point Probe Technique». In: *Journal of Applied Physics* 125 (2019), p. 045102. DOI: 10.1063/1.5066558 (cit. on p. 30).
- [66] Aarat P. Kalra, Piyush Kar, Jordane Preto, Vahid Rezania, Aristide Dogariu, John D. Lewis, Jack A. Tuszynski, and Karthik Shankar. «Behavior of  $\alpha$ ,  $\beta$  tubulin in DMSO-containing electrolytes». In: *Nanoscale Advances* 1.9 (2019), pp. 3364–3371. DOI: 10.1039/C9NA00354D (cit. on pp. 33, 41, 42, 63).
- [67] Aarat P. Kalra et al. «Revealing and Attenuating the Electrostatic Properties of Tubulin and Its Polymers». In: *Small* 16.45 (2020), p. 2003560. DOI: 10.1002/smll.202003560 (cit. on p. 48).
- [68] Iara B. Santelices et al. «Response to Alternating Electric Fields of Tubulin Dimers and Microtubule Ensembles in Electrolytic Solutions». In: *Scientific Reports* 7 (2017), p. 9594. DOI: 10.1038/s41598-017-09323-w (cit. on p. 61).
- [69] Azin Sadat and Iris J. Joye. «Peak Fitting Applied to Fourier Transform Infrared and Raman Spectroscopic Analysis of Proteins». In: *Applied Sciences* 10.17 (2020), p. 5918. DOI: 10.3390/app10175918. URL: https://doi.org/10.3390/app10175918 (cit. on p. 65).
- [70] Dmitry Kurouski, Thomas Postiglione, Tanja Deckert-Gaudig, Volker Deckert, and Igor K. Lednev. «Amide I vibrational mode suppression in surface (SERS) and tip (TERS) enhanced Raman spectra of protein specimens». In: *Journal of the American Chemical Society* 135.1 (2013), pp. 139–146. DOI: 10.1021/ja308273t. URL: https://pmc.ncbi.nlm.nih.gov/articles/PMC3586543/(cit. on p. 65).